UCSF
UC San Francisco Electronic Theses and Dissertations

Title

Improving Brain Tumor Characterization and Management Using 1H and Hyperpolarized 13C Magnetic Resonance Spectroscopic Imaging

Permalink

https://escholarship.org/uc/item/3k5431pm

Author

PARK, IL WOO

Publication Date

2010

Peer reviewed|Thesis/dissertation

eScholarship.org Powered by the California Digital Library
University of California

Improving Brain Tumor Characterization and Management Using 1H and Hyperpolarized 13C Magnetic Resonance Spectroscopic Imaging

by

Il Woo Park

DISSERTATION

Submitted in partial satisfaction of the requirements for the degree of

DOCTOR OF PHILOSOPHY

in

Bioengineering

in the

Copyright 2010

By

Il Woo Park

Dedicated to

My parents, Choon Sung Park and Sun Ho Lee

and

My wife, Kate Kiyoon Kwon

Acknowledgements

Most of all, to my mentor, Sarah Nelson, I am incredibly fortunate to have her as my mentor. She has shown me what it means to be a good mentor, leader and role model. Without her kindness, generosity, encouragement and guidance, I would not be able to finish my graduate school. I am truly grateful for the supports and opportunities she has provided me from the first day of my study.

to Daniel Vigneron, John Kurhanewicz and Soonmee Cha, for their expert knowledge and experiences that contributed to shape my research direction,

to Sabrina Ronen, for the great discussions and for allowing me to experience the world of biochemistry,

to Sharmila Majumdar and Xiaoliang Zhang for serving on my qualifying exam committee and for many helpful inputs,

to Andrea Pirzkall, for guiding me in the early days of my study,

to Matthew Zierhut, Yi-Fen Yen, Mark Albers and Albert Chen, for teaching me how to perform hyperpolarization experiment and for their contributions,

to Simon Hu and Peder Larson, for their assists in running ^{13}C experiments,

to Ralph Hurd, Douglas Kelley, David Wilson, Kayvan Keshari, Cornelius von Morze, Duan Xu, Janine Lupo, Esin Ozturk-Isik, Mark Van Criekinge, Jason Crane, Nan Tien, Yan Li and Hagit Dafni, for their great opinions and various inputs,

to Bob Bok and Kristen Scott, for training me for the animal handling and preparation,

to Hikari Yoshihara, Galen Reed, Peter Shin, Trey Jalbert, Myriam Chaumeil, Chris Ward, Humsa Venkatecsh and Vickie Zhang, for assisting with experiments,

to C. David James, Tomoko Ozawa, Raquel Santos, Scott Vandenberg and Joanna Phillips, for their collaboration,

to Niles Bruce, Bert Zimenez and Mary Mcpolin, for their helps in acquiring patient data and scanner scheduling,

to my current and past colleagues in Nelson lab: Kate Hammond, Inas Khayal, Joe Osorio, Radhika Srinivasan, Rebecca Choy, Forest Crawford, Bo Han, Paul DiCamillo, Michael Lee, Collen McGue, Pieter Pels, Eugene Ozhinksy, Emma Essock-Burns, Angela Jakary, Laleh Jalilian, Beck Olson, Wei Bian, Rupa Parvataneni, Achuta Kadambi, Adam Elkhaled, Chris Williams, Alexandra Constantin, Gabriela Bourne and Maryam Vareth, for

helping me in various ways and making our lab a friendly and pleasant environment,

to brothers and sisters in IGSM, for their cares and prayers,

to my parents-in-law, Oh Chul Kwon and Mi Ja Oh, for their tremendous supports, cares and love for me,

to my parents, Choon Sung Park and Sun Ho Lee, for their sacrificial love and supports in my entire life and for raising me to be a person with a warm heart,

and, finally, to my wife, Kiyoon, for her love and endless support, for her sacrifice, without which the completion of my Ph.D. wouldn't be possible, for being a source of encouragement, for her smile that makes me truly happy and for being a life-long companion,

This dissertation project was funded by UC Dean's Health Science grants, an academic-industry research grants ITL-BIO04-10148 and ITL-BIO-08-104, which is funded by the UC Discovery Program in conjunction with GE Healthcare, and by NIH grants SPORE P50CA97297, R01CA059880, R01CA127612 and R01 EB007588.

Il Woo Park

September 30, 2010

Abstract

Improving Brain Tumor Characterization and Management Using ^{1}H and Hyperpolarized ^{13}C Magnetic Resonance Spectroscopic Imaging

by

Il Woo Park

Magnetic resonance spectroscopic imaging (MRSI) has been used for the evaluation of properties of a number of different metabolites within tissue in the body. In the case of brain tumors, ^{1}H MRSI has been widely used due to its ability to measure metabolic profiles that are visibly altered in cancerous tissue. Recent developments in the technology required to implement dynamic nuclear polarization have enabled the acquisition of ^{13}C MRSI data for probing cancer metabolism. The goal of this dissertation was to develop new methods for the characterization and management of brain tumors using ^{1}H and hyperpolarized ^{13}C MRSI.

Four distinct projects are included in this dissertation. The first examines the feasibility of using combined information from ^{1}H MRI and MRSI for radiation target definition in a retrospective study using data from patients with gliomas. The second implemented a new lactate-edited 3D ^{1}H MRSI sequence on a 3 Tesla (T) MRI scanner in an attempt to assess lactate in patients with gliomas. The third focus evaluated the feasibility of using ^{13}C MRSI with hyperpolarized [1-^{13}C]-pyruvate as a substrate for the evaluation of *in vivo* tumor metabolism in a rat brain tumor model from a human

glioblastoma xenograft. Finally, these ^{13}C metabolic imaging techniques were used for the detection of early response to therapy in a rat brain tumor model.

These projects show that the combination of MRI and ^{1}H MRSI or hyperpolarized ^{13}C MRSI is likely to be extremely important for targeting focal therapy and evaluating treatment effects. The specialized lactate-edited 3D ^{1}H MRSI sequences that were used detected lactate in patients with brain tumors at both 1.5 T and 3 T, which means that brain lactate can be evaluated in a routine clinical setting to study its potential as a marker for prognosis and response to therapy. The data from hyperpolarized ^{13}C MRSI studies indicate that metabolic imaging with hyperpolarized [1-^{13}C]-pyruvate provides a new tool that would be valuable for clinical neuro-oncologists to use in monitoring tumor response to therapy.

Table of Contents

Chapter 1: Introduction 1

Chapter 2: Background – Brain Tumors 4
2.1 Classification of Brain Tumors 4
2.1.1 Primary and Metastatic Brain Tumors 4
2.1.2 Classification of Gliomas 5
2.1.3 Grading of Astrocytomas 6
2.2 Treatment of Brain Tumors 7
2.2.1 Surgery 8
2.2.2 Radiation Therapy 8
2.2.3 Chemotherapy 9

Chapter 3: Background – Fundamentals of MR 11
3.1 Basics of Magnetic Resonance Imaging 11
3.1.1 Spin Physics 11
3.1.2 Relaxation 14
3.1.3 Localization 17
3.2 Basics of Magnetic Resonance Spectroscopy 20
3.2.1 Chemical Shift 21
3.2.2 Acquisition of MRS data 22
3.3 Basics of Hyperpolarized ^{13}C MRS 24
3.3.1 Hyperpolarization 25
3.3.2 ^{13}C Hyperpolarizaion by Dynamic Nuclear Polarization 26
3.3.3 Imaging of Hyperpolarized ^{13}C Agents 29
3.3.4 Probing Cancer Metabolism using Hyperpolarized [1-^{13}C]-pyruvate 30

Chapter 4: Patterns of Recurrence Analysis in Newly Diagnosed GBM Following 3D Conformal Radiation Therapy with respect to Pre-RT MR Spectroscopic Findings 32

4.1 Introduction 32
4.2 Materials and Methods 34
4.2.1 Patients Population 35
4.2.2 MRI/MRSI Acquisition 36
4.2.3 ROIs and MRI/MRSI Volumetric Evaluation 37
4.3 Results 39
4.3.1 Pre-RT 39
4.3.2 Post-RT Follow-up with respect to the RT Dose 42
4.3.3 Post-RT Follow-up with respect to MRI/S 45
4.3.4 Relationship between Volumes Receiving 60 Gy and MRI/S Lesions 47
4.4 Discussion 48

Chapter 5: Implementation of 3T Lactate-Edited 3D ^{1}H MR Spectroscopic Imaging with Flyback Echo-Planar Readout for Patients with Gliomas 53
5.1 Introduction 53
5.2 Materials and Methods 58
5.2.1 Sequence Development and Implementation 58
5.2.2 Estimation of Chemical Shift Artifacts with Over-PRESS Factors 59
5.2.3 Spectroscopic Imaging 60
5.2.4 Chemical Shift Artifacts with Different Over-PRESS Factors in Phantom 60
5.2.5 Comparison between the Conventional Phase Encoding and Flyback Readout Gradient Methods 61
5.2.6 Patient Data Acquisition 63
5.2.7 Data Processing and Quantification 64
5.3 Results 65
5.3.1 Estimation of Chemical Shift Artifacts with Over-PRESS Factors 65
5.3.2 The Effect of Chemical Shift Artifacts on Metabolite Signal in Phantom 68
5.3.3 Comparison between the Conventional Phase Encoding and Flyback Readout Gradient Methods 72
5.3.4 Patient Data from the Lactate-Edited 3D MRSI with a Flyback Gradient 73
5.4 Discussion 76

Chapter 6: Hyperpolarized ^{13}C MR Metabolic Imaging: Application to Brain Tumors 80
6.1 Introduction 80
6.2 Materials and Methods 83
6.2.1 Cell Culture and Implantation of Intracerebral Tumors 83
6.2.2 Animal Preparation 83
6.2.3 Polarization Procedure 85
6.2.4 ^{1}H and ^{13}C MR Imaging 86
6.2.5 Immunohistochemical Analysis 87
6.2.6 Data Processing 88
6.2.7 Data Analysis 88
6.3 Results 90
6.4 Discussion 100

Chapter 7: Detection of Early Response to Temozolomide Treatment in Brain Tumors Using Hyperpolarized ^{13}C MR Metabolic Imaging 107
7.1 Introduction 107
7.2 Material and Methods 108
7.2.1 Cell Culture 108
7.2.2 Intracerebral Tumor Implantation 109
7.2.3 Animal Population and Imaging Study Scheme 109
7.2.4 Polarization Procedure 110
7.2.5 ^{1}H and ^{13}C MR Imaging 111
7.2.6 Data Analysis 113
7.3 Results 114
7.4 Discussion 119

Chapter 8: Summary 122

References 124

List of Tables

Table 3.1 Net spin, gyromagnetic ratio and natural abundance for isotopes commonly used for NMR and MRI experiment 13

Table 3.2 T_1 and T_2 values for specific tissues at 3T 17

Table 4.1 Summary of the pre-radiation therapy (RT) metabolic (CIN2) and combined-modality (MRI/S) findings with respect to the RT dose of 60 Gy actually delivered 40

Table 4.2 Volume comparison between MRI/S, normal brain tissue receiving 60 Gy, and the total volume of 60 Gy 42

Table 4.3 Overall contrast enhancing changes during follow-up relative to before radiation therapy 42

Table 4.4 Patients with new or increased contrast enhancement (CE) during follow-up, and the median volume of new or increased CE which extends beyond the volume of MRI/S 45

Table 5.1 Comparison of BASING, VSS and PRESS pulse parameters between the 1.5T and the newly implemented 3T sequence 59

Table 5.2 Comparison between three over-PRESS factors 68

Table 5.3 The median SNR values and metabolite ratios of brain metabolites for raw flyback, normalized flyback and conventional MRSI methods 72

Table 6.1 Summary of the rats evaluated in this study 84

Table 6.2 Immunohistochemical evaluation of the rats with intracranial human xenograft tumors 99

Table 6.3 Comparison of biological, immunohistochemical and MR features between U-251 MG and U-87 MG model 103

Table 7.1 Summary of rats included in this study 111

List of Figures

Figure 2.1 Cellular composition of subventricular zone in adult human brain 5

Figure 3.1 Precession 14

Figure 3.2 T_1 and T_2 relaxation curve 16

Figure 3.3 2DFT sequence and k-space representation 19

Figure 3.4 An example of spectrum with major brain metabolites 22

Figure 3.5 A 2D MRSI sequence based on PRESS 24

Figure 3.6 Nuclear spins at thermal equilibrium and in the hyperpolarized state 26

Figure 3.7 Thermal equilibrium polarization at 3.35 T 27

Figure 3.8 Prototype polarizer and DNP process 28

Figure 3.9 [1-^{13}C]-pyruvate metabolism and the corresponding ^{13}C spectrum 31

Figure 4.1 T1 spoiled gradient echo post-contrast at pre-radiation therapy and at 2 months post RT 38

Figure 4.2 An example of detailed dose distribution 41

Figure 4.3 Contrast enhancement (CE) volume change in follow-up scans for patients with (a) new or increased CE, and (b) decreased CE 43

Figure 4.4 Example of increasing contrast enhancement within a combined anatomic and metabolic region of interest (MRI/S) that was covered by 60 Gy 43

Figure 4.5 Example of increasing contrast enhancement within a combined anatomic and metabolic region of interest (MRI/S) that was not entirely covered by 60 Gy 44

Figure 4.6 The only patient in whom increased contrast enhancement occurred beyond the pre-radiation therapy combined MRI/MRSI 46

Figure 4.7 Examples comparing the volume of a combined anatomic and metabolic region of interest (MRI/S) and the actually delivered 60 Gy 48

Figure 5.1 The new BASING pulse waveform designed for 3T, its inversion profile and the resulting lactate editing scheme 55

Figure 5.2 The representation of voxels included for SNR calculation 61

Figure 5.3 The illustration of chemical shift mis-registration artifact for 1.2 and 1.5 over-PRESS factors 66

Figure 5.4 The effect of chemical shift artifacts on brain metabolite signal evaluated using a phantom 67

Figure 5.5 The distribution of lactate methyl doublet from MRSI data using a phantom 69

Figure 5.6 Lactate spectra from the first and second cycles acquired from a phantom using the over-PRESS factor of 1.5 70

Figure 5.7 Lactate edited spectra with flyback gradient in a phantom and a volunteer 71

Figure 5.8 Comparison of MRSI data between the flyback-gradient method and the conventional elliptical MRSI method from a volunteer 73

Figure 5.9 An example of lactate-edited spectra using the flyback-gradient method from a patient 74

Figure 5.10 An example of lactate-edited spectra using the flyback-gradient method from a patient, showing the full coverage of a slice from the PRESS volume 75

Figure 6.1 A representative example of hyperpolarized ^{13}C dynamic data from a rat with tumor 90

Figure 6.2 Representative hyperpolarized ^{13}C 2D MRSI data from a normal rat 92

Figure 6.3 Representative anatomical images and the corresponding magnitude spectra from a hyperpolarized ^{13}C 2D MRSI study of a rat with tumor 94

Figure 6.4 Comparison of ^{13}C parameters between the tumor and normal rats 95

Figure 6.5 Metabolic maps of ^{13}C imaging parameters between a rat with tumor and a control rat 96

Figure 6.6 Comparison of the SNR of lactate, pyruvate and total carbon between U-251 MG and U-87 MG xenograft 97

Figure 6.7 Staining of U-251 MG and U-87 MG xenograft with MIB-1, CA-9 and H&E 98

Figure 6.8 Correlation between proliferation marker and the SNR of lactate 99

Figure 6.9 The patterns of contrast enhancement in T1 post-Gd images between rats with U-251 MG and U-87 MG model 101

Figure 7.1 Percent change in Lac/Pyr from baseline 115

Figure 7.2 Percent tumor volume change from baseline 116

Figure 7.3 Early morphological and metabolic changes in a treated rat 117

Figure 7.4 Early morphological and metabolic changes in a control rat 118

Figure 7.5 Immunohisochemical staining of caspase-3 119

Chapter 1: Introduction

Since the first discovery of the nuclear magnetic resonance (NMR) phenomenon (1) and its application to imaging (2), magnetic resonance imaging (MRI) has evolved into one of the most significant non-invasive medical imaging tools for clinical applications and biomedical research. The ability to visualize differences in contrast between soft tissues in the body makes MRI valuable for studying neurological, musculoskeletal and cardiovascular diseases. While MRI provides structural information for the body, magnetic resonance spectroscopic imaging (MRSI) allows for the non-invasive assessment of the chemical composition of different tissues. MRSI is one of the most active areas of research in biomedical imaging and has become a popular tool for clinicians due to its ability to provide metabolic information that can be helpful in diagnosis and treatment of many diseases.

Gliomas are the most common primary brain tumor in adults and have been studied extensively with MRI and MRSI. The infiltrative nature and heterogeneity of gliomas make them difficult to characterize using purely morphological data. MRSI has been proposed as a modality that can provide extra information that would be valuable for the characterization and management of brain tumors. Initial studies using ^{1}H MRSI have shown that metabolite levels may contribute to vital information in differentiating lesions, planning therapy and evaluating therapy outcome (3-5).

MRSI of nuclei other than ^{1}H has been investigated mostly in research settings, but have not yet been used routinely in the clinic. ^{13}C is one of the nuclei that has been

proposed for MRSI experiments. Despite its potential for probing a wide range of biochemical metabolism, the application of ^{13}C MRSI has been limited by its low sensitivity. The recent application of dynamic nuclear polarization (DNP) and the development of a dissolution process that retains the polarization of ^{13}C compounds has allowed the acquisition of ^{13}C MRSI data with more than 10,000-fold signal increase compared to traditional ^{13}C MRSI (6). This technological breakthrough has made possible the real-time *in vivo* imaging of ^{13}C-labeled molecules and is expected to provide the opportunities for scientists to develop new biomarkers for the characterization and management of various diseases.

The goal of this dissertation project was to improve brain tumor characterization and management using ^{1}H and hyperpolarized ^{13}C MRSI. The first two projects provide methods to improve upon existing techniques using ^{1}H MRSI of patients with gliomas. The next two projects employ ^{13}C MRSI with hyperpolarization technology in an attempt to develop new biomarkers for brain tumors using an animal brain tumor model. This dissertation is organized in the following manner:

Chapter 2 provides a brief overview of brain tumors. The classification, grading and treatment of brain tumors were discussed.

Chapter 3 introduces the basic physics of MRI and magnetic resonance spectroscopy (MRS). The overview of hyperpolarization techniques and their application to *in vivo* ^{13}C MRSI were also provided.

Chapter 4 evaluates whether the combined ^{1}H MRI and MRSI prior to radiation therapy (RT) is valuable for target definition and assesses the feasibility of replacing the current

definition of uniform margins by custom shaped margins based on the information from ^{1}H MRI and MRSI.

Chapter 5 presents the implementation of a new lactate-edited 3D ^{1}H MRSI sequence at 3 Tesla (T) and demonstrates the feasibility of using this sequence for measuring lactate in patients with gliomas.

Chapter 6 compares *in vivo* metabolism between malignant gliomas and normal brain using ^{13}C MRSI data acquired from normal rats and rats with human glioblastoma xenografts, following injection of hyperpolarized [1-^{13}C]-pyruvate. The ^{13}C imaging parameters were characterized and compared with results from immunohistochemical analysis.

Chapter 7 demonstrates the feasibility of using hyperpolarized [1-^{13}C]-pyruvate to detect early response to therapy using an orthotopic human glioblastoma xenograft model.

Chapter 8 summarizes the results from this dissertation project and discusses their clinical implications.

Chapter 2: Background – Brain Tumors

Brain tumors comprise a mass of abnormally growing cells and are the second leading cause of cancer-related deaths in children under age 20, males up to age 29 and females under age 20 (7). The annual incidence rate of all primary brain and other central nervous system (CNS) tumors in the United States is approximately 19 cases per 100,000 person (8). This chapter will focus on basic information about brain tumors, including the classification, grading and treatment.

2.1 Classification of Brain Tumors

2.1.1 Primary and Metastatic Brain Tumors

Brain tumors are classified into categories depending on their origin: primary and metastatic. Primary brain tumors come from cells in the intracranial sphere or the central spinal canal, and tend to stay in the brain. Metastatic brain tumors originate in other organs and are delivered to the brain through the lymphatic system and blood vessels. Primary brain tumors can be further divided into benign and malignant lesions. Benign brain tumors consist of very slowly growing cells with a relatively normal appearance under a microscope but they can be life-threatening due to mass effect, depending on their location. Malignant brain tumors consist of rapidly growing cells and are very invasive and life-threatening. They differ from other cancers in that they rarely metastasize and are furthered classified by their cellular origin.

2.1.2 Classification of Gliomas

The human brain consists of two major cell types: neurons and glial cells. Neurons are the basic building blocks of the nerve system, whose main function is to possess and transmit information by electrical signals. Glial cells, also known as glia, sustain homeostasis, build myelin and provide protection and support for neurons. The human brain contains roughly equal numbers of neurons and glial cells, but their ratio differs between the different parts of the brain (9). Brain tumors that arise from glial cells are called gliomas. Gliomas make up 70% of all primary brain tumors and account for more than half of all human CNS malignancies (10). Gliomas are sub-grouped according to the origin of their cell type: astrocytomas, ependymomoas and oligodendrogliomas.

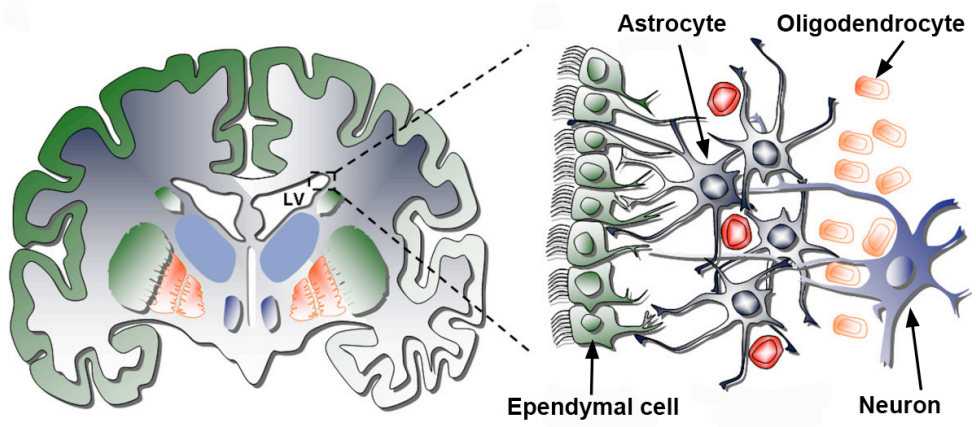

Figure 2.1 A schematic diagram describing the cellular composition of subventricular zone in adult human brain. LV: lateral ventricle.

(Adapted from: http://en.wikipedia.org/wiki/Subventricular_zone)

Astrocytomas are gliomas derived from astrocytes. Astrocytes are star-shaped glial cells in the brain and spinal cord. Their functions include endothelial cell support,

maintenance of extracellular ion balance and provision of nutrients. Astrocytomas are the most common glioma. The following section will discuss the grading system for astrocytomas.

Ependymomas are derived from ependymal cells which support neurons that form the epithelial lining of the ventricles. They produce cerebrospinal fluid (CSF) and help circulate the CSF. Approximately 5% of adult intracranial gliomas are ependymomas.

Oligodendrogliomas are derived from oligodendrocytes and make up approximately 10 % of adult giomas. The main function of oligodendrocytes is the insulation of axons by producing myelins. Oligoastrocytomas are mixed gliomas that contain both abnormal oligodendrocytes and astrocytes.

2.1.3 Grading of Astrocytomas

Astrocytomas are the most common type of gliomas and are graded based on microscopic evidence of aggressiveness or malignant characteristics. The World Health Organization (WHO) grading system has been developed for defining four different grades. Grade 1 is the least aggressive and 4 is the most aggressive. The classification is based on the appearance of four histological characteristics: nuclear atypia, mitosis, endothelial proliferation and necrosis (11).

Grade I astrocytomas are benign and slow growing in general, and do not possess any of the aforementioned features. They are typically cured by surgical removal or made inactive by radiation. The most common example is pilocytic astrocytomas.

Grade II astrocytomas possess nuclear atypia. They are relatively slow growing and benign, but can evolve into higher grade tumors if untreated. Patients with grade II

astrocytomas have a median survival of five to ten years (12). These lesions are typically referred to as low-grade gliomas.

Grade III astrocytomas, also known as anaplastic astrocytomas (AA), demonstrate anaplastic features with increased cellularity, distinct nuclear atypia and the presence of mitotic activity. The median survival for patients with AA is two to four years (13). Grade III and grade IV astrocytomas are often referred to as high-grade lesions.

Grade IV astrocytomas are the most malignant and aggressive brain tumor, and often called glioblastoma or glioblastoma multiforme (GBM). In addition to the histological characteristics of AA, GBM usually show the presence of necrosis and abnormal vasculature. GBM are the most common primary brain tumors in adults, accounting for 12-15% of intracranial tumors and 50-60% of primary brain tumors (14). GBM are very infiltrative and usually spread quickly to other parts of the brain. For these reasons, GBM are difficult to treat, and frequently recur after initial treatment. The prognosis of GBM is worst among all gliomas, with patients having a median survival of nine to twelve months (15). This dissertation focuses on developing novel methods to improve the evaluation, characterization and monitoring therapy response of GBM using MR technology. Theses topics are covered in chapters 4, 5, 6 and 7.

2.2 Treatment of Brain Tumors

The treatment of brain tumors generally involves surgery, radiation therapy and chemotherapy. Early treatment is thought to be important for increasing the chance of a good outcome. The size, type and location of tumor as well as the general health of the patient determine the most appropriate treatment strategy.

2.2.1 Surgery

Surgery is typically the first step in treating brain tumors with as extensive a resection as possible without the risk of neurological injury. Surgery has the following aims: (1) to remove as much tumor as possible, (2) to reduce intracranial pressure, and (3) to provide biopsy tissue for the accurate diagnosis of tumor and an extensive analysis of tumor sample by H&E (hematoxylin and eosin) staining, immunohistochemistry and genetic analysis.

The region of brain that shows enhancement on MR images after the administration of contrast enhancing agent is an important target for resection in GBM and some grade III gliomas. The enhancement of brain is caused by the disruption of blood-brain barrier (BBB), and has been used to define tumor extent and facilitate the differentiation of tumor from adjacent normal tissue (16,17). The resection is termed as a gross total resection for the entire removal of contrast enhancing lesion (CEL) and a subtotal resection for the partial removal of CEL. More extensive resection is associated with a more favorable outcome for patients with both high-grade and low-grade gliomas (18-21).

In some cases, it may not be possible to perform a gross total resection because of the location of tumor and the risk of causing serious neurological damage. Tumors located near the areas that control language, movement and vision are the examples of such cases. In addition, surgery is not recommended for tumors located in the thalamus and brain stem.

2.2.2 Radiation Therapy

The goal of fractionated radiation therapy is to destroy or stop the growth of tumor cells by causing damage to DNA while having minimal effect on normal brain. Although radiation affects both normal and tumor cells, most normal cells recover from the effects of radiation more quickly and completely than tumor cells. In contrast, a large number of tumor cells are destroyed as radiation treatments continue. Radiation therapy usually begins within 2 to 4 weeks after surgery or to treat inoperable tumors and some low-grade gliomas that do not require surgery.

Three-dimensional conformal radiotherapy (3D-CRT) and intensity-modulated radiation therapy (IMRT) are two of the most advanced techniques used for the planning of radiation treatment. These techniques improve the effectiveness of external beam radiation therapy by delineating tumors and adjacent structures in three dimensions using specialized planning software and information acquired from computed tomography (CT), positron emission tomography (PET) and/or MRI (22,23). We will discuss a novel method to improve the efficiency of radiation planning using MRSI in chapter 4.

One of the limitations of radiation therapy is oxygen deficiency in tumor microenvironment. Solid tumors tend to develop hypoxia because they outgrow their blood supply. Oxygen makes cancer cells more sensitive to the effects of radiation therapy by forming DNA-damaging free radicals. Tumor cells in a hypoxic condition are more resistant to radiation damage than those in a normal oxygen condition (24).

2.2.3 Chemotherapy

The goal of chemotherapy is to prevent tumor reproduction by impairing the mitosis of tumor cells or to cause tumor cells to undergo apoptosis or a programmed cell

death. Chemotherapeutic drugs that interfere with a specific phase of the cell cycle are called cell-cycle specific drugs. The examples of cell-cycle specific drugs used to treat brain tumors include etoposide (VP-16) and steroid (25-27). Other chemotherapeutic drugs act effectively at any phase of the cell cycle; these are called cell-cycle non-specific drugs. Temozolomide (Temodar), lomustine (CCNU) and carmustine (BCNU) are the examples of cell-cycle non-specific drugs used to treat brain tumors (28-30). Chemotherapy can be given alone or adjuvantly with other treatment. The combination of radiation therapy with temozolomide has been shown to increase the survival of patients with brain tumors (15,31).

One of the limitations of chemotherapy in treating brain tumors is the existence of the BBB in the brain. The BBB is a brain's unique protective mechanism to regulate molecular exchanges between the blood and the neural tissue. The tight junctions between endothelial cells act as a key component to create the selectivity at the interface between the blood and the brain. Many drugs have trouble passing through the BBB and thus are ineffective at reaching cancer cells (32,33). Delivery of drugs can also be limited due to regions with poor perfusion in high-grade gliomas.

Chapter 3: Background – Fundamentals of MR

We will briefly cover the basic physics of magnetic resonance imaging (MRI) and magnetic resonance spectroscopy (MRS) in this chapter. A classical description of magnetic resonance (MR) is sufficient to understand the materials presented in this dissertation; therefore, a quantum mechanical description of MR will be mostly omitted. Following the fundamentals of MRI and MRS, a brief introduction of dynamic nuclear polarization (DNP) and hyperpolarized ^{13}C magnetic resonance spectroscopic imaging (MRSI) will be presented.

3.1 Basics of Magnetic Resonance Imaging

MRI is a non-invasive medical imaging technique that provides a wealth of diagnostic information. It provides images with different levels of contrast for soft tissues in the body, making it very useful for neurological, musculoskeletal and cardiovascular imaging. In this section, we will discuss the basic properties of MRI including spin physics, relaxation and localization.

3.1.1 Spin Physics

Spin is a fundamental property of elementary particles; e.g. protons, electrons and neutrons. Spin appears in multiples of ½ and can be positive (+) or negative (-). An unpaired proton, electron and neutron each possess a spin of ½. Non-zero spin is associated with a non-zero dipole moment, which is represented in the following equation:

$$\mu = \gamma S \qquad [3.1]$$

where μ is the nuclear magnetic dipole moment, γ is the gyromagnetic ratio specific for a given nucleus, and S is the spin quantum number determined by the number of protons and neutrons in a nucleus. Table 3.1 shows the value of γ for several isotopes commonly used for nuclear magnetic resonance (NMR) and MRI experiments. When placed in an external magnetic field (B_0), the spin's magnetic moment can be oriented either parallel or anti-parallel to B_0. The spins parallel to B_0 are in a lower energy state than the spins anti-parallel to B_0. The difference between the two energy states (ΔE) is given by the following equation:

$$\Delta E = \gamma \hbar B_0 \qquad [3.2]$$

where $\hbar$ is the reduced Planck's constant.

Based on the Boltzmann probability distribution (34), the number of spins in the lower energy state (N_+) outnumbers the number of spins in the higher energy state (N_-), and their ratio at a given temperature T (Kelvin) is given by the following equation:

$$\frac{N_-}{N_+} = e^{-\frac{\Delta E}{kT}} \qquad [3.3]$$

where k is Boltzmann's constant. Polarization (P), which is the ratio of the excess spins in the lower energy state and the number of total spins, can be estimated as follows:

$$P = \frac{N_+ - N_-}{N_+ + N_-} \approx \frac{\gamma \hbar B_0}{2kT} \qquad [3.4]$$

Polarization is the basis for the signal in MRI. In other words, MR signal is proportional to the population difference between the two energy states. At body temperature and at a magnetic field strength of 3 Tesla (T), the polarization of ^1H is very small (approximately 10×10^{-6}). However, the high natural abundance of the ^1H isotope and the large number

of protons from water molecules in the human body produce detectable MR signals. Table 3.1 shows the natural abundance of several isotopes.

Table 3.1 Net spin, gyromagnetic ratio and natural abundance for isotopes commonly used for NMR and MRI experiments.

Isotope	Net spin	Gyromagnetic ratio (MHz/T)	Natural abundance (%)
^{1}H	1/2	42.58	99.985
^{2}H	1	6.54	0.015
^{13}C	1/2	10.71	1.11
^{14}N	1	3.08	99.63
^{15}N	1/2	-4.32	0.37
^{17}O	5/2	-5.77	0.037
^{19}F	1/2	40.08	100
^{31}P	1/2	17.24	100

A collection of spins experiencing the same external magnetic field $\mathbf{B_0}$ can be represented by a net magnetic moment vector **M**. The net magnetic moment vector is the vector sum of the magnetic moment vectors from all individual spins. **M** and $\mathbf{B_0}$ point in the same direction (+z) at thermal equilibrium (Figure 3.1a). If somehow **M** is made to point away from $\mathbf{B_0}$, **M** precesses around $\mathbf{B_0}$ (Figure 3.1b). The behavior of precession can be expressed as:

$$\frac{d\mathbf{M}}{dt} = \mathbf{M} \times \gamma \mathbf{B_0} \qquad [3.5]$$

The solution to this equation is for **M** to precess about $\mathbf{B_0}$ at a frequency:

$$\omega_0 = \gamma B_0 \qquad [3.6]$$

This frequency is called a Larmor frequency or a resonance frequency. Since γ is an intrinsic constant for a given nucleus, each nucleus possesses its own Larmor frequency. In typical field strengths, Larmor frequency is in the radio frequency (RF) range for most nuclei.

In MR experiments, the tipping of **M** away from $\mathbf{B_0}$ is achieved by applying an additional magnetic field $\mathbf{B_1}$, which is perpendicular to the $\mathbf{B_0}$ field and rotating at the Larmor frequency. This is called excitation. In the following section, we will discuss how the magnetization behaves after excitation.

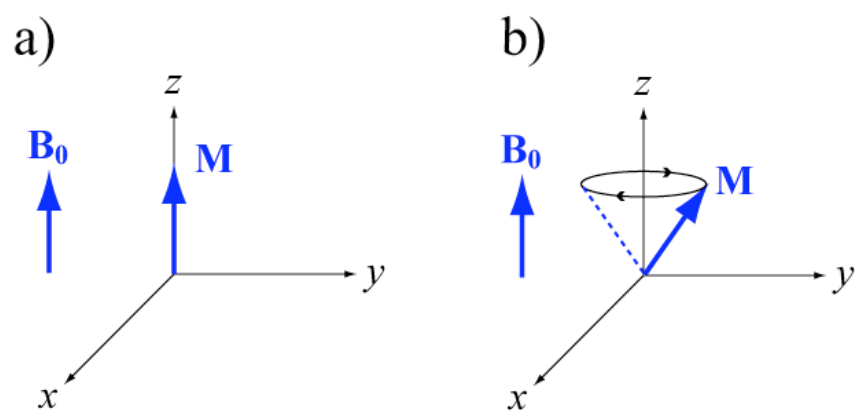

Figure 3.1 The behavior of a net magnetic moment vector **M** in the presence of an external magnetic field $\mathbf{B_0}$. **M** aligns with $\mathbf{B_0}$ at thermal equilibrium (a). **M** precesses around $\mathbf{B_0}$ when it is tipped away from $\mathbf{B_0}$ (b).

3.1.2 Relaxation

The precessing net magnetic moment vector can be expressed by the longitudinal component (M_z) and the transverse component (M_{xy}) of the magnetization. After an excitation, the M_z grows back to its equilibrium state along z according to the following equation:

$$\frac{dM_z}{dt} = -\frac{M_z - M_0}{T_1} \qquad [3.7]$$

where M_0 is the original magnetization along z. The solution to this equation is:

$$M_z = M_0 + (M_z(0) - M_0)e^{-t/T_1} \qquad [3.8]$$

T_1 is called the longitudinal relaxation time or the spin-lattice relaxation time. T_1 is the time it takes for the M_z to recover to approximately 63% (1-1/*e*) of its original longitudinal magnetization M_0 (Figure 3.2a). At a microscopic level, T_1 involves the exchange of energy between the nuclei and the surrounding lattice. The in-depth explanation of the T_1 relaxation mechanism is beyond the scope of this dissertation and if interested, the reader may examine other references (35,36).

Assuming a 90° excitation, which is the most commonly used excitation angle, the transverse component M_{xy} of the magnetization lies on the x-y plane and precesses at the resonance frequency. Ideally, the magnetization vectors from all individual spins in the volume precess at the same resonance frequency. In reality, however, the small variations of the magnetic field in the volume cause the individual magnetization vectors to rotate at slightly different frequencies. This discrepancy in the resonance frequency causes the loss of phase coherence (dephasing) and the decay of the M_{xy}. The decay of the M_{xy} after the excitation can be expressed by:

$$\frac{dM_{xy}}{dt} = -\frac{M_{xy}}{T_2} \qquad [3.9]$$

The solution to this equation is:

$$M_{xy} = M_0 e^{-t/T_2} \qquad [3.10]$$

T_2 is called the transverse relaxation time or the spin-spin relaxation time. T_2 characterizes the decay of the transverse magnetization. T_2 is the time it takes for the M_{xy} to reach 37% (1/*e*) of its initial value (Figure 3.2b). T_2 involves the energy transfer between neighboring spins. More in-depth explanation of the T_2 relaxation mechanism can be found in other references (35,36). Inhomogeneities in the main magnetic field also produce dephasing of the transverse magnetization. This additional dephasing, combined with the T_2 relaxation, represents T_2* (T_2 star) relaxation (36).

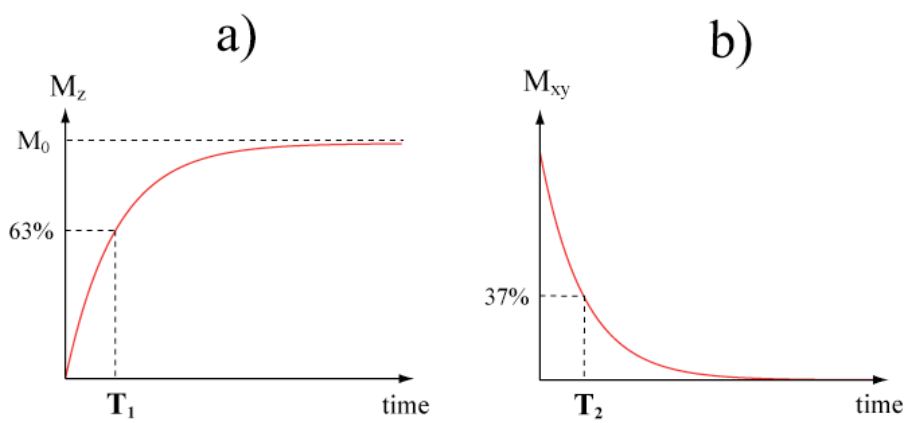

Figure 3.2 T_1 and T_2 relaxation curves. The longitudinal component of the magnetization M_z returns to its original state M_0 after an excitation (a). The transverse component of the magnetization M_{xy} decays exponentially over time (b).

The T_1 relaxation and T_2 (or T_2*) relaxation along with proton density are the major mechanisms that produce contrast in MRI. The significant variations of T_1 and T_2

(or T_2*) in different pathological tissue make MRI a very sensitive diagnostic tool. Table 3.2 shows T_1 and T_2 values in specific tissue types at 3T (37,38).

Combining Eq. [3.5] with Eq. [3.7] and [3.9] gives the Bloch equation (39):

$$\frac{d\mathbf{M}}{dt} = \mathbf{M} \times \gamma \mathbf{B_0} - \frac{(M_z - M_0)\mathbf{k}}{T_1} - \frac{M_x \mathbf{i} + M_y \mathbf{j}}{T_2} \qquad [3.11]$$

where **i**, **j** and **k** are unit vectors in x, y and z direction, respectively. The Bloch equation describes the behavior of the nuclear magnetization in terms of the longitudinal relaxation time T_1, the transverse relaxation time T_2 and the precession.

Table 3.2 T_1 and T_2 values for specific tissues at 3T.

Tissue	T_1 (ms)	T_2 (ms)
White matter	838	75
Grey matter	1607	83
Subcutaneous fat	365	133
Blood	1932	275
Kidney	1194	56
Liver	812	42

3.1.3 Localization

In MR imaging systems, the signal is detected from the receiver coil which is designed to measure changes in flux of the transverse magnetization. In other words, the received time varying signal $s_r(t)$ comes from the contribution of all transverse magnetizations in a volume:

$$s_r(t) = \int_{vol} M_{xy}(\mathbf{r},t)dV = \int_x \int_y \int_z M_{xy}(x,y,z,t)dxdydz \qquad [3.12]$$

Eq. [3.12] tells us that the signal in MRI is the magnitude of the transverse magnetization in the volume. Note that Eq. [3.12] does not provide information about the location of the signal in the volume. Additional information about localization must be acquired in order to produce useful MR images.

Magnetic field gradients are spatially varying magnetic fields and allow us to obtain spatial information in the acquisition of MR images. If we superimpose a spatially varying magnetic field on a homogeneous external magnetic field, we can create a predictable variation in the resonance frequency along a given axis. The following expression represents the resonance frequency as a function of the direction j in the presence of a magnetic field gradient:

$$w(j) = \gamma(B_0 + jG_j) = \gamma B_0 + \gamma j G_i \qquad [3.13]$$

where G_j is the magnitude of the magnetic gradient in the j direction. Applying this to all three dimensions in x, y and z, Eq. [3.12] can be expressed as:

$$s_r(t) = \int_x \int_y \int_z M_{xy}(x,y,z)e^{-i\gamma(xG_x + yG_y + zG_z)t}dxdydz \qquad [3.14]$$

This equation can be re-written as:

$$\begin{aligned} s_r(k_x,k_y,k_z) &= \int_x \int_y \int_z M_{xy}(x,y,z)e^{-i2\pi(xk_x + yk_y + zk_z)}dxdydz \\ k_j(t) &= \frac{\gamma}{2\pi}\int_0^t G_j(\tau)d\tau \end{aligned} \qquad [3.15]$$

where j can be either x, y or z. Eq. [3.15] tells us that the received signal $s_r(\mathbf{k})$ is the Fourier transform of the net magnetization density in the transverse plane M_{xy}, where the variable in the frequency domain is k_i. Thus, the data acquisition in MRI is achieved by

collecting data in the frequency domain, known as k-space. The inverse Fourier transform then converts the k-space data into an image.

There are a variety of methods for collecting k-space data to form 3 dimensional (3D) MR images. One of the most common methods is the 2 dimensional Fourier transform (2DFT) sequence. 2DFT employs a selective excitation pulse followed by the application of two magnetic field gradients for frequency encoding and phase encoding. Figure 3.3a shows a timing diagram for the 2DFT sequence. At the beginning of the sequence, slice selection is applied to selectively excite tissue in a particular region. The combination of RF pulse designed to only excite a specific range of frequency and a spatially varying magnetic field gradient G_z is used for the slice selection. In case of a 90° RF excitation, the excited spins are flipped into the transverse plane (Figure 3.3b).

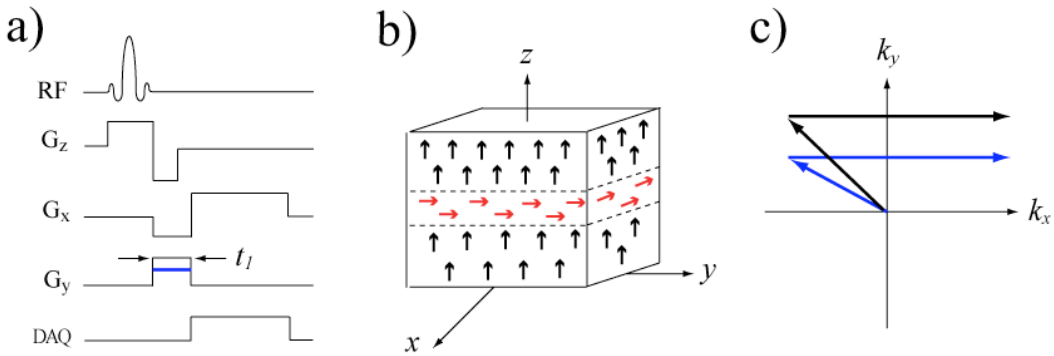

Figure 3.3 (a) Time diagram of 2DFT sequence. (b) Slice selection selectively excites spins in a specific slice from a volume. (c) K-space trajectory for two phase encoding steps. DAQ: data acquisition.

Following the slice selection, magnetic field gradients in x and y direction (G_x and G_y, respectively) are turned on. According to the equation [3.15], the k-space trajectory is

determined by the integral of these gradients. Thus, the location in the Cartesian k-space after t_1 is:

$$(k_{1,x}, k_{1,y}) = (\frac{\gamma}{2\pi} G_x t_1, \frac{\gamma}{2\pi} G_y t_1) \qquad [3.16]$$

Once the G_y turns off, the signal is read out in the presence of a constant x-gradient G_x and the entire horizontal line at $k_{1,y}$ is collected (Figure 3.3c). This step can be repeated with different G_y gradient amplitudes (blue line) until the entire k-space is covered.

Due to the specific roles of each gradient, the G_x, G_y and G_z gradient are referred to as the frequency encoding, phase encoding and slice selection gradient, respectively. Frequency encoding, phase encoding and slice selection form the basis for localization in MRI. Slice selection selects a group of spins in a plane along the z direction. When the frequency encoding gradient is applied along the x-axis of the plane while the signal is sampled, a variation in the resonance frequency is created along the x-axis. This variation is used to encode the spatial position of spins during the signal measurement. Lastly, phase encoding is used to localize the second in-plane dimension. The application of a single brief gradient in the y-axis prior to the signal readout causes the momentary variation of the precessional frequencies of the spins along the y direction. Once the phase encoding gradient is turned off, the precessional frequencies become uniform again, but the changes in phase persist. Mathematically, the spatially varying complex weighting factor $e^{-i2\pi[(\gamma/2\pi)G_y t_y]y}$ in Eq. [3.15] accounts for the phase accrual during the application of the constant phase encoding gradient. The difference among the phases of the spins at the signal readout enables the signal location along the y-axis to be mapped.

3.2 Basics of Magnetic Resonance Spectroscopy

MRS is a specialized non-invasive technique that provides information about the chemical composition of tissue in the body, whereas MRI only provides morphological information in the body. MRS has emerged as an important clinical tool for diagnosing diseases and monitoring response to therapy due to its ability to assess biochemical statuses and metabolic activity without removing tissue for biopsy. In this section, we will present the basic concepts of MRS.

3.2.1 Chemical Shift

Even in a perfectly homogeneous external magnetic field, not all protons have the same resonance frequency. The external magnetic field applied to the proton nucleus produces an orbital motion of surrounding electrons, inducing electric currents around the nucleus. These currents, in turn, generate local magnetic fields, which cause the nucleus to be shielded or deshielded from the external magnetic field. As a result, the resonance frequency from Eq. [3.6] becomes:

$$\omega_i = \gamma B_0 (1 - \sigma_i) \qquad [3.17]$$

where σ_i is the chemical shield term. This small displacement of the resonant frequency due to shielding or deshielding by the motion of surrounding electrons is termed chemical shift. Chemical shift is defined as:

$$\delta_i = \frac{\omega_i - \omega_{ref}}{\omega_{ref}} \times 10^6 \qquad [3.18]$$

where ω_{ref} is the frequency of a known reference. The most commonly used reference molecule is tetramethylsilane (TMS). Chemical shift is reported on a parts per million (ppm) scale and does not depend on field strength.

Chemical shift provides the basis for acquiring metabolite signals in MRS. Different chemical environments in a particular molecule render subtle frequency shifts

in the signal. Conventionally, MRS data are presented in a spectrum, which is a graph of signal amplitude versus frequency. Figure 3.4 is the simplified ^{1}H spectrum of major brain metabolites: total choline (Cho), total creatine (Cr) and N-acetyl aspartate (NAA). Although the ^{1}H signal of Cho, Cr and NAA all came from the protons in a methyl group (CH_3), the different molecular environments surrounding each methyl group give rise to unique chemical shift for each molecule. As a result, Cho, Cr and NAA are resolved at approximately 3.2, 3.0 and 2.0 ppm, respectively.

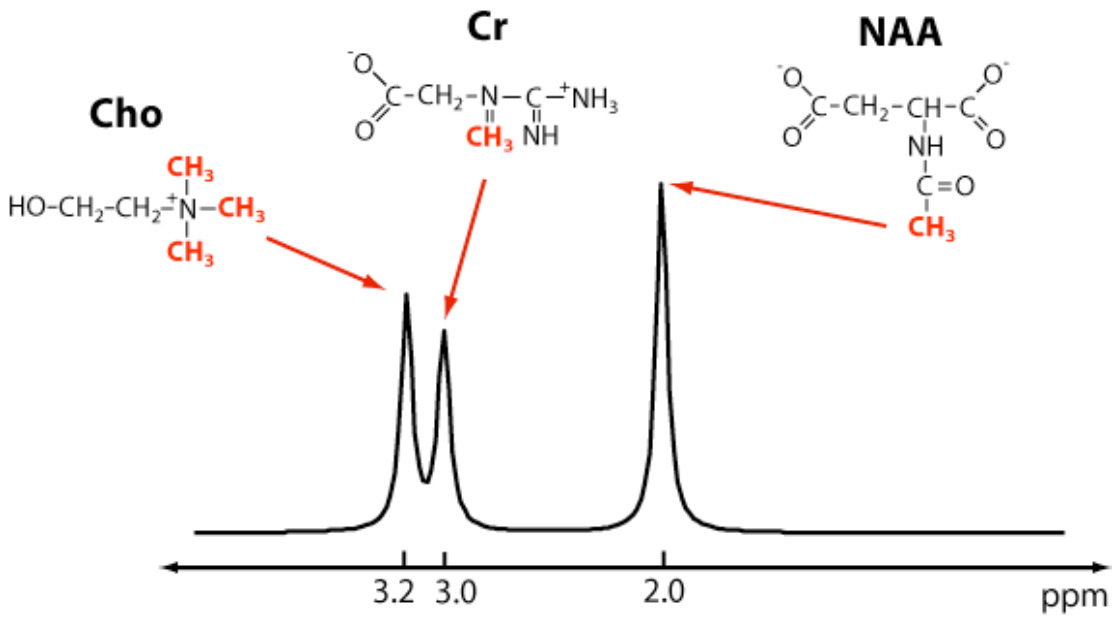

Figure 3.4 The schematic depiction of a spectrum containing major brain metabolites: total choline (Cho), total creatine (Cr) and N-acetyl aspartate (NAA).

3.2.2 Acquisition of MRS data

We can represent the MRS signal using the equation we developed in section 3.1.3. Including chemical shift, Eq. [3.15] becomes:

$$s_r(t) = \int_x \int_y \int_z \int_f M_{xy}(x,y,z,f) e^{-i2\pi(xk_x + yk_y + zk_z + f_1 k_f)} dxdydzdf$$

$$k_j(t) = \frac{\gamma}{2\pi} \int_0^t G_j(\tau) d\tau \qquad [3.19]$$

$$k_f(t) = t$$

where f_1 is the chemical shift offset frequency with respect to the Larmor frequency ω_0. Eq. [3.19] indicates that we can treat the chemical shift axis f as another spatial dimension and k_f as another k-space dimension. The acquisition of MRS data with spatial information thus requires a filling of k-space, which has an extra dimension k_f. The inverse Fourier transform then converts the k-space data into spectra with the corresponding spatial information.

There are various methods to localize MRS data (40). Point resolved spectral selection (PRESS) is one of the techniques that have been commonly used to obtain spectroscopic data with a spatial localization (41). PRESS consists of one 90° RF pulse followed by two 180° RF pulses. Slice selection gradients are applied with each RF pulse to define a 3D volume. Spatial information is encoded using phase encoding gradients, typically in two or three axes. A spectroscopy method that collects data from multiple adjacent voxels within a volume, thereby creating an image of spectra, is called chemical shift imaging (CSI) or MRSI. Figure 3.5 is the schematic diagram of a 2D MRSI sequence using PRESS localization.

Due to the high concentration of water signal and its proximity to the frequencies of the metabolites of interest, it is necessary to suppress water signal in ^{1}H MRS. Chemical shift selective (CHESS) imaging technique is one of the most commonly used techniques for water suppression (42). CHESS eliminates the water signal by employing a frequency selective 90° excitation pulse followed by spoiling gradients in all three

dimensions. The application of magnetic field gradients together with the spoiling gradients dephases the excited water signal. Depending on the organs of interest, unwanted lipid signals may pose another challenge for the acquisition of quantitative spectroscopic data. ^{1}H MRS of the human brain, for example, is vulnerable to lipid contamination due to the adjacent skull that contains the very high concentration of lipid. Outer volume saturation (OVS) is commonly used to spatially saturate the unwanted lipid signals outside the volume of interest (VOI) (43). Water suppression and outer volume saturation occur immediately prior to the employment of the conventional MRS sequence.

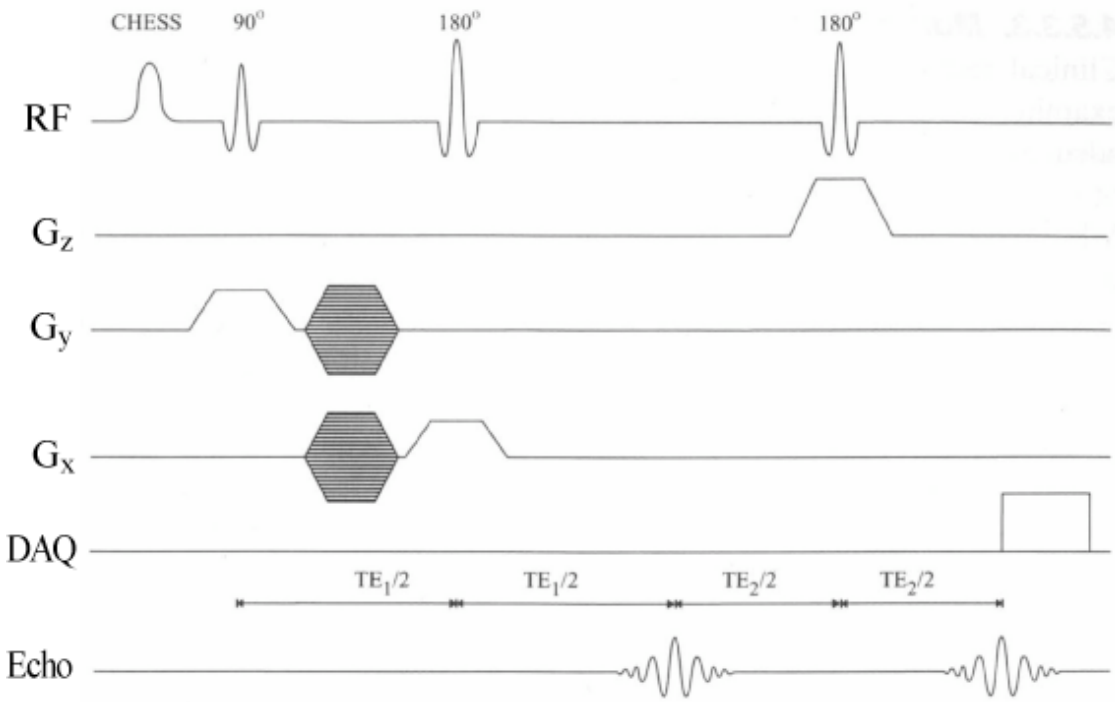

Figure 3.5 A 2D MRSI sequence based on PRESS. DAQ: data acquisition.

3.3 Basics of Hyperpolarized ^{13}C MRS

MR imaging of nuclei other than protons has been limited so far due to the lack of sensitivity at thermal equilibrium. With the recent development of hyperpolarization techniques, a significant increase in signal strength enables the imaging of non-proton nuclei for the investigation of various biochemical pathways. In this section, we will briefly introduce the concepts of hyperpolarization and discuss the application of this technique for probing cancer metabolism.

3.3.1 Hyperpolarizaion

As we discussed in section 3.1.1, MR signal depends on polarization, which is the population difference between the two spin energy states. MR imaging generally has low sensitivity due to the low polarization of nuclei at thermal equilibrium. In case of ^{1}H, there are only 10 nuclei out of a million, which contribute to the measurable MR signal. The high concentration of protons in biological tissue compensates for the low sensitivity. In contrast, MR imaging of nuclei other than ^{1}H, for example ^{13}C, ^{19}F, ^{23}Na and ^{31}P, suffers from very low sensitivity due to the low concentration of these nuclei in biological tissue. In case of ^{13}C, the low sensitivity is further weakened by its low natural abundance and small gyromagnetic ratio (Table 3.1).

A number of methods have been proposed to enhance the polarization by creating a non-equilibrium distribution of nuclear spins; in other words, a “hyperpolarized” state where the population difference between the two energy states is significantly increased (Figure 3.6). One of the methods, called brute force, is based on Eq. [3.4], which states that the thermal equilibrium polarization increases with increasing magnetic field and decreasing temperature. By cooling down the sample to the temperature close to zero Kelvin (K) at a very high magnetic field, the enhancement of polarization can be attained.

Other hyperpolarization methods include optical pumping of noble gases (44,45), parahydrogen-induced polarization (PHIP) (46,47) and DNP (48).

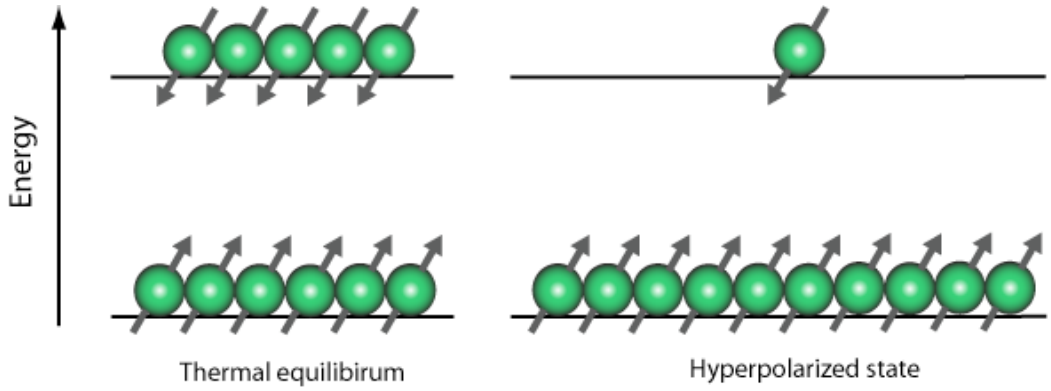

Figure 3.6 The orientation of nuclear spins at thermal equilibrium and in the hyperpolarized state.

3.3.2 ^{13}C Hyperpolarizaion by Dynamic Nuclear Polarization

The concept of DNP was first realized by Albert Overhauser in 1953, who predicted that nuclear spin population levels in metals and free radicals (unpaired electrons) would be perturbed when electron spin transitions are saturated by microwave irradiation (49). Until recently, DNP was only used for solid state polarization because polarization was quickly lost in liquid state. The recent development of a dissolution process has enabled the retainment of polarization in the liquid state on the order of approximately 25% (6).

At a temperature 1 K and ~3 T, the polarization of ^{13}C at thermal equilibrium is still very small (< 0.1%), whereas electrons are highly polarized (> 90%) due to the much larger gyromagnetic ratio of the electron (Figure 3.7). When ^{13}C-containing molecules are doped with a substance containing free radicals in an amorphous solid at ~1 K and ~ 3

T, it is possible to transfer the polarization from the radicals to the ^{13}C nuclei by irradiating with microwaves at a frequency equal to the resonance frequency of electron. This transfer process can increase the ^{13}C nuclear polarization in the solid state to 20-30 %. After the polarization transfer process has occurred, the sample is rapidly dissolved by heated and pressurized solvent (6). The dissolved sample is immediately transferred to the MRI or NMR scanner for spectroscopic experiment. It has been demonstrated that ^{13}C spectroscopy of hyperpolarized sample using this method can achieve more than 10,000 times the gain in signal-to-noise ratio compared to the conventional ^{13}C spectroscopy at thermal equilibrium (6). Figure 3.8 shows a prototype polarizer and the schematic depiction of DNP process in a ^{13}C sample.

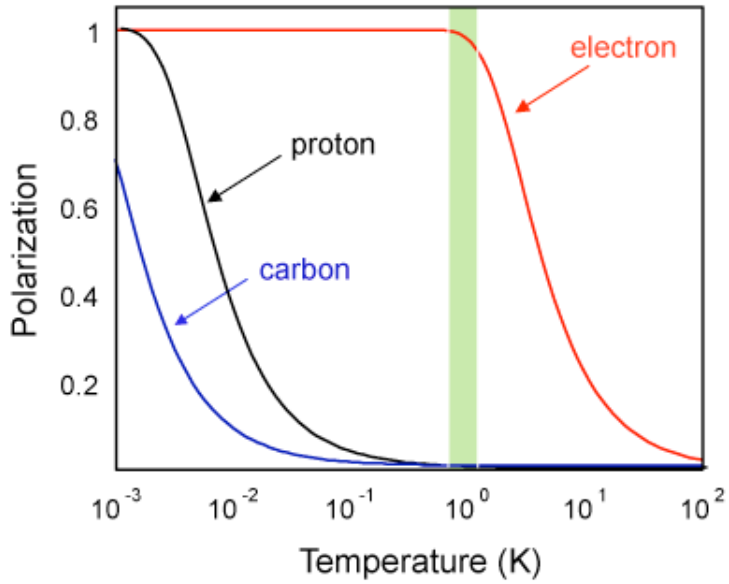

Figure 3.7 Thermal equilibrium polarization of ^{1}H, ^{13}C and electron at 3.35 T. DNP process takes place in the shaded area where the electron polarization is close to unity at the temperature near 0 K.

Although several studies have reported the DNP hyperpolarization of various nuclei (50-52), ^{13}C has mostly been used for *in vivo* MR experiments in combination with DNP hyperpolarization. There are several advantages of using ^{13}C containing molecules for hyperpolarized ^{13}C MRS. The low natural abundance of ^{13}C allows the acquisition of ^{13}C MR signal without background noise. The high gyromagnetic ratio of ^{13}C compared to other nuclei such as ^{15}N gives relatively high sensitivity. In addition, the long history of ^{13}C NMR spectroscopy makes ^{13}C-specialized instrumentations, such as RF coils tuned to ^{13}C frequency and pulse sequences for ^{13}C MRS readily available for use in hyperpolarized ^{13}C MRS.

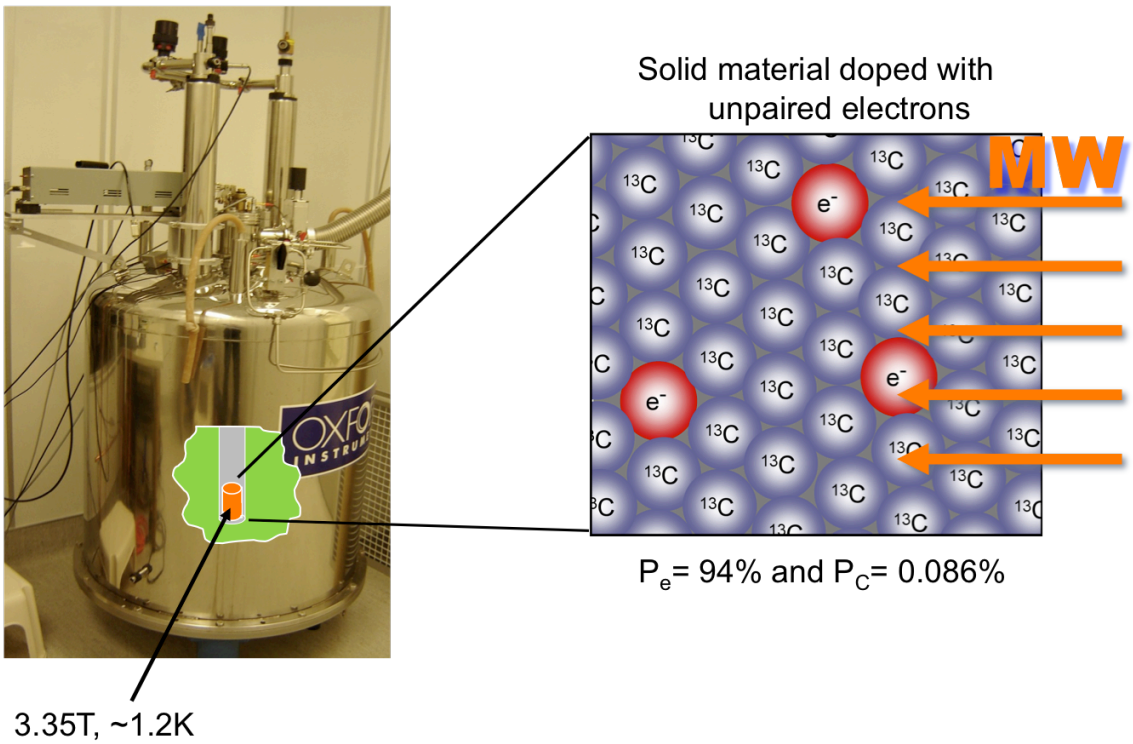

Figure 3.8 The picture of a prototype polarizer and the schematic depiction of DNP mixing process in a ^{13}C sample doped with radicals.

3.3.3 Imaging of Hyperpolarized ^{13}C Agents

The MRI of hyperpolarized ^{13}C agents is different from the ^{1}H MRI of contrast agents. In ^{1}H MRI, the administration of paramagnetic contrast agents affects the relaxation time of the protons in adjacent tissue. The change in relaxation time results in either an increase or a decrease in signal, thereby giving rise to the image contrast (53). In contrast, the hyperpolarized ^{13}C agent is the source of signal and produces the signal itself. The hyperpolarized ^{13}C agents behave similarly to the tracers used in positron emission tomography (PET) and single photon emission computed tomography (SPECT) in that they lack background signal and the signal strength is proportional to the concentration of the agent being used. The lack of background signal necessitates the acquisition of ^{1}H images for anatomical reference.

In order to use hyperpolarized ^{13}C molecules as probes for *in vivo* imaging, one must consider several characteristics of hyperpolarized ^{13}C MR. Once the dissolution process starts, the longitudinal magnetization decays back to thermal equilibrium according to the T_1 relaxation time in liquid state. As a result, the hyperpolarized ^{13}C molecule must have sufficiently long T_1 relaxation time in the liquid state. Unlike the conventional ^{1}H MRI, the longitudinal magnetization is non-renewable; therefore, the data acquisition must take place within a few minutes after the injection of hyperpolarized ^{13}C medium. Fast imaging sequences utilizing a low flip angle (54) or a single shot method (55) have typically been used to make efficient use of the longitudinal magnetization. In addition, a number of biological requirements must be met. The injected hyperpolarized ^{13}C compound has to reach the target tissue within the imaging window, which is typically a few minutes. In examining biochemical reactions, the

hyperpolarized ^{13}C compound and its resulting metabolites should reflect the relevant metabolism, and their resonances have to be sensitive enough to be resolved in ^{13}C spectra. A range of hyperpolarized ^{13}C molecules has been used for the pre-clinical study of angiography (47,55), perfusion (56,57) and metabolic imaging (58-64).

3.3.4 Probing Cancer Metabolism using Hyperpolarized [1-^{13}C]-pyruvate

[1-^{13}C]-pyruvate is currently the molecule used most extensively for DNP-hyperpolarized ^{13}C metabolic imaging. [1-^{13}C]-pyruvate meets the requirements for hyperpolarized ^{13}C MR in that pyruvate is an endogenous compound and, when labeled at the carboxyl group, possesses a relatively long T_1 of nearly one minute in aqueous solution. It is readily taken up by cells through the monocarboxylate transporter (MCT), and its metabolic pathway is well known. The main metabolites of [1-^{13}C]-pyruvate *in vivo* are lactate, alanine and bicarbonate, whose chemical shifts are well separated in their ^{13}C spectra. Figure 3.9 illustrates [1-^{13}C]-pyruvate metabolism and the corresponding ^{13}C spectrum displaying the resonances of [1-^{13}C]-pyruvate and its metabolites. Pyruvate-H_2O (pyruvate hydrate) is the pH-dependent, metabolically inactive product of a dynamic equilibrium of pyruvate in aqueous solution.

Pyruvate is a key molecule involved in glycolysis. Depending on the status of the cell, it is converted to lactate, alanine and bicarbonate to a different degree. It is well known that cancer cells preferentially depend on anaerobic glycolysis for energy production and excess lactate is produced from pyruvate by the upregulation of an enzyme called lactate dehydrogenase (LDH) (Figure 3.9a) (65). Pyruvate is, therefore, ideal for probing LDH activity and differentiating between aerobic and anaerobic

metabolism. A number of pre-clinical studies have reported the ^{13}C MRS experiments of DNP-hyperpolarized [1-^{13}C]-pyruvate for the prediction of tumor progression (62), detection of tumor response to treatment (59) and assessment of cardiac metabolism (66-68). The hyperpolarized ^{13}C MRSI of [1-^{13}C]-pyruvate for application to brain tumors will be the topic in Chapter 6 and 7.

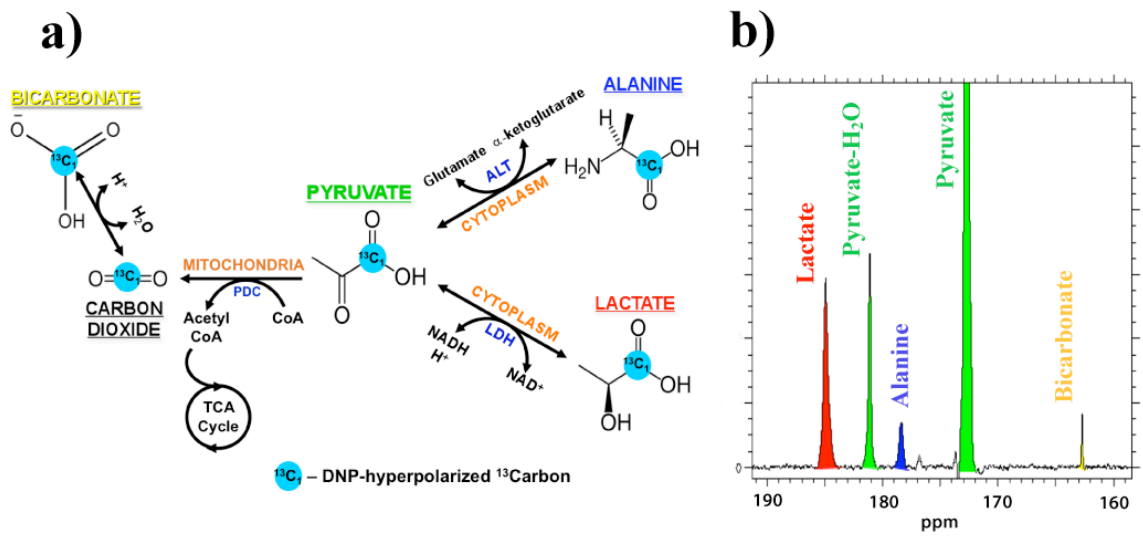

Figure 3.9 [1-^{13}C]-pyruvate metabolism (a) and the corresponding ^{13}C spectrum displaying the resonances of [1-^{13}C]-pyruvate and its metabolites: lactate, alanine and bicarbonate (b). LDH: lactate dehydrogenase; ALT: alanine transaminase; PDC: pyruvate dehydrogenase complex.

Chapter 4: Patterns of Recurrence Analysis in Newly Diagnosed GBM Following 3D Conformal Radiation Therapy with respect to Pre-RT MR Spectroscopic Findings

4.1 Introduction

High-grade malignant gliomas are the most common primary brain tumors in adults. Despite recent developments in surgical techniques and postoperative treatment, the prognosis for patients with a high-grade glioma remains very poor. The median survival has been reported in the range of 12 - 15 months for patients with glioblastoma multiforme (GBM) and 36 months for patients with anaplastic astrocytoma (AA) (15,69-71). Conventional treatment of high-grade gliomas includes surgical resection which provides immediate decompression and yields tissue for histopathologic evaluation. This is typically followed by concurrent radiation/chemotherapy.

In order to enhance the effectiveness of radiation therapy (RT) in gliomas while sparing normal tissue, it is important to accurately distinguish cancer from normal tissue. Computed tomography (CT) and magnetic resonance imaging (MRI) are currently used to delineate the target volume for high grade gliomas with MRI providing superior soft tissue contrast (72-74). Target volumes for 3D conformal radiation therapy (3D-CRT) are defined to cover the Gadolinium contrast enhancing region on T1-weighted images obtained from MRI with a uniform margin of 1 to 4 cm (69,75-77) and/or the area of hyperintense lesion on T2-weighted MRI enlarged by several centimeters (78,79).

These uniform margins are defined in an attempt to address several shortcomings with conventional anatomic imaging. Serial biopsy studies show tumor cells more than 3 cm from the contrast enhancing (CE) region (80); in addition, some tumors are not contrast-enhancing, and the T2 hyperintensity (T2h) may not distinguish tumor from edema, or normal appearing brain tissue beyond T2h might harbor tumor cells. Previous studies have shown that three-dimensional (3D) magnetic resonance spectroscopic imaging (MRSI) is valuable for mapping the spatial extent of brain tumors and this technique is suggested as an adjunct to MRI in delineating the target for radiation therapy in high-grade gliomas (HGG) (81,82).

Three-dimensional proton MR spectroscopy imaging (MRSI) provides information concerning the spatial distribution of cellular metabolites in the brain. At long echo times (TE 144ms), it provides information about levels of metabolites such as choline (Cho), creatine (Cr), N-acetyl-aspartate (NAA), and lipid/lactate (LL). NAA is a neuronal marker that is decreased in tumors. Creatine provides a measure of cellular bioenergetic processes, and may be a marker for cell oxygenation. Cho is a membrane component that is increased in tumors due to increased proliferation and/or increased membrane turnover. Lactate and lipid are presumed to represent measures of hypoxia and necrosis, respectively.

A series of image-guided biopsies have been performed at our institution in an attempt to study the biological significance of these imaging parameters. Dowling et al. correlated metabolite levels measured by preoperative MRSI with histologic findings from image-guided biopsies of brain tumors (83). The findings showed that when the pattern of MRS metabolites included abnormally increased Cho and decreased NAA

resonances, the histology of such biopsy samples invariably confirmed the presence of tumor. This prompted the development of an automated analysis that estimates peak parameters for Cho and NAA on a voxel-by-voxel basis (including normal appearing brain tissue) and computes the so-called Cho-to-NAA Index (CNI). A CNI of 2 or greater has been shown to correspond to tumor in biopsy correlation studies (84,85).

In previous studies, we have compared the differences between MRSI and MRI lesions in patients with HGG. We found significant variations between the two modalities with respect to tumor size and location prior to surgery (81), and after surgery but before RT (82). These data suggested that MRSI is likely to improve the diagnostic accuracy of the assessment of residual disease for HGG. It was concluded that the incorporation of metabolic information into the treatment planning of postoperative HGG patients would result in target volumes different in size and shape compared to the currently defined target volumes as described above.

The purpose of this study is to determine whether the combination of MRI and MRSI is of value for RT target definition. In particular, we sought to assess the feasibility of replacing the current definition of uniform margins by custom shaped margins in accordance to the tumor extent seen on MRI and MRSI in order to limit RT exposure to normal brain tissue. We therefore compared the spatial location and extent of CE at follow-up imaging with the actually delivered radiation dose and related those to spectroscopic findings prior to RT in order to assess the potential for modifying the RT target volume.

4.2 Materials and Methods

4.2.1 Patients Population

A total of thirty adult patients (22M/8F; median age 57 years, range 27-80 years) with WHO II classified glioblastoma multiforme (GBM) who were treated at the University of California, San Francisco, Medical Center between March 2000 and October 2004 were recruited for this retrospective study. Each patient underwent MRI and MRSI within 4 weeks after surgery but before RT (pre-RT). Follow-up (FU) exams with MRI/MRSI were acquired at the end of RT and at two month intervals thereafter. To be included in this study, patients must have had a pre-RT MRI and MRSI and at least one FU that included post contrast imaging. Another requirement was the availability of the radiation treatment plan. Seven patients were excluded due to incomplete follow-up data (4), an alignment failure between the pre-RT and the FU exams (1), lack of spectroscopy at pre-RT (1), or a lack of availability of the radiation treatment plan (1), leaving a total of 23 patients for evaluation.

The median age of the 23 patients studied was 53 years at the pre-RT time point with a range of 27 - 76 years. The Karnofsky performance scale (KPS) was ≥ 70. Written and informed consent for participating in the study was obtained from all patients. All 23 patients were treated with fractionated 3D-CRT and chemotherapy whereby three patients received more than one chemotherapeutic agent. Chemotherapeutic agents included Temozolomide (13), Thalidomide (3), Poly ICLC (6), Zarnestra (1), Tarceva (1), Accutane (1) and Celebrex (1), and 2 patients underwent carbogen breathing during delivery of RT following injection of bovine hemoglobin (HbOC-201). Chemotherapy was given either concurrently (15) or adjuvantly (8).

Radiation target volumes were defined based on current standard of care without

knowledge of the MRSI data. The conventional target volume was defined to encompass the region of hyperintensity on T2-weighted MR images with a uniform margin of about 1 cm and/or the region of contrast enhancement plus a margin of 2-3 cm. The addition of the 1-3 cm margin to the target volume was designed to account for microscopic tumor infiltration. The latter target volume was reduced after delivery of about 46 Gy (so called cone down) in about half of the patients and an additional 14 Gy was prescribed to the region of contrast enhancement plus a margin of about 1-2 cm. A total dose of 60 Gy was delivered in 30 fractions over a course of approximately 6 weeks by means of an average of 3 to 5 non-coplanar treatment portals designed to achieve at least 95% target coverage while meeting surrounding structure dose constraints.

4.2.2 MRI/MRSI Acquisition

Patients were scanned on a 1.5 T GE Signa MR scanner (GE Healthcare, Milwaukee, WI) using a quadrature head coil. The MRI protocol included an axial T2-weighted fluid attenuated inversion recovery (FLAIR) sequence (86,87) with 3-mm slice thickness and pre- and post-Gadolinium-DTPA T1-weighted spoiled gradient echo (SPGR) images with 1.5-mm thickness. At the end of the MRI scan, 3D MRSI was acquired using Point Resolved Spectroscopic (PRESS) (41) volume localization with spectral spatial pulses for water suppression and very selective suppression (VSS) pulses for outer volume suppression (TR/TE=1000/144 ms, 1 cc nominal spatial resolution; 12×12×8 or 16×8×8 phase-encoding matrix) (88). Spectral values were normalized relative to the noise standard deviation, estimated from the right hand end of the spectra which was devoid of metabolite peaks (89). The MRSI data were quantified offline to

estimate peak parameters for the metabolites within the excited region. A Choline-to-NAA Index of greater than 2 (CNI2) was calculated automatically and respective contours of CNI2 were displayed on the anatomic images. The details of the acquisition parameters of the MRI and MRSI examinations and the spectral processing have been published elsewhere (89,90).

MRI and MRSI data were aligned to the post contrast T1-weighted images. The treatment planning CT and the actually delivered RT dose distribution were obtained and registered to the latter in order to correlate the radiation dose distribution with the MRI and MRSI data (91-93).

4.2.3 ROIs and MRI/MRSI Volumetric Evaluation

The MRI data sets were contoured manually and verified by a radiation oncologist (AP). Regions of interest (ROI) included contrast enhancement (CE) on T1-weighted post contrast images and the hyperintensity on T2-weighted images (T2h), and the resection cavity (RC, the latter because it is included in the conventional RT target definition). Any regions of intrinsic T1 shortening, i.e. blood, were accounted for based on the pre-contrast T1-weighted images and subtracted from the CE ROI. The CNI2 contour was automatically generated by a previously described automated image analysis program (85). Because of current size and shape limitations, the PRESS volume did not always cover ROIs in their entire extent, we restricted our subsequent data analysis to the portion of these lesions that were within the PRESS volume.

The overall morphologic abnormality, which serves for the standard RT target volume definition, was defined as CE + T2h + RC (Figure 4.1a). The addition of the

metabolic abnormality (CNI2) to the morphologic abnormality defined the combined volume of MRI/S.

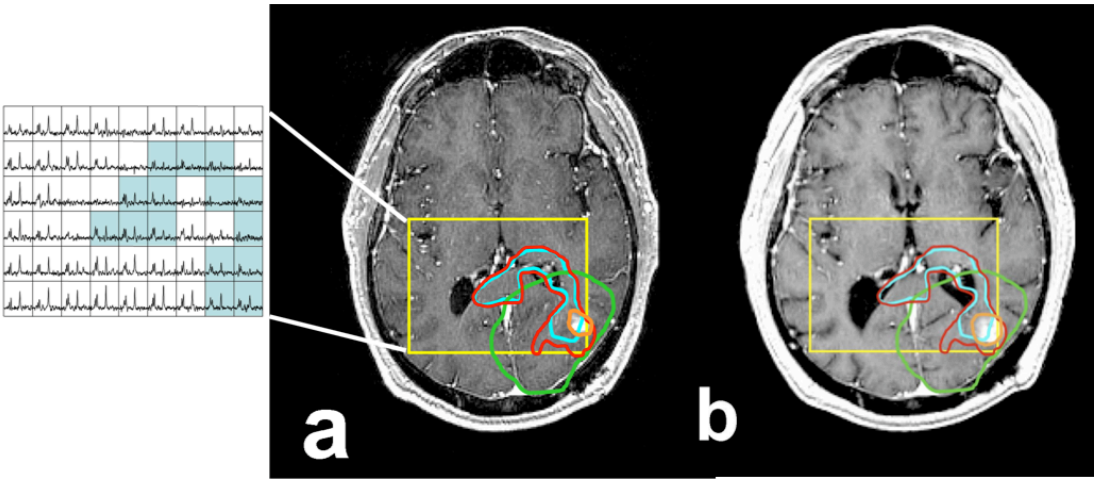

Figure 4.1 T1 spoiled gradient echo (SPGR) post-contrast at pre-radiation therapy (RT) with corresponding multi-voxel spectra (a) and at 2 months post RT (b) with superimposed regions of interest (ROIs). The ROIs include point resolved spectroscopy (PRESS; yellow rectangular box), contrast enhancement (CE; orange line), 60 Gy (green line), CNI2 (cyan line), and MRI/S (red line). Note that the CNI2 suggests tumor infiltration along the posterior aspect of the corpus callosum with crossing to the contralateral side which did not appear hyperintense on T2-weighted MRI.

The radiation treatment plans that were actually delivered to the patients were retrieved from the department of radiation oncology at UCSF and the delivered isodose lines were uploaded into our image analysis programs. The MRI/S volume and the perpendicular distance of its maximum extension beyond the 60 Gy isodose line (60 Gy) were calculated. The volume and the maximum extension of CNI2 outside the 60 Gy were also calculated in order to evaluate whether the entire region of the metabolic

abnormality as defined by CNI2 was covered by the current conventional target definition and dose distribution.

The follow-up imaging data sets were aligned to the pre-RT reference T1-weigheted post contrast SPGR data set (94). Post-RT areas of CE (as a conventional measure of possible tumor recurrence) were contoured and the pre-RT ROI's including PRESS, CNI2, 60 Gy, and the combined volume of MRI/S were superimposed and compared to the post-RT CE for analysis (Figure 4.1b). The volume and the maximum extension of CE at each follow-up scan beyond the pre-RT MRI/S were calculated. The spatial correspondence of CE during follow-up and the pre-RT CNI2 were analyzed to evaluate the degree of new/increased CE residing within or beyond CNI2 and to see whether this area of CNI2 was covered by 60 Gy. In addition, the total volumes of CE as well as the volume of CE within the PRESS volume were evaluated.

Changes in CE volume during FU were classified as "increased" (>25% increase in CE volume), "new" (onset of new CE in patients without CE residual disease at pre-RT), "stable" (less than 25% +/- volume change), or "decreased" (>25% decrease in CE volume). Upon declared clinical progression (in light of new or increased CE and neurological or neurocognitive symptoms), patients were enrolled into different treatment protocols and at that point excluded from this current analysis.

4.3 Results

4.3.1 Pre-RT

Prior to RT, 21 of 23 patients showed contrast enhancing lesions with a median CE volume of 10.1 cc, ranging from 0.4 to 42.0 cc. The median CE volume covered by

the PRESS volume was 6.3 cc, and ranged from 0.2 to 35.5 cc. The median CE volume outside the PRESS volume was 1.9 cc, and ranged from 0.05 to 11.8 cc.

There were portions of the MRI/S abnormality (CNI2+CE+T2h+RC) that were not covered by the prescribed dose of 60 Gy in 11/23 patients. Among these 11 patients, 10 showed regions of CNI2 that were not covered by 60 Gy. The median volume of CNI2 that extended beyond the prescribed dose volume was 3.5 cc (range: 0.2 – 29.2 cc), and it extended as much as 4 cm from the 60 Gy isodose contour (median 1.7, range: 0.4 – 4.0 cm). Five of the 10 patients had only minor extensions of CNI2 which were less than 2 cc. Table 4.1 summarizes the pre-RT results.

Table 4.1 Summary of the pre-radiation therapy (RT) metabolic (CIN2) and combined-modality (MRI/S) findings with respect to the RT dose of 60 Gy actually delivered.

	Number of patients	Extension volume (cc) within PRESS Median (range)	Maximum distance (cm) Median (range)
MRI/S outside 60 Gy	11/23	5.4 (1.3 – 48.5)	2.5 (1.0 – 13.6)
CNI2 outside 60 Gy	10/23	3.5 (0.2 – 29.2)	1.7 (0.4 – 4.0)

CNI2: Choline-to-NAA Index of >2; MRI: magnetic resonance imaging; PRESS: point resolved spectroscopy.

Figure 4.2 shows an example of one of the 10 patients who had CNI2 extensions suggestive of tumor infiltration along the posterior genu of the corpus callosum that was not covered by 60 Gy. The dose display for this patient shows that the majority of the CNI2 which extended beyond the 60 Gy region received ≥50 Gy, with a small portion of CNI2 receiving 40 Gy. The actually delivered doses in such CNI2 extension areas varied

across these 10 patients. Five of them received between 50 and 60 Gy to the CNI2 region outside 60 Gy, one patient received between 40 and 60 Gy, and four patients received between 30 and 60 Gy.

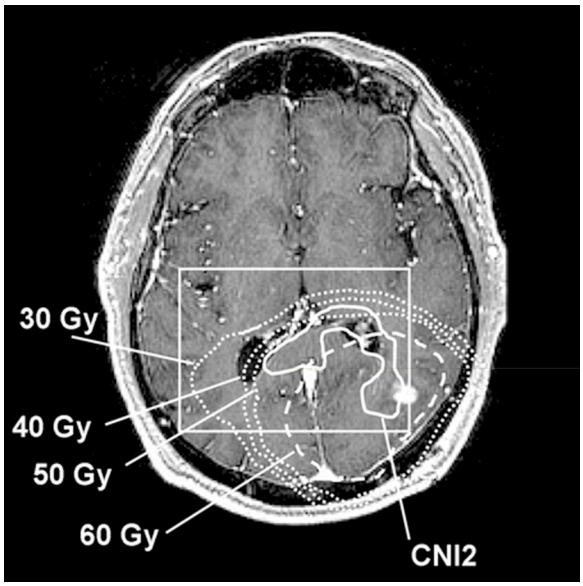

Figure 4.2 Detailed dose distribution of the same patient as in Figure 4.1 with the CNI2 region extending outside the 60 Gy isodose line (CNI2, solid line; 60 Gy, dashed line). Additional isodose lines for 30, 40, and 50 Gy are displayed as square dotted lines (outside to inside).

The volume of "normal" brain tissue within the spectroscopically evaluated region that was morphologically intact and exhibited normal metabolite levels that was exposed to the prescribed dose of 60 Gy exhibited a rather large median volume of 78.5 cc (range 20.1- 135.9 cc) compared to the volume of MRI/S (median 38.8, range 10.6 – 107.9 cc) (Table 4.2).

Table 4.2 Volume comparison between MRI/S, normal brain tissue receiving 60 Gy, and the total volume of 60 Gy for all patients and for the subset of patients with new or increased contrast enhancement.

Number of patients	MRI/S volume (cc) Median (range)	Normal brain tissue receiving 60 Gy (cc) Median (range)	Total volume of 60 Gy (cc) Median (range)
23 (total)	38.8 (10.6 - 107.9)	78.5 (20.1 – 135.9)	126.8 (71 - 165.7)
9 with new/increased CE	47.2 (15.3 - 80.2)	77.5 (44.5 – 115.5)	126.9 (81.2 - 163.9)

MRI/S: combined morphologic (MRI) and metabolic (MRSI) region of interest.

Note that the overall volume of 60 Gy was much larger than the MRI/S volume, leaving a large portion of normal brain tissue that received 60 Gy.

Table 4.3 Overall contrast enhancing (CE) changes in all 23 patients during follow-up relative to before radiation therapy (RT).

CE during follow-up	No. of patients
New/Increased CE	
CE occurring within CNI2 that was not entirely covered by 60 Gy	3
CE occurring within CNI2 that was covered by 60 Gy	6
Decreasing CE	11
Stable CE	3

4.3.2 Post-RT Follow-up with respect to the RT Dose

The changes in CE were evaluated with respect to the pre-RT parameters in all 23 patients during follow-up examinations (Table 4.3). The CE volume inside PRESS was calculated at each FU scan, and compared to that of the pre-RT scan. Median FU for all patients was 6 months with a range of 1.7 to 16.5 months. Three of the 23 patients

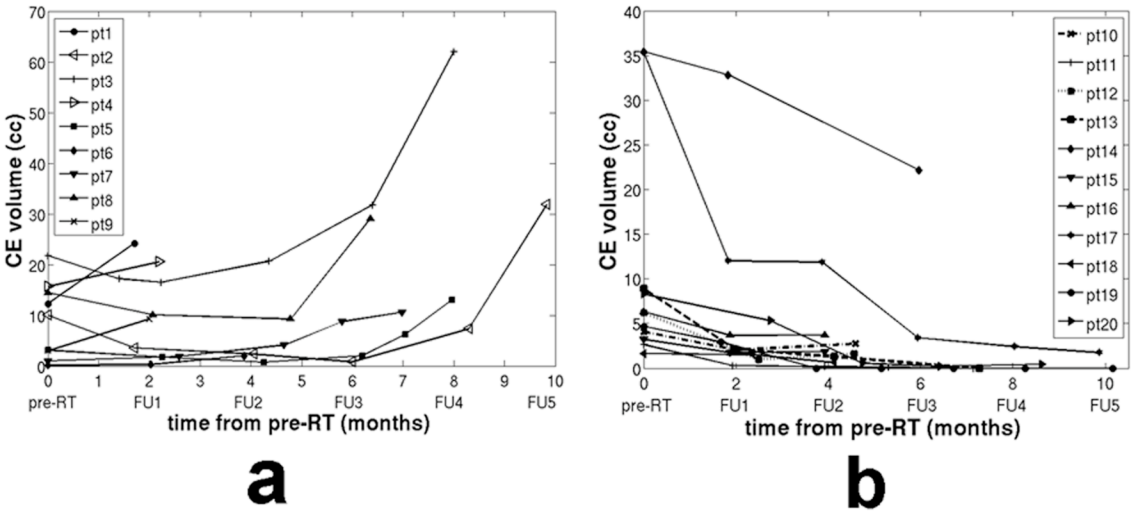

Figure 4.3 Contrast enhancement (CE) volume change in follow-up scans for patients with (a) new or increased CE, and (b) decreased CE.

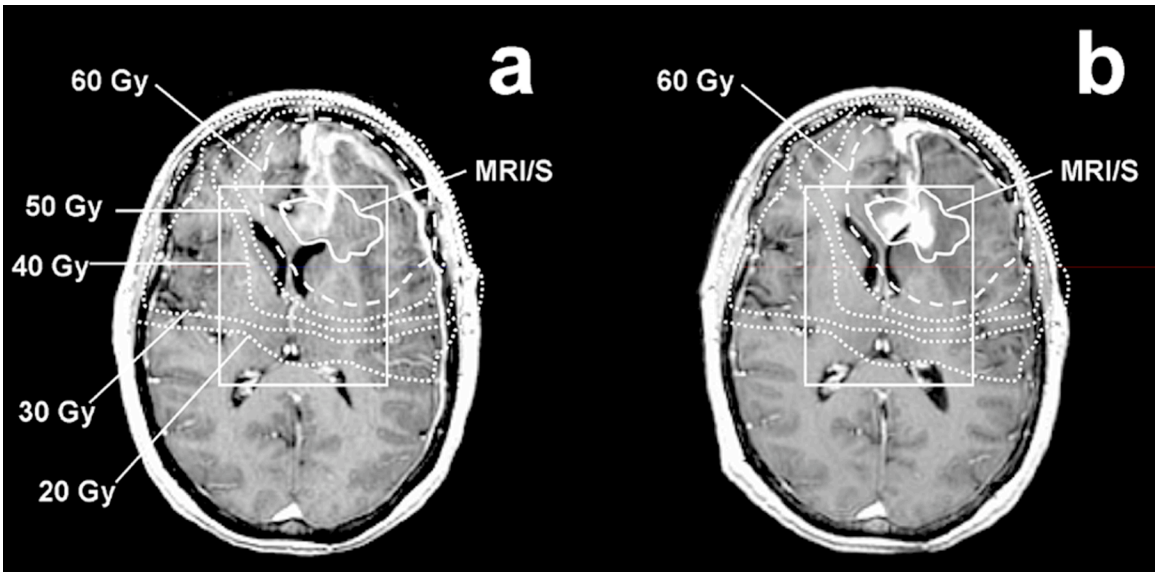

Figure 4.4 Example of increasing contrast enhancement (CE) within a combined anatomic and metabolic region of interest (MRI/S; solid line) that was covered by 60 Gy (dashed line): (a) T1 spoiled gradient echo (SPGR) pre-radiation therapy (RT), (b) T1 SPGR at 7 months post-RT.

showed stable CE, 11 showed decreasing CE (Figure 4.3b). A total of 9 patients showed new or increased CE on their FU scans that resided within the pre-RT CNI2 (Figure 4.3a). Six of them showed CE within the CNI2 that was covered by 60 Gy (see example in Figure 4.4), and 3 of them showed CE within the CNI2 that was not entirely covered by 60 Gy (see example in Figure 4.5). The first of those three patients (pt 1 in Figure 4.3a) progressed through the course of RT and developed a large contrast enhancing cyst with considerable midline shift 2 months after the start of RT. This patient deceased

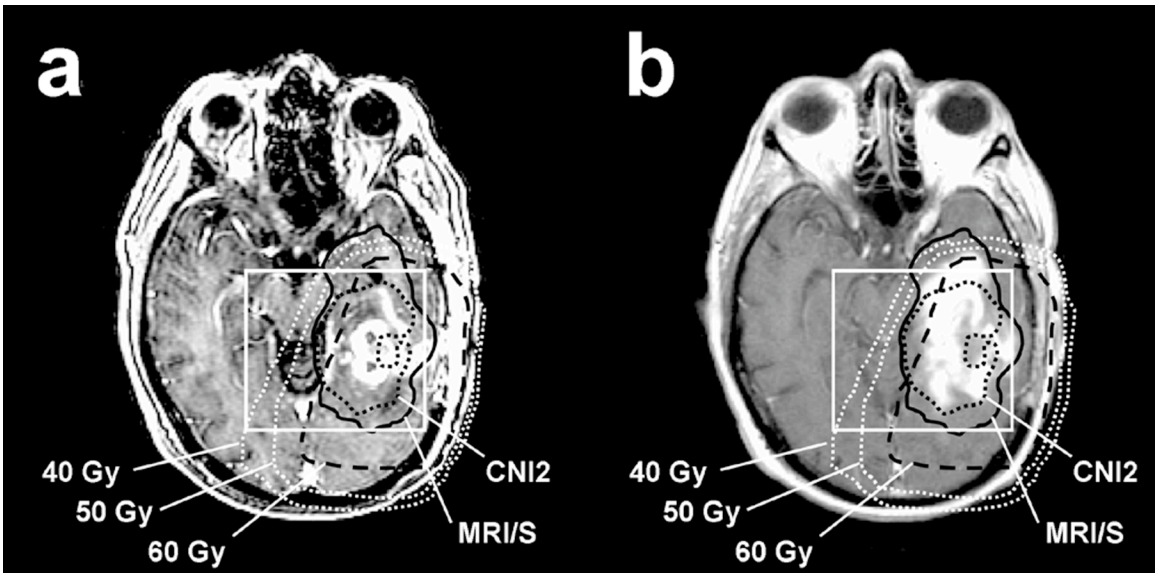

Figure 4.5 Example of increasing contrast enhancement (CE) within a combined anatomic and metabolic region of interest (MRI/S; black solid line) that was not entirely covered by 60 Gy (black dashed line): (a) T1 spoiled gradient echo (SPGR) at pre-radiation therapy (RT). (b) T1 SPGR at 8 months post-RT. Note the limited coverage of the anterior and lateral portion of the temporal lobe due to current spatial and size limitations in the point resolved spectroscopy (PRESS) prescription.

shortly thereafter. The second patient (pt 2 in Figure 4.3a) showed new CE inferior to the resection cavity, as well as enlarged CE around the resection cavity 10 months after RT. The volume of CE extending outside of the 60 Gy volume was 3 cc. This patient responded initially to RT with an overall decrease in CE volume, but showed a significant increase in CE volume at 10 months follow-up. The third patient (pt 3 in Figure 4.3a) showed increased CE volume around the resection cavity at 8 months after RT, and the volume of CE extending beyond the 60 Gy volume was 3.7 cc.

Table 4.4 Patients with new or increased contrast enhancement (CE) during follow-up, and the median volume of new or increased CE which extends beyond the volume of MRI/S.

Time after RT (months)	Number of patients with new or increased CE	Number of patients with new or increased CE beyond MRI/S	Median volume of new or increased CE beyond MRI/S (cc)
2	3	1	5.1
4	2	0	-
6	2	1	3.3
8	1	0	-
10	1	0	-

MRI/S=combined anatomic and metabolic region of interest; RT=radiation therapy.

One of the 2 patients at 6 months showed increased CE of >25% at 6 month follow-up relative to pre-RT, whereby the increased CE beyond MRI/S occurred as an outgrowth from prior discernible CE changes (<25% at prior FU).

4.3.3 Post-RT Follow-up with respect to MRI/S

We assessed whether the addition of MRS to conventional MRI target definition would have predicted regions of new or increasing CE at follow-up. For each follow-up scan, we evaluated the extent of new or increased CE and compared it at the time of progression to the size of the pre-RT MRI/S volume. Three patients showed increasing CE at the 2 month FU whereby the new or increased CE resided within the combined MRI and MRSI abnormality (MRI/S) as assessed at pre-RT in 2 of 3 patients (Table 4.4). Increased CE was found to extend beyond the pre-RT MRI/S at the 2 month FU exam in the one patient described above who developed a significant tissue shift due to the formation of a large contrast enhancing cyst (Figure 4.6). The patient deceased shortly thereafter. At 4 months post RT, new or increased CE was observed in 2 patients

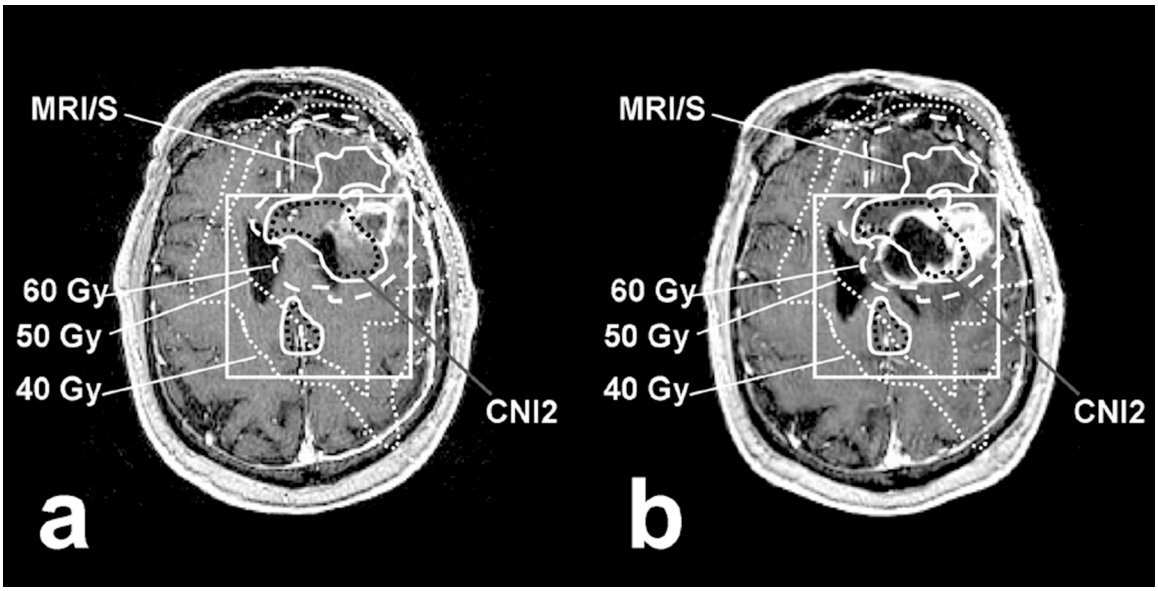

Figure 4.6 The only patient in whom increased contrast enhancement (CE) occurred beyond the pre-radiation therapy (RT) combined MRI/MRSI was caused by the formation of a large necrotic cyst that caused a significant tissue shift: (a) T1 spoiled gradient echo (SPGR) at Pre-RT. (b) T1 SPGR at 2 months post-RT.

confined to the pre-RT MRI/S. At 6 months, 2 patients showed new or increased CE. One of them showed new or increased CE residing within the MRI/S region. The other patient had showed some increase (<25%) in his CE pattern at his prior FU but increased further at 6 months and exceeded by then beyond the pre-RT MRI/S. This can be interpreted as the result of continued outgrowth from the initial recurrence pattern which was originally confined within the MRI/S lesion, as opposed to a recurrence that originated outside the combined MRI/S volume at pre-RT. One patient at 8 months and another at 10 months after RT showed new or increased CE whereby the new or increased CE was found confined within the pre-RT MRI/S volume.

4.3.4 Relationship between Volumes Receiving 60 Gy and MRI/S Lesions

For the 9 patients with new or increased CE, the median 60 Gy volume was 126.9 cc (range 81.2 – 163.9 cc), which is significantly larger than the volume of MRI/S (median 47.2 cc; range 15.3 – 80.2 cc), thereby leaving a large portion of normal brain tissue that received 60 Gy (Table 4.2). Figure 4.7 shows 2 examples in which the volume of 60 Gy is compared to the volume of MRI/S. Figure 4.7a depicts an example case where the 60 Gy isodose contour largely surrounds the volume of MRI/S leaving a considerable portion of morphologically and metabolically normal appearing brain tissue arguably over treated with 60 Gy. Defining the target volume based on the combined metabolic and morphologic information could have spared a substantial volume of brain tissue irradiated. Figure 4.7b shows another example case in which the difference between the volumes of 60 Gy and MRI/S was minimal, but the 60 Gy isodose contour

failed to cover the entire MRI/S abnormal region because the target definition was based on the MRI abnormality alone.

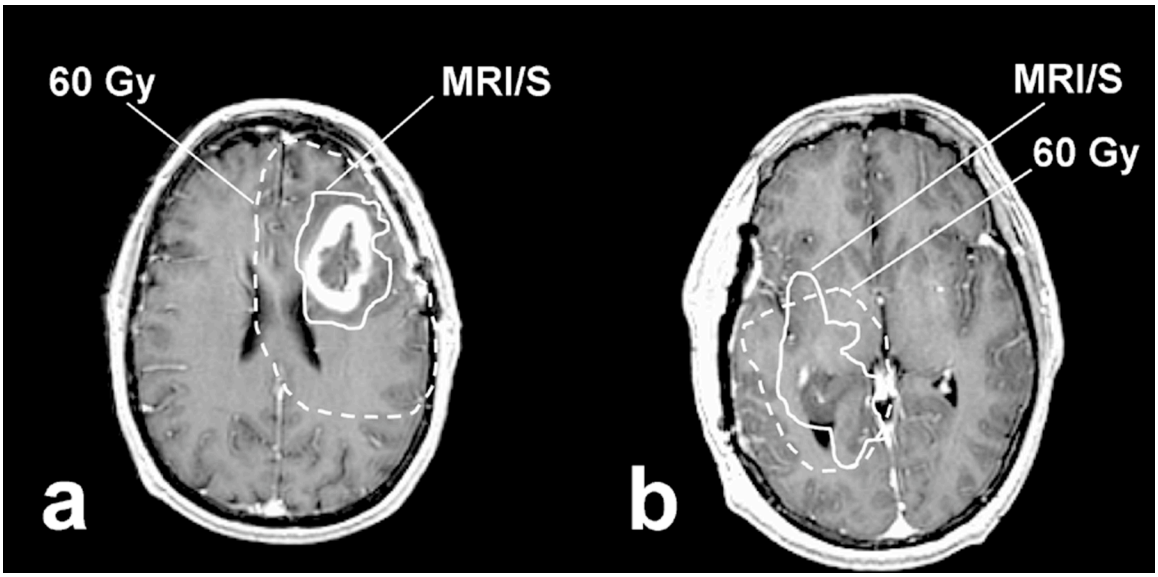

Figure 4.7 Examples comparing the volume of a combined anatomic and metabolic region of interest (MRI/S; solid line) and the actually delivered 60 Gy (dashed line). (a) Typical volume of 60 Gy compared with that of MRI/S, which had a large portion of normal-appearing brain tissue that received 60 Gy; (b) case in which MRI/S extended beyond 60 Gy.

4.4 Discussion

We have retrospectively evaluated whether a new approach for RT target definition that adds MR based information on metabolic abnormality (CNI2) to the conventional RT target definition is likely to be sufficient in defining the possible regions of new or increasing CE that develop following conventional 3D conformal RT.

The conventional target definition and dose prescription for RT as applied in the herein evaluated GBM patients status post surgical resection was found to cover the majority of MRSI metabolic disease. However, the prescribed dose of 60 Gy did not cover all pre-RT tumor extensions with tumor suggestive metabolic activity in 48% (11/23) of the patients (Table 4.1). This CNI2 extension ranged in volume and was rather small in most cases but extended as much as 4 cm beyond the 60 Gy isodose line and was found to be covered by RT doses of at least 30 Gy. Based on our recurrence analysis with respect to the pre-RT MRI/S volume, we believe that this CNI2 extension outside the 60 Gy volume is not the initial focus of tumor recurrence, but we observed that CE seemed to expand, i.e. the tumor grew into these regions during FU.

All recurrence patterns analyzed in this study were local, and no distant failures were observed. These findings are consistent with prior studies that have shown that the vast majority of recurrences occur within 2 cm of the original tumor site (77,95,96) or "in field" (more than 80% of the tumor recurrence residing within the prescription isodose) (97). The results summarized in Table 4.3 show that the increased CE, as a presumed sign of tumor recurrence, occurred both within and beyond the prescribed dose of 60 Gy. Increased CE was found within the region of the CNI2 that extended beyond the 60 Gy isodose line in three patients. As pointed out above, tumor seems to be growing into these regions rather than originating from there. In other words, tumor growth or recurrence as demarcated by breakdown of the blood-brain barrier is confined to the metabolically active tumor regions as assessed prior to RT. It is not expected that the inclusion of the CNI2 volume into the 60 Gy volume would improve tumor control but spare normal tissue.

The MRI/S volume may be considered as a new way to define custom shaped target volumes which seems to contain the recurrence effectively within the first year of RT. We have shown that 89 % of the patients exhibited recurrence patterns contained within the pre-RT MRI/S volume (Table 4.4). This suggests that if we had reshaped the target definition using the MRI/S volume, we could have reduced the irradiated volume to morphologically and metabolically normal brain tissue, but still covered the recurrent tumor. Whether this approach would result in the same pattern of recurrence still remains to be assessed in a clinical trial. In particular, it remains to be shown that reducing tumor margins would not result in worsened tumor control if one assumes that the herein described lack of recurrence in normal appearing brain may be related to the efficacy of RT.

Our findings have importance for the target definition of high-grade gliomas and low-grade gliomas alike (98). Conventionally employed large uniform margins have been historically utilized due to the inability to demarcate “invisible” tumor extent. They typically expose a rather large volume of normal appearing brain arguably unnecessary. The new approach of custom shaped margins in accordance to metabolic and morphologic abnormality will allow for the sparing of normal tissue as well as reducing the overall volume of tissue radiated, and thereby reduce side effects. This will allow the exploitation of focal therapies including delivery if high focal doses to tumor subregions that deem radioresistant or particularly aggressive, i.e. high proliferative potential. Such regions can be demarcated by MRSI and/or other metabolic imaging techniques either prior to RT or at the end of RT by means of assessing a serial response pattern. Studies in this regard are currently ongoing.

Adverse side effects following brain irradiation and the resulting compromised clinical outcome can be minimized by limiting the volume of irradiated brain tissue. Such central nervous system side effects include impaired intellectual function and hypothalamic-pituitary dysfunction. The risk of radiation necrosis is rather unlikely following a conventional dose of 60 Gy delivered in standard fractionation of 2 Gy/30 fractions but rises rapidly as the radiation dose increases above 60 Gy (99).

We found for the herein evaluated patient population that the volume of brain tissue that was treated with 60 Gy but appeared morphologically and metabolically normal was rather large, nearly double the median volume of the MRI/S. With respect to local control, all patients' recurrence seemed to originate within the combined MRI/S abnormality except for one patient with debatable outcome due to significant tissue shift (Fig. 6). This suggests that tissue sparing seems feasible using modern RT coupled with customized target definition that is based upon the combined morphologic/metabolic imaging.

Current technical limitations in regard to the size and shape of the PRESS region prescribed for MRS evaluation are likely to be overcome shortly with the design of more effective suppression pulses that will allow the size of the selective volume to be adjusted to different head sizes and shapes, allowing the spectroscopic analysis of larger regions of supratentorial brain tissue.

In conclusion, increased CE during FU was observed to occur within the combined MRI/S volume as defined at pre-RT in all but one patient, for whom a large cyst caused a significant tissue shift. This suggests that the definition of RT target volumes according to the morphologic and metabolic abnormality (MRI/S) may be

sufficient for RT targeting. MRSI in combination with MRI may thus allow for a reduction and custom shaping of currently employed target volumes for RT in brain gliomas which would reduce the dose exposure to uninvolved normal brain tissue.

Chapter 5: Implementation of 3T Lactate-Edited 3D ^{1}H MR Spectroscopic Imaging with Flyback Echo-Planar Readout for Patients with Gliomas

5.1 Introduction

Lactate is a metabolic marker that is observed in many brain pathologies (100,101). Neoplastic processes that are present in tumors have low oxygen supply and depend on non-oxidative glycolysis for energy production (65). This means that lactate can be considered as an indicator of anaerobic glycolysis and reduced cellular oxygenation, which is of interest for evaluating response to radiation or other therapies. The potential for identifying regions of metabolic stress and ischemic area in brain means that in vivo measurements of lactate are of interest in patients with a number of different brain pathologies. Previous studies performed at 1.5 Tesla (1.5T) have shown that the presence of lactate and lipid peaks in ^{1}H magnetic resonance spectroscopic imaging (MRSI) data is associated with a diagnosis of high-grade tumor (102,103). Elevated signals from lactate and lipid were associated with short survival in patients with glioblastoma multiforme (GBM) who were evaluated either prior to surgery or radiation treatment at 1.5T (104,105). In these cases, increased lactate was interpreted as an indication of increased tumor metabolism and growth (106,107). The detection of lactate is thus of interest for evaluating prognosis and response to therapy in brain tumor patients.

^{1}H magnetic resonance spectroscopy (MRS) of lactate demonstrates two resonances: a doublet at 1.3 ppm from methyl protons (CH_3) and a quartet at 4.1 ppm from methine protons (CH). The methyl protons and the methine protons are weakly coupled to each other with a J-coupling constant of 6.93 Hz. For proton in vivo spectroscopy, the methyl doublet has been the target for lactate detection because the methine peaks are close to the water resonance and are not usually visible because of their relatively low signal intensity. Despite this advantage, the methyl doublet can be difficult to quantify because of lipid peaks, which overlap in the range of 0.9 to 1.3 ppm. In order to overcome this problem, a number of techniques have been developed to measure and separate the lactate doublet from lipid resonances (108-110).

One such technique is based on spectral editing using dual BASING (BAnd Selective INversion with Gradient dephasing) pulses (108). This technique allows for simultaneous detection of lactate at 1.3 ppm as well as uncoupled metabolites such as choline (Cho), creatine (Cr), N-acetyl-aspartate (NAA) and lipid. Based on J-difference editing, this technique exploits the fact that the phase of the doublet depends on the carrier frequency of the BASING pulse acting on the quartet at 4.1 ppm, which is weakly coupled to the doublet. The BASING pulse, which is a frequency selective inversion pulse surrounded by bipolar crusher gradients on orthogonal axes, places the methine quartet within the BASING inversion band for the first cycle (edit-on), while the carrier frequency of the BASING pulse is shifted in the second cycle so that the quartet is removed from the inversion band (edit-off) (108). As a result, the doublet becomes in-phase in the first cycle and 180 degree out-of-phase in the second cycle relative to uncoupled spins for echo time TE = 144 ms. Summing the two data sets provides only

uncoupled spins including Cho, Cr, NAA and lipid, whereas subtracting them renders only lactate (Figure 5.1c).

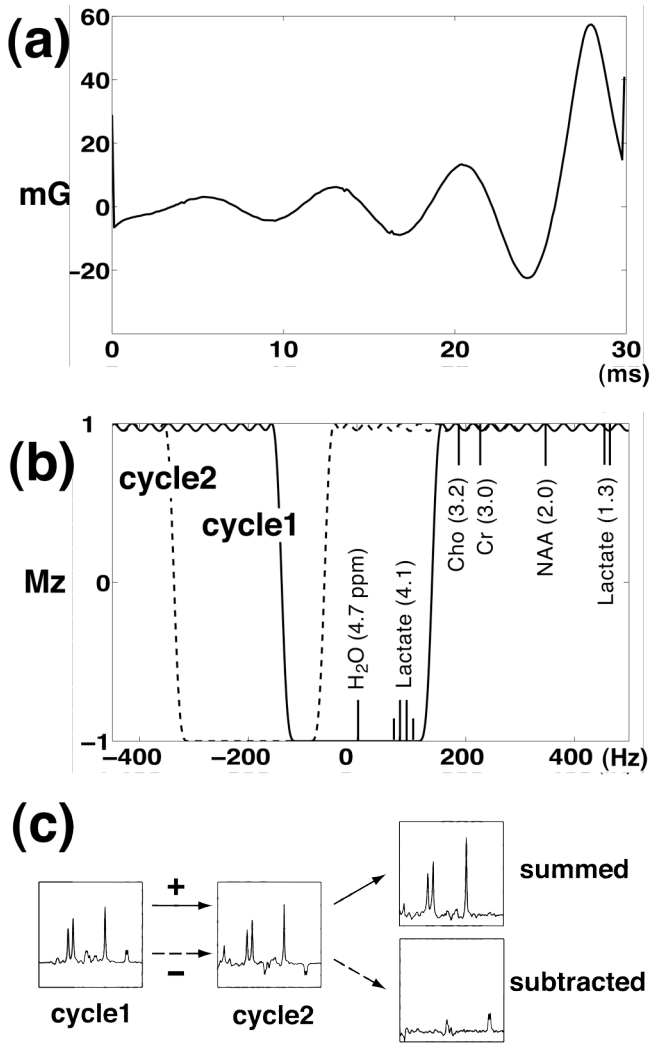

Figure 5.1 The new BASING pulse waveform designed for 3T (a) and its inversion profile (b). Carrier frequency of the second cycle was shifted 198 Hz from the first cycle so that the lactate methine quartet was placed in either the passband or the stopband. As a result, lactate doublet is upright in one cycle and inverted in other cycle, so that summing the two data sets produces uncoupled resonances while subtracting them produces lactate resonance (c).

Lactate editing combined with PRESS (Point RESolved Spectroscopy) localized 3D MRSI has been applied to glioma patients at 1.5T for non-invasive detection of lactate and other brain metabolites (103-105). These studies demonstrated the detection of lactate as well as Cho, Cr, NAA and lipid, and suggested that in vivo measurement of lactate as well as other MR-derived parameters may help in diagnosis and proper therapy selection for glioma patients. Although the increased signal strength at higher field is expected to enhance the sensitivity of brain metabolites including lactate, the detection of brain lactate using ^{1}H MRS based on J-difference editing at 3 Tesla (3T) scanner has not been reported. Several studies have reported their unsuccessful attempts at measuring lactate in brain tumor patients using single voxel PRESS-localized MRS at 3T (111,112). The poor lactate detection that was observed at 3T in these studies was due to chemical shift mis-registration artifact caused by the limited bandwidth of refocusing pulses used for the localization of spectroscopic data.

Several studies have investigated the signal cancellation of J-coupled resonance due to the chemical shift difference between J-coupled spin partners in PRESS MRSI sequence in the context of lactate and GABA (113,114). This artifact is produced because spatially selective RF pulses cause a relative shift in the location of the selected volume for J-coupled resonances, thereby leading to net signal loss when the final signal is contributed from different regions. Kelley et al. (113) demonstrated in phantoms that BASING pulses incorporated into non-editing PRESS sequence reduced the artifact for the detection of lactate methyl resonance in single voxel and MRSI data. For our editing scheme, this artifact may happen in the second cycle with BASING editing off, which is

basically regular J-evolution. In the present study, we sought to eliminate this artifact by using higher bandwidth RF pulses since the spatial offset due to chemical shift difference is inversely proportional to RF bandwidth. In addition, we over-prescribed PRESS-localized volume and applied high bandwidth saturation pulses in order to further minimize this artifact.

The clinical use of lactate edited MRSI based on J-difference editing has been limited by the requirement of two successive acquisitions per phase encoding step and the acquisition time which has typically been 20 minutes (103). Flyback echo-planar spectroscopic imaging has been used to allow the acquisition of MRSI data in a shorter scan time. Cunningham et al. (115) demonstrated the feasibility and potential of MRSI data acquisition at 3T with high spatial resolution and large coverage in a short scan time with flyback echo-planar readout gradient waveforms.

The purpose of this study was to implement a lactate edited 3D PRESS ^{1}H MRSI sequence at 3T with new high bandwidth 180° pulses, new BASING pulses and a flyback echo-planar readout gradient in order to allow a clinically suitable scan time of 10 minutes and demonstrate the feasibility of using this sequence for the detection of brain lactate as well as Cho, Cr, NAA and lipid in patients. We addressed the effect of chemical shift artifact on lactate signal with different PRESS over-prescription (over-PRESS) factors and compared the metabolite SNR and its ratio of the lactate edited MRSI data between a flyback echo-planar readout gradient method and conventional MRSI with elliptical k-space sampling. The method was then applied to patients with gliomas in order to determine whether it could detect lactate within lesions.

5.2 Materials and Methods

5.2.1 Sequence Development and Implementation

Pulse sequence development and implementation were performed using the GE pulse sequence development environment (version 12x). The new 3T dual BASING pulses were modified from the BASING pulses developed in our laboratory for application at 1.5T (108) to accommodate the increased spectral range at 3T. The new waveform, derived from the Shinnar-Le Roux algorithm (116), had a duration of 30 msec and peak amplitude of 57 mG (Figure 5.1a). The inversion and transition bandwidth of the waveform were 230 Hz and 55 Hz, respectively (Figure 5.1b). The sequence was modified so that the center of the BASING inversion band was placed at water (4.7 ppm) for the first cycle and shifted 198 Hz for the second cycle. As a result, the lactate methine peak (4.1 ppm) was placed within the BASING inversion band for the first cycle and removed from it in the subsequent cycle (Figure 5.1b). The PRESS localization scheme incorporated shortened (6.5 ms) and higher-bandwidth (1.5 kHz) 180º refocusing pulses that were designed to minimize the effect of chemical shift mis-registration artifact at 3T. The center frequency of 90º and 180º pulses was placed in the middle of lactate methyl and methine resonances at 2.64 ppm. New high bandwidth Very Selective Suppression (VSS) pulses were custom-designed for 3T with an 8.8 kHz bandwidth and 2 msec duration. The resulting 3D MRSI sequence consisted of a PRESS scheme incorporating new high bandwidth VSS pulses, higher-bandwidth 180º pulses, new 3T dual BASING pulses positioned after the first and second 180º pulses and a flyback echo-planar readout gradient. Table 5.1 summarizes the various parameters for BASING, VSS and PRESS pulses between the 1.5T and the newly designed 3T (88,108,117).

Table 5.1 Comparison of BASING, VSS and PRESS pulse parameters between the 1.5T and the newly implemented 3T sequence.

		BASING		VSS		PRESS	
	Peak amplitude	Inversion BW	Transition BW	BW	Duration	90° pulse BW	180° pulse BW
1.5T	30 mG	100 Hz	55 Hz	6.5 kHz	3 msec	2,400 Hz	933 Hz
3T	57 mG	230 Hz	55 Hz	8.8 kHz	2 msec	2,400 Hz	1,500 Hz

BW: Bandwidth

5.2.2 Estimation of Chemical Shift Artifacts with Over-PRESS Factors

The effect of chemical shift artifacts on the excitation profiles of lactate methyl and methine resonances was estimated by calculating the spatial offset of each resonance using the following equation (118):

$$\Delta x = \frac{(w - w_0)}{BW_{RF}} \times X_{BOX} \qquad [5.1]$$

where Δx is the spatial offset of the excitation profile for a metabolite with resonance frequency w, from the carrier frequency, w_0; BW_{RF} is the bandwidth of the PRESS RF excitation pulse in the given direction (90° or 180°); and X_{BOX} is the width of the excited spectral region in that direction. Using Eq. [5.1], we estimated the excitation profiles of lactate methyl and methine resonances for 1.2, 1.5 and 1.7 PRESS over-prescription (over-PRESS) factors, defined as the ratio of the linear dimension of the excited volume to the prescribed volume. For simplicity, we considered only the x-y plane and assumed that the prescribed region is a 2D box with a size of 80x80 mm.

5.2.3 Spectroscopic Imaging

All spectroscopic imaging data were acquired using a 3T Signa HDx (v12x) MR scanner (GE Healthcare, Milwaukee, WI) and an 8-channel phased array head coil. The spectroscopic imaging data were acquired with PRESS volume localization with an over-PRESS factor between 1.2 and 1.7. The over-PRESS factor was achieved by reducing the amplitude of the slice selection gradients. Chemical shift-selective saturation (CHESS) pulses were used for water suppression. VSS pulses of width 40 mm were placed on all sides of the prescribed volume to define the edges of the selected volume, and six additional graphic VSS bands were used in order to further improve the suppression of subcutaneous lipids for volunteer and patient scan. High-order shimming was performed prior to the MRSI data acquisition to optimize the magnetic field homogeneity. In order to estimate the sensitivity profile of each coil element, proton density weighted gradient-echo (GRE) images were acquired using the manufacture-provided parallel imaging (ASSET) calibration sequence (TR/TE=150/20 ms).

5.2.4 Chemical Shift Artifacts with Different Over-PRESS Factors in a Phantom

To study the effect of chemical shift artifacts for different over-PRESS factors and to determine an optimal over-PRESS factor for the new sequence, empirical data were obtained from a GE head MRS phantom containing 5 mM lactate as well as Cho (3 mM), Cr (10 mM) and NAA (12.5 mM) (88). 3D MRSI data were acquired with the excited volume of 80x80x40 mm^3 using over-PRESS factors of 1.2, 1.5 and 1.7 and VSS pulses around the prescribed volume (TR/TE=1104/144 ms, FOV=16x16x16cm, voxel size=1x1x1cm, flyback echo-planar readout gradient in SI direction, 712 dwell points,

988 Hz bandwidth). In order to evaluate the variation in lactate signal across the excited volume for different over-PRESS factors, the mean value of lactate SNR was calculated from the right, left, middle, anterior and posterior of the central two slices (Figure 5.2). In addition, the peak height ratio of choline to NAA (Cho/NAA) was calculated and compared for three over-PRESS factors.

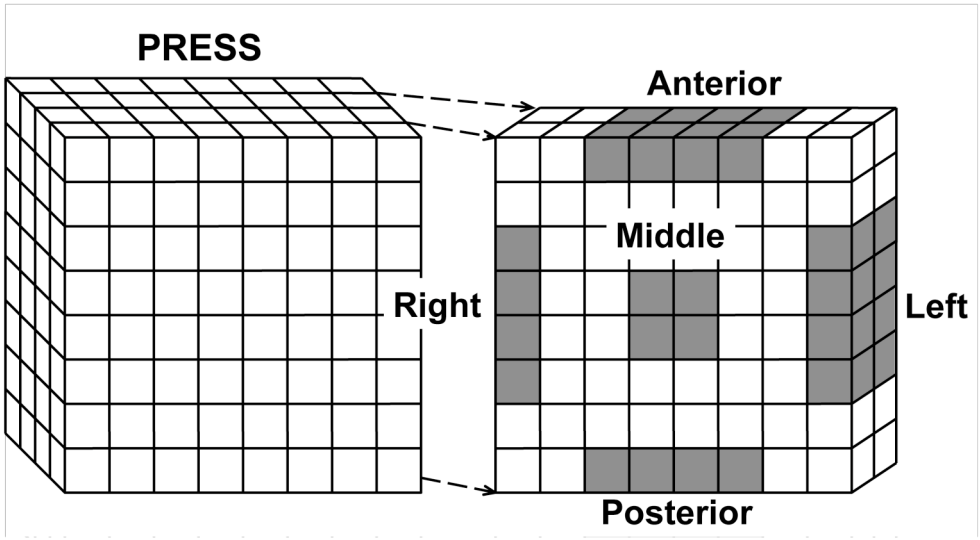

Figure 5.2 Lactate edited 3D PRESS MRSI was applied to study the effect of chemical shift artifacts on lactate signal and other brain metabolites. The mean value of lactate SNR and choline to NAA ratio were calculated from the right, left, middle, anterior and posterior voxels of the central two slices.

5.2.5 Comparison between the Conventional Phase Encoding and Flyback Readout Gradient Methods

In order to compare signal quality between the conventional phase encoding and flyback readout gradient methods, a phantom and two volunteers were scanned using lactate edited PRESS MRSI with both the conventional phase encoding

(TR/TE=1104/144 ms, FOV=12x12x8cm, nominal voxel size=1x1x1cm (1 cc), effective resolution=2.5 cc, total acquisition time=19 min, 1024 dwell points, 2000 Hz bandwidth) and the flyback echo-planar readout gradient applied in SI (z) dimension (TR/TE=1104/144 ms, FOV=16x16x16cm, voxel size=1x1x1cm (1 cc), total acquisition time=9.5 min, 712 dwell points, 988 Hz bandwidth). An over-PRESS factor of 1.5 was chosen for both methods. For the conventional MRSI method, an elliptical k-space sampling was applied so that the radius of the ellipsoid was chosen to reduce the acquisition time to approximately one-half of that of the full rectangular sampling (103). The number of phase encoding steps was reduced from 1152 (12×12×8) to 512 through zero filling the appropriate k-space points outside a normalized ellipsoidal radius of 1.2 (119). The SNR of Cho, Cr, NAA and lactate were calculated from the middle 4 voxels of the central two slices for the phantom, and the SNR of Cho, Cr and NAA in normal appearing white matter (NAWM) for the volunteers. The SNR of the flyback method was normalized to compensate for different scan times and effective spatial resolutions between the flyback and conventional MRSI methods by:

$$nSNR_{flyback} = SNR_{flyback} \cdot \frac{\sqrt{TA_{conventional}}}{\sqrt{TA_{flyback}}} \cdot \frac{\Delta V_{conventional}}{\Delta V_{flyback}} \qquad [5.2]$$

where $nSNR_{flyback}$ is the normalized SNR of flyback data, $SNR_{flyback}$ is the raw SNR of flyback data, TA is the total acquisition time, and ΔV is the effective spatial resolution. The reduced elliptical k-space sampling in the conventional MRSI method resulted in an increase in the effective spatial resolution (120,121). A recent study has compared the effective spatial resolution between the elliptical k-space sampling in the conventional phase encoding method and the rectangular k-space sampling in the flyback method (119). The authors used the spatial response function (SRF) generated by Fourier

reconstruction in order to calculate the effective volume for each method and reported that the effective spatial resolutions for the conventional and flyback methods were 2.473 cm^3 and 1.014 cm^3, respectively. This resulted in an additional factor of 2.439 being required to correct for the difference between the effective spatial resolution of the conventional and flyback methods:

$$\Delta V_{conventional} = 2.439\ \Delta V_{flyback} \qquad [5.3]$$

This ratio was consistent with the previous finding, obtained by comparing the SNR of NAA in NAWM between the two methods (122). Considering both the effective spatial resolution and differences in scan time between the conventional and flyback methods, a factor of 3.4 was used to normalize the SNR of the flyback method.

$$nSNR_{flyback} = 3.4 \times SNR_{flyback} \qquad [5.4]$$

5.2.6 Patient Data Acquisition

A total of ten patients (8 male, 2 female, median age 55, range 41-64) with GBM were included in this study. Some patients had more than one examination and a total of thirty four scans from these patients were examined to demonstrate the feasibility of using the new lactate edited 3D MRSI sequence for the detection of lactate in brain tumor at 3T. All patients were scanned using 3T lactate edited PRESS 3D MRSI sequence with the flyback echo-planar readout gradient applied in SI dimension using an over-PRESS factor of 1.5 (TR/TE=1104/144 ms, FOV=16x16x16cm, voxel size=1x1x1cm, total acquisition time=9.5 min, 712 dwell points, 988 Hz bandwidth). The MRI protocol included an axial T2-weighted FLAIR (FLuid Attenuated Inversion Recovery) sequence (87) with 3-mm slice thickness and axial pre- and post-Gadolinium-DTPA T1-weighted

SPGR (SPoiled Gradient Recalled) images with 1.5-mm thickness. All patients provided informed consent as approved by the committee on human research at our institution.

5.2.7 Data Processing and Quantification

The method used for spectral quantification has been described previously (89). In brief, the 3D MRSI data with the conventional phase encoding were reconstructed by processing each of the spectra from the eight-channel coil individually, apodizing with a 4 Hz Lorentzian filter in the time domain, zero-filling to 1024 points, applying phase and frequency correction, and then removing residual water and baseline. The individual data were Fourier-transformed to produce a 3-D spatial array of spectra and combined using in-house developed software that weights the data by their coil sensitivities from the low resolution proton density weighted images (117,123). The two cycles of data were then either summed or subtracted to produce a 3D array of summed or subtracted spectra.

The 3D MRSI data with the flyback echo-planar readout were reconstructed and combined in the same way as the data with the conventional phase encoding, but with the application of an additional linear phase correction in the SI dimension of spectral k-space to prevent spatial chemical shift artifacts (115). To reconstruct the data acquired with the flyback echo-planar readout gradient, only samples from the flat part (plateau) of the gradient waveforms were used.

The SNR of brain metabolites was calculated using the previously published method (124). The region of 100 spectral points without metabolite signal was selected to estimate the standard deviation of the noise. Sub-regions with a size of 20, 40, and 80 points were made and located at the beginning of the selected region. The location of the

sub-region was incremented by 1 point until it reached the end of the selected region, resulting in a total of 81, 61, and 21 divisions, respectively. For each sub-region, the standard deviation (SD) was computed, the minimum SD was taken for each division, and the minimum SD of the divisions was used for the final standard deviation of noise. The SNR of peak height over the standard deviation of noise was calculated for Cho, Cr, NAA and lactate.

In order to quantify lactate level in patients, median lactate SNR was estimated for each examination. Lactate peaks with SNR equal to or greater than 4 were only included in calculating the median lactate SNR. The estimation of lactate SNR was confined to the lactate appearing in contrast enhancing lesion (CEL) or T2 hyperintense region (T2h). The lactate found in resection cavity, necrotic region or cerebrospinal fluid was excluded from the analysis.

5.3 Results

5.3.1 Estimation of Chemical Shift Artifacts with Over-PRESS Factors

Figure 5.3 illustrates the effect of chemical shift mis-registration artifact on the lactate excitation profiles for 1.2 and 1.5 over-PRESS factors. Using a 96x96 mm excited box with an 1.2 over-PRESS factor, 1500 Hz and 2400 Hz bandwidth of the PRESS 180° (RL direction) and 90° pulses (AP direction), respectively, 170 Hz shift of lactate methyl resonance (1.3 ppm) from the carrier frequency (2.64 ppm), and the directionality information of the chemical shift artifact, Eq. [5.1] estimated the lactate methyl excitation profile (dashed line) to be shifted from the carrier frequency excitation profile (solid line)

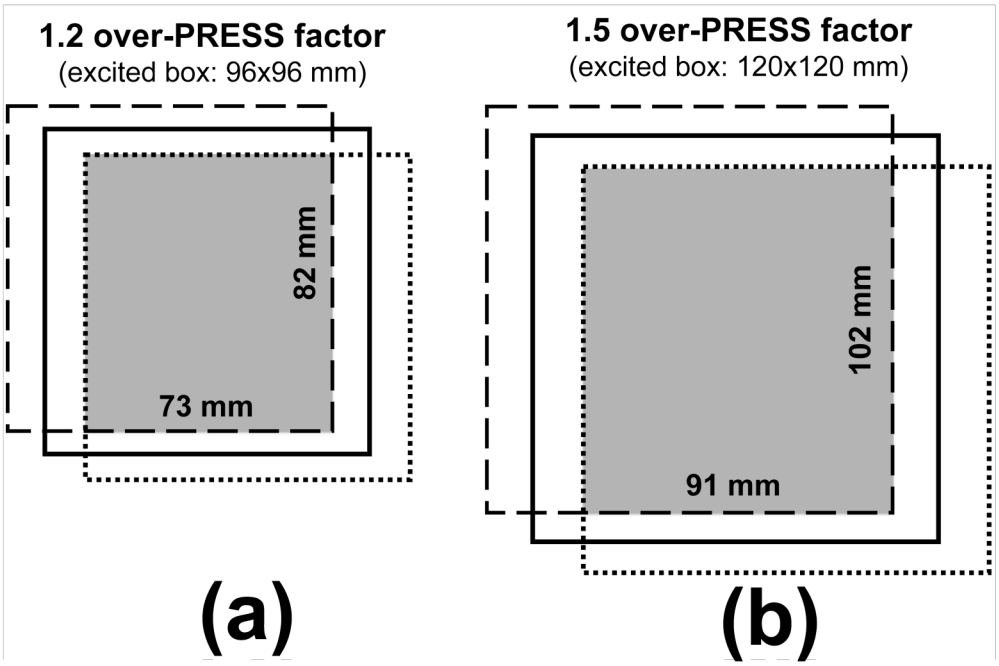

Figure 5.3 The illustration of chemical shift mis-registration artifact for 1.2 and 1.5 over-PRESS factors. The 1.2 over-PRESS factor produces shifted excitation profiles for lactate methyl (dashed line) and methine (dotted line) resonances from the excitation profile of carrier frequency (solid line), resulting in a 73x82 mm region with the simultaneous excitation of two lactate resonances (a). Similarly, the 1.5 over-PRESS factor produces a 91x102 mm region with the simultaneous excitation of two lactate resonances (b) and therefore smaller chemical shift artifacts compared to the 1.2 over-PRESS factor.

by 11 mm in RL direction and 6.8 mm in AP direction toward the top-left corner and the lactate methine excitation profile (dotted line) by 12 mm in RL direction and 7.5 mm in AP direction toward the bottom-right corner (Figure 5.3a). As a result, it produces a region with a size of 73x82 mm (highlighted box) where both the lactate methyl and methine resonances are equally excited and a portion of the prescribed box in RL direction where only one of the lactate resonances is excited. Similarly, using an 120x120

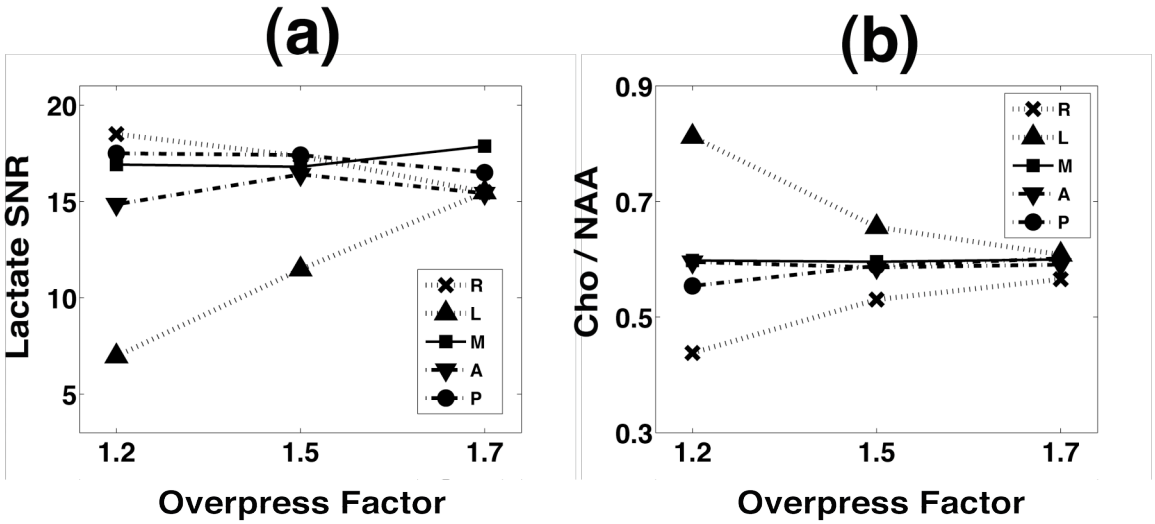

Figure 5.4 The effect of chemical shift artifacts on brain metabolite signal was evaluated using a phantom. Mean lactate SNR (a) and choline to NAA ratio (Cho/NAA) (b) were compared between the right (R), left (L), middle (M), anterior (A) and posterior (P) voxels of the excited volume. As the over-PRESS factor increased from 1.2 to 1.7, the chemical shift artifact lessened.

mm and 136x136 mm excited box with the over-PRESS factors of 1.5 and 1.7, respectively, the 1.5 over-PRESS factor produces a 91x102 mm region (Figure 5.3b) and the 1.7 over-PRESS factor a 104x116 mm region with the simultaneous excitation of two lactate resonances. Given the size of the prescribed box (80x80 mm), the chemical shift artifact is expected to be most pronounced with an 1.2 over-PRESS factor and more accentuated in RL direction compared to AP direction due to the lower bandwidth of 180º pulse (1.5 kHz) used for selection in RL direction compared to the bandwidth of 90º pulse (2.4 kHz) used for selection in AP direction. Our phantom data were consistent with this observation in that the chemical shift artifact manifested as the signal

cancellation of lactate doublet was most apparent in the left column and improved with increases in the over-PRESS factor (Figure 5.4 and Figure 5.5).

Table 5.2 Comparison between three over-PRESS factors.

	over-PRESS factor		
	1.2	1.5	1.7
Lactate SNR	15 (4.7)	16 (2.5)	16 (1.1)
Cho/NAA	0.60 (0.14)	0.59 (0.04)	0.59 (0.02)

The mean and standard deviation of lactate SNR and choline to NAA ratio (Cho/NAA) across the five regions of the excited volume for different over-PRESS factors. The numbers inside parenthesis indicate the standard deviation.

5.3.2 The Effect of Chemical Shift Artifacts on Metabolite Signal in Phantom

As expected, the effect of chemical shift artifacts on lactate signal variation across the exited volume was reduced as the over-PRESS factor increased. Mean lactate SNR from the right, left, middle, anterior and posterior voxels are plotted against the over-PRESS factors of 1.2, 1.5 and 1.7 in Figure 5.4. The mean and standard deviation of lactate SNR from the five locations are summarized in Table 5.2. The mean lactate SNRs were similar for different over-PRESS factors. In contrast, the standard deviation of lactate SNR decreased with increases in the over-PRESS factor, indicating that the chemical shift mis-registration artifact lessened with increase in the over-PRESS factor. The lactate SNR from the left voxel showed the largest variation across the three over-PRESS factors and rapidly increased with increases in the over-PRESS factor. The differences between the lactate SNR from the left and right voxel were 12 and 6 for the

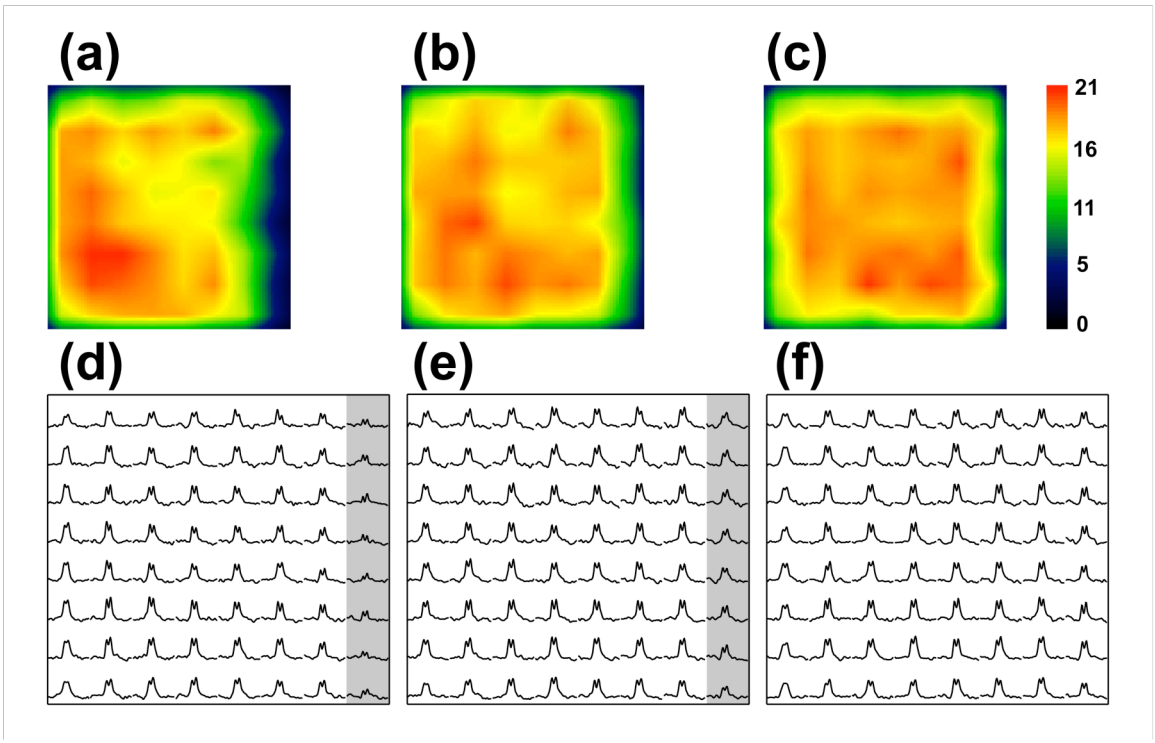

Figure 5.5 The distribution of lactate methyl doublet from MRSI data using phantom. The top images show the color-maps of lactate SNR for the over-PRESS factors of 1.2 (a), 1.5 (b) and 1.7 (c). The corresponding spectra zoomed-in around lactate doublet are shown in the bottom for the over-PRESS factors of 1.2 (d), 1.5 (e) and 1.7 (f). The lactate doublet in the left column (highlight) had lower intensity compared to other regions of the PRESS volume for the over-PRESS factors of 1.2 and 1.5. The overall uniformity of lactate intensity increased with increases in the over-PRESS factor.

over-PRESS factors of 1.2 and 1.5, respectively and hardly noticeable for the over-PRESS factor of 1.7 (Figure 5.4a). The Cho/NAA displayed a similar pattern. The Cho/NAA values from the different regions of the excited volume converged as the over-PRESS factor increased, whereas the mean Cho/NAA from the five regions were similar across the three over-PRESS factors (Table 5.2). Figure 5.5 shows the color-maps of

lactate SNR and the corresponding lactate spectra for the three over-PRESS factors. The spectra were taken from the central slice of the PRESS 3D volume. The color-maps were generated by spatially interpolating lactate SNR values to the resolution of anatomical images using a linear kernel. The map with an 1.2 over-PRESS factor showed a large signal drop-off in the left region of the spectra, which was alleviated with an 1.5 over-PRESS factor. The map with an 1.7 over-PRESS factor showed fairly uniform signal intensity across the entire region.

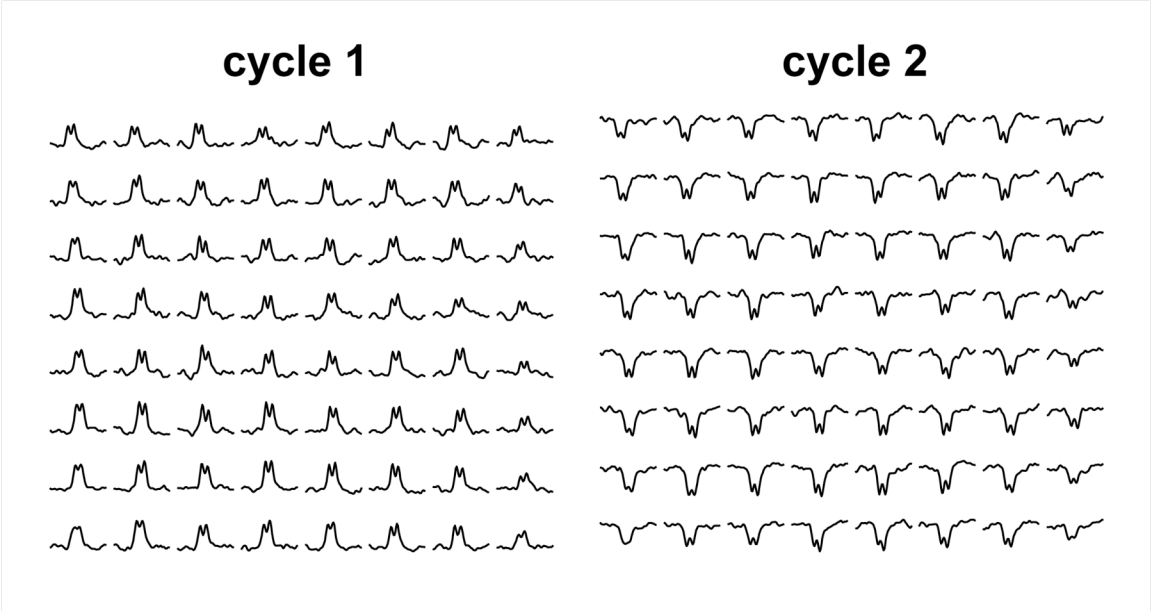

Figure 5.6 Lactate spectra from the first (edit-on) and second (edit-off) cycles acquired from phantom using the over-PRESS factor of 1.5. The use of higher-bandwidth 180º refocusing pulses in combination with over-prescription and high bandwidth VSS pulses minimized signal cancellation across the excited volume and provided relatively uniform lactate signal for both datasets.

The artifact caused by the spatial interference of lactate methyl and methine spins appeared to be minimal. Figure 5.6 shows MRSI datasets zoomed-in around lactate doublet from the BASING edit-on (1st cycle) and edit-off (2nd cycle) scans with an 1.5 over-PRESS factor. The lactate doublets from the first and second cycles were relatively uniform throughout the excited volume with a slight signal drop-off in the left column. The intensity and distribution of lactate from the second cycle were similar to those from the first cycle, except that they are 180° out-of-phase to each other. It indicates that the use of higher-bandwidth 180° pulses in combination with over-PRESS and high bandwidth VSS pulses was able to minimize the chemical shift artifact.

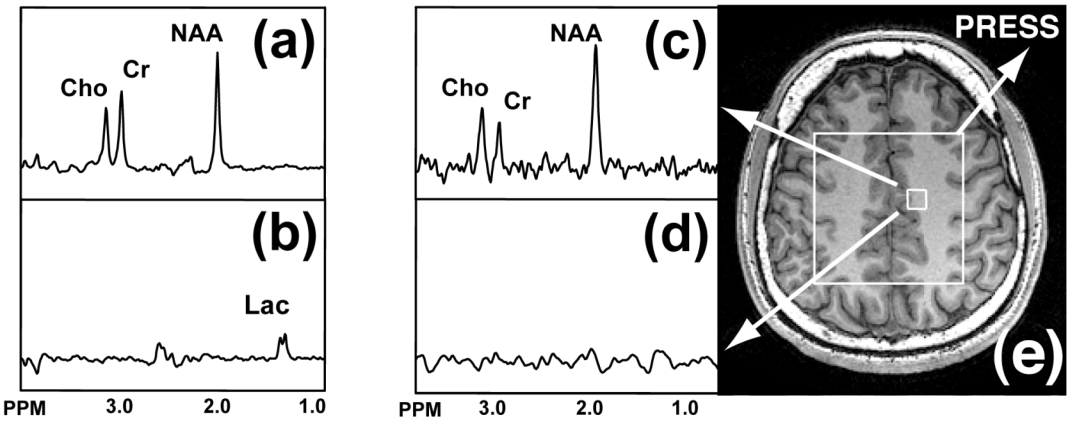

Figure 5.7 Lactate edited spectra with a flyback gradient in a phantom (a, b) and a volunteer (c, d). Lactate is detected in the subtracted spectrum of phantom (b), and uncoupled resonances are produced in summed spectra in both phantom (a) and volunteer (c). T1-weighted image from the volunteer (e) shows the PRESS box and the voxel chosen for the spectra.

Table 5.3 The median SNR values and metabolite ratios of brain metabolites for raw flyback, normalized flyback and conventional MRSI methods.

	phantom (n=1)			volunteer (NAWM, n=2)			patients (NAWM, n=33)	
	rFB	nFB	cMRSI	rFB	nFB	cMRSI	rFB	nFB
Cho	50	173	208	10	35	43	10	34
Cr	60	207	262	8	29	39	8	28
NAA	84	288	349	19	66	85	17	59
Lac	18	61	78				5†	17†
Cho/NAA	0.60		0.60	0.53		0.51	0.59	
Lac/NAA	0.21		0.22				0.30†	

NAWM: normal appearing white matter; rFB: raw flyback; nFB: normalized flyback; cMRSI: conventional MRSI with elliptical k-space sampling; Cho/NAA: choline to NAA ratio; Lac/NAA: lactate to NAA ratio

†Lactate in patients was measured from the contrast enhancing lesion or T2 hyperintense region and lactate in necrosis or resection cavity was excluded.

5.3.3 Comparison between the Conventional Phase Encoding and Flyback Readout Gradient Methods

Lactate edited MRSI spectra acquired with a flyback readout gradient demonstrated excellent detection of uncoupled spins in the summed spectra and lactate in the subtracted spectra for phantoms and volunteers. The over-PRESS and use of high bandwidth VSS pulses provided minimal chemical shift mis-registration. Figure 5.7 shows an example of spectroscopic voxels from the lactate edited MRSI with a flyback echo-planar readout gradient in a phantom (a, b) and a volunteer (c, d). In the subtracted spectra (b, d), the lactate doublet at 1.3 ppm was observed in the phantom data (b), but

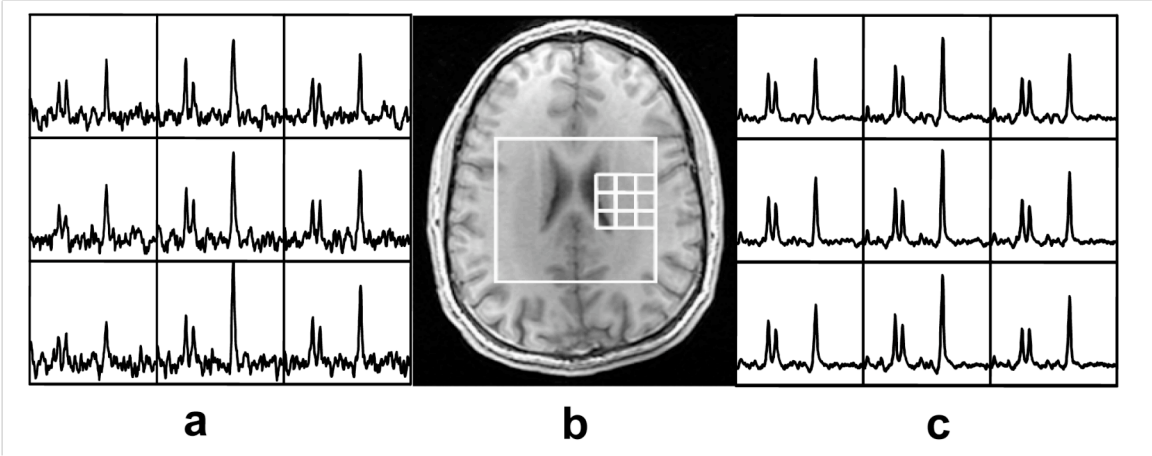

Figure 5.8 Comparison of MRSI data between the flyback-gradient method (a) and the conventional elliptical MRSI method (c) from a volunteer. T1-weighted SPGR (b) shows PRESS box and the spectral array.

not in the healthy volunteer (d). Cho, Cr and NAA were summed (a, c) or removed (b, d) for both the phantom and volunteer. The median raw SNR of Cho, Cr and NAA from the flyback method was 50, 60 and 84 for phantom and 10, 8 and 19 for volunteers, respectively. The median raw SNR of lactate from the flyback method was 18 for the phantom. The median normalized SNR values of brain metabolites and their ratios from the flyback method are compared to those from the conventional phase encoding method for phantom and volunteers in Table 5.3. The signal reduction for the flyback method compared to the conventional phase encoding ranged from 17 % to 22 % in the phantom and 19 % to 25 % in volunteers for Cho, Cr, NAA and lactate (Table 5.3). An example of spectra from a volunteer comparing the two MRSI methods is shown in Figure 5.8.

5.3.4 Patient Data from the Lactate-Edited 3D MRSI with a Flyback Gradient

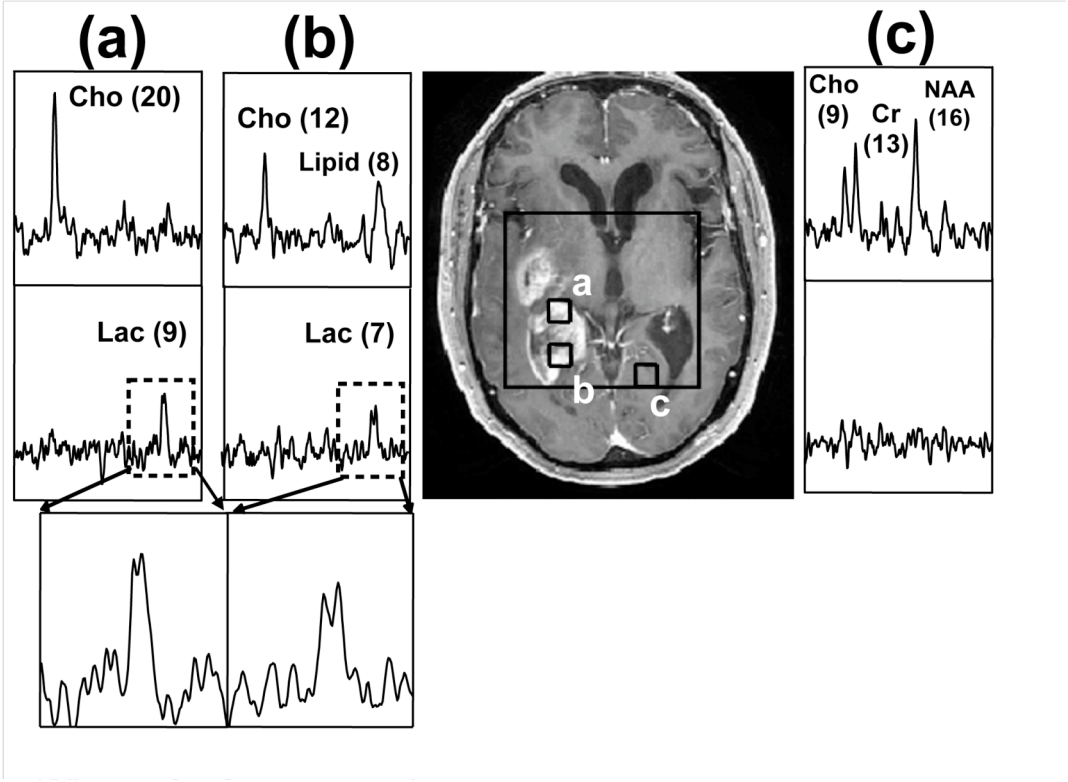

Figure 5.9 An example of lactate-edited spectra using the flyback-gradient method from a patient. The voxels in contrast enhancing lesions (a, b) contain high choline (Cho) as well as lipid in summed spectra (top) and lactate in subtracted spectra (bottom). The normal tissue from contra-lateral hemisphere (c) shows normal display of brain metabolite level (top in c) without lactate (bottom in c). The numbers indicate raw SNR values.

Seven patients showed the presence of lactate peaks and lactate with a SNR greater than 4 was observed in a total of fourteen examinations. The median normalized SNR of lactate in those patients was 17. The SNR of Cho, Cr and NAA in NAWM from all patients were similar to the values in NAWM from normal volunteers (not significantly different in a Mann-Whitney rank sum test with $p > 0.4$) (Table 5.3). The Cho/NAA in NAWM from the patients were similar to the values from healthy

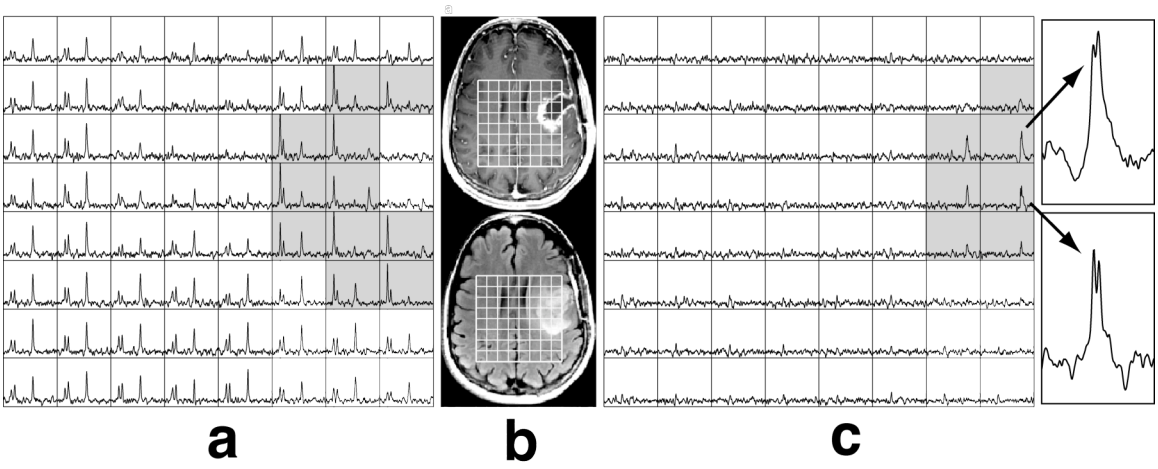

Figure 5.10 An example of lactate-edited spectra using the flyback-gradient method from a patient, showing the full coverage of a slice from the PRESS volume. In the summed spectra (a), the highlighted voxels show abnormal levels of metabolites with highly elevated choline around lesions in T1 post-contrast image (top, b) and T2-weighted FLAIR image (bottom, b). The highlighted voxels in the subtracted spectra (c) show lactate doublet at 1.3 ppm.

volunteers (not significantly different in a Mann-Whitney rank sum test with $p > 0.3$) and comparable to the values reported in several literatures (125,126). An example of data from a patient who had lactate in the CEL is shown in Figure 5.9. Voxel (a) and (b) were taken from the CEL in the T1-weighted post contrast image, and voxel (c) was taken from the normal tissue in the contra-lateral hemisphere. The voxels in the top row are summed spectra, and the voxels in the bottom row are subtracted spectra. High Cho levels were observed in the summed spectrum of the voxel (a) and (b), which is characteristic of tumor, and the presence of lipid in the summed spectrum of the voxel (b) may indicate necrosis. Lactate appeared in the voxels with lesions (a, b). Lactate doublets

were clearly visible as indicated in the zoomed-in spectra even with the presence of lipid. The voxel in the contra-lateral hemisphere contained normal levels of Cho, Cr and NAA (c) with no lactate in the corresponding subtracted spectrum.

Another example of a patient exam that was acquired with the lactate edited MRSI using a flyback echo-planar readout gradient is displayed in Figure 5.10. This shows the summed and subtracted spectra for the full coverage of a slice from the PRESS volume. The T2-weighted image from this patient (bottom in b) showed a large area of T2h in the left hemisphere, which consisted of a large necrotic area surrounded by a contrast enhancing rim, as depicted in T1-weighted post-contrast image (top in b). The summed spectra (a) showed abnormal levels of brain metabolites with high Cho and low NAA in the CEL and T2h. Several voxels in the necrotic area contained lipid. In the subtracted spectra (c), lactate doublet peaks were observed in the lesions.

5.4 Discussion

This study demonstrated the feasibility of detecting lactate, as well as Cho, Cr, NAA and lipid in 9.5 minutes using a new 3T lactate edited PRESS 3D MRSI sequence with a flyback echo-planar readout gradient. Using this approach we were able to detect lactate in patients with brain tumors (median normalized SNR=17) using a nominal voxel size of 1 cc and a factor of two reduction in scan time compared to conventional elliptical phase encoding MRSI (19 min).

Implementation of higher-bandwidth volume selection pulses was required because of the increased chemical shift between lactate methyl (1.3 ppm) and methine (4.1 ppm) resonances at higher field. It should be noted that the bandwidth of slice-

selective 180° pulses in the current study (1500 Hz) was higher than those reported in the previous studies (ranging from 874 to 1385 Hz) which used a PRESS scheme for volume-selection at 3T (111,117,127). The use of higher-bandwidth pulses was important in minimizing chemical shift mis-registration because the chemical shift artifact is inversely proportional to the size of the RF bandwidth used for localization. The use of an over-PRESS factor and high bandwidth VSS pulses further minimized artifacts from chemical shift mis-registration.

Over-PRESS factors of 1.2, 1.5 and 1.7 were tested in this study in order to minimize the chemical shift mis-registration of two lactate resonances as well as other metabolites. Although the higher factor would have given more uniform lactate signal and metabolite ratios, an over-PRESS factor of 1.5 was used for all volunteer and patient scans because of the proximity of the excited volume to the subject's skull and the potential of having increased contamination from subcutaneous lipid with an 1.7 over-PRESS factor.

Although, in theory, the chemical shift artifact should be eliminated with an 1.5 over-PRESS factor since the excited box (91x102 mm) is bigger than the prescribed box (80x80 mm) (Figure 5.3b), the lactate spectra with an 1.5 over-PRESS factor were still not completely uniform. Imperfections in slice-selection may have contributed to the artifact. The lactate signal in the left column was relatively smaller than those in the rest of the excited volume, however the variation of lactate level over the entire excited volume was relatively small and showed significant improvement over the lactate spectra acquired with the over-PRESS factor of 1.2 (Figure 5.5). The lactate SNRs in regions besides the left column were very uniform for the over-PRESS factor of 1.5 with the

standard deviation of 0.5 (Figure 5.4). When interpreting lactate peaks in the left column, one should note the possibility of underestimating lactate in this region and may use other means to correct for the chemical shift artifacts. This can either be achieved using theoretical corrections that are determined from the size of the PRESS selected volume, the over-PRESS factor and the bandwidths of the selection pulses or to acquire empirical data with similar parameters from a uniform phantom and use the ratio of lactate intensities in different voxels to provide correction factors.

The trade-off in using a flyback echo-planar readout gradient is a decrease in sensitivity. The median signal reduction for the flyback echo-planar readout gradient compared to the conventional phase encoding in the normalized SNR of NAA was 17% for phantom and 22 % for volunteers (Table 5.3), which are similar to previous findings described by Cunningham et al. (115). The loss of data during rewind portion of the flyback trajectory and imperfections in the gradient trajectory contributed to the net signal loss. Lactate peaks with SNR smaller than 4 were difficult to be distinguished from noise, and therefore the SNR of 4 was used as a threshold for calculating the median SNR of lactate in patients. Although the conventional phase encoding method may provide higher sensitivity for lactate detection, especially when lactate concentration in tumors is small, the long scan time (20 min) has traditionally prevented it from being used in routine clinical practices. By integrating the flyback echo-planar readout gradient, we have made possible a factor of two reduction in scan time (9.5 min). As the use of 3T scanner becomes more widespread due to its improved SNR associated with higher field strength, this technique is expected to be more appropriate for routine clinical uses and may assist in evaluating the role of lactate in the management of brain tumors.

In most cases, the highest lactate signal was observed in necrosis or resection cavity with a raw SNR as high as 18 in these regions. It is known that lactate produced in cancerous cells can accumulate in cystic or necrotic regions (128). Since lactate in these regions has been reported to be clinically irrelevant (105), we limited our estimation of lactate signal to CEL or T2h and excluded lactate in necrosis and resection cavity.
The current study was primarily aimed at demonstrating the practicability of detecting lactate signal using the new lactate-edited 3D MRSI sequence in patients with brain tumors at 3T; hence the clinical interpretation of lactate was omitted. A study assessing the patterns of lactate prior to radiation and during treatment in GBM patients is currently underway in an attempt to predict treatment outcome.

In conlucsion, we have developed and implemented a lactate edited 3D MRSI sequence that incorporates specialized rf pulses and a flyback echo-planar readout gradient at 3T. The results from the current work demonstrated the ability of this sequence to detect lactate in the presence of lipid signal from brain tumor patients in a clinically acceptable acquisition time of 9.5 min. While further studies are required, this robust technique should permit noninvasive measurement of brain lactate as well as Cho, Cr, NAA and lipid in routine clinical settings at 3T and may assist in investigating its potential as a marker for prognosis and response to therapy.

Chapter 6: Hyperpolarized ^{13}C MR Metabolic Imaging: Application to Brain Tumors

6.1 Introduction

It is well known that malignant transformation is associated with increased glycolytic flux and high cellular lactate excretion (65). Cancers preferentially reply on non-oxidative glycolysis for energy production, and excess lactate is produced as a result. With regard to brain tumors, a number of studies have shown increased lactate production in human gliomas (100,129), as well as in rat glioma models (130,131). These studies suggested that lactate may be used as a biomarker for anaerobic glycolysis and reduced cellular oxygenation, and that its detection may be important for assessing prognosis and detecting brain tumor response to therapy.

Proton MR Spectroscopy (^{1}H MRS) has been one of the major tools applied to non-invasive detection of lactate in brain tumors (108,109). Several studies have demonstrated the clinical significance of assessing lactate for the management of brain tumor patients using ^{1}H MRS. Sijens et al. (102) and Li et al. (103) showed the association of lactate and lipid signals in ^{1}H magnetic resonance spectroscopic imaging (MRSI) with the diagnosis of high grade tumor. Saraswathy et al. (104) demonstrated that elevated lactate and lipid signals were associated with poor survival in patients with glioblastoma multiforme (GBM) who were examined prior to radiation and chemotherapy. The interpretation of the lactate which is measured by ^{1}H MRS remains complex (128). The steady state lactate signal that is observed using this methodology

may stem from increased glycolysis in cancerous cells, but also depends on the rate of lactate production and clearance. A further complication is that the observed signal may originate from lactate that is accumulating in cystic or necrotic regions.

In an attempt to overcome these complications, ^{13}C MRS has been used to study in vivo tumor metabolism in brain tumor model of animals (130,132) and in patients with brain tumors (133). In these studies, tumor glycolytic metabolism was investigated using ^{13}C MRS after the injection of ^{13}C-labeled glucose. The altered energy metabolism in tumor was confirmed by the elevated production of ^{13}C-labeled lactate in tumor tissue. The intrinsically low concentration of ^{13}C cellular metabolites and the consequently low sensitivity compared to ^{1}H MRS limit the application of this technique in the clinic. Another approach is the use of positron emission tomography (PET) imaging with 2-[^{18}F]fluoro-2-deoxy-D-glucose (FDG), which has been established as a molecular imaging tool for monitoring uptake of FDG, which is an analogue of glucose (134,135). Despite its high sensitivity and appealing potential to assist in diagnosis and management of many cancers (136,137), the low specificity of this technique and the high levels of FDG uptake in normal grey matter have similarly limited its application in clinical neuro-oncology.

Dynamic Nuclear Polarization (DNP) and the recent development of a dissolution process which retains polarization into the liquid state enable the real time investigation of *in vivo* metabolism with more than 10,000-fold signal increase over conventional ^{13}C methods (6,138). Previous studies have demonstrated the promise of this technique for examining *in vivo* tumor metabolism for application in the management of cancer (59,62,139). Hyperpolarized ^{13}C pyruvate, labeled at the C1 position, may be used as a

substrate for evaluating metabolism by high-resolution ^{13}C MRSI, which can be integrated with anatomic proton magnetic resonance imaging (MRI). Chen et al. (139) showed elevated [1-^{13}C]-lactate in both primary and metastatic tumors in a transgenic adenocarcinoma of mouse prostate (TRAMP) model, while normal prostate tissue produced much less [1-^{13}C]-lactate. The result of this study demonstrated the potential for using hyperpolarized agents for evaluating tumor aggressiveness. Day et al. (59) demonstrated that the DNP technique can be use to detect tumor response to treatment in lymphoma-bearing mice *in vivo*. These studies were based on the premise that cancer cells preferentially generate lactic acid for cellular energy production and that pyruvate, which is an end product of glycolysis, is excessively converted to lactate via lactate dehydrogenase (LDH) in tumor tissues (65,140). The injection of ^{13}C pyruvate and assessment of ^{13}C lactate can be used to distinguish cancerous tissue from normal healthy tissue (62,141).

The purpose of the current study was to explore the feasibility of using ^{13}C MRSI with hyperpolarized [1-^{13}C]-pyruvate as a substrate for evaluation of *in vivo* tumor metabolism in a rat brain tumor model with a human glioblastoma xenograft, and compare it to normal rat brain. Two human GBM tissue-cultured cell lines were used to generate tumors in the rat brain for this study. These tumor models exhibited distinct heterogeneity in growth characteristics and histology, which simulated some of the characteristics of human GBM (142). In conducting this study, we characterized and compared ^{13}C imaging parameters with results from immunohistochemical analysis. To our knowledge, this is the first application of hyperpolarized ^{13}C agents to study brain tumor metabolism in an *in vivo* model system.

6.2 Materials and Methods

6.2.1 Cell Culture and Implantation of Intracerebral Tumors

The details of cell culture and intracerebral implantation procedure have been described elsewhere (142). In brief, U-251 MG and U-87 MG human GBM cell lines obtained from the Tissue Bank in the Department of Neurological Surgery at the University of California, San Francisco were maintained as exponentially growing monolayers in complete medium consisting of Eagle's minimal essential medium with 10% fetal calf serum and 1% nonessential amino acids. Cells were cultured at 37°C in a humidified atmosphere consisting of 95% air and 5% CO_2. Cells were harvested by trypsinization, washed once with Hanks' Balanced Salt Solution and resuspended in Hanks' Balanced Salt Solution for implantation. Five-week-old male athymic rats (rnu/rnu, homozygous) purchased from Harlan (Indianapolis, IN) were housed under aseptic conditions with filtered air and sterilized food, water, bedding, and cages. For implantation, rats were anesthetized with an intraperitoneal injection of ketamine (60 mg/kg) and xylazine (7.5 mg/kg). 10 μL of cell suspension (2×10^6 cells for U-251 MG and 5×10^6 cells for U-87 MG) were slowly injected into the right caudate-putamen of rat brain using an implantable guide-screw system. All protocols for animal studies were approved by the UCSF Institutional Animal Care and Use Committee.

6.2.2 Animal Preparation

Nine male athymic rats (median weight 270 grams) with human GBM xenograft tumors (four arising from U-251 MG cell lines and five from U-87 MG cell lines) and six

Table 6.1 Summary of the rats evaluated in this study.

Rat ID	Tumor cell type	Study date from tumor transplantation	Weight (g)	Pyruvate injection volume[b]	Polarization[b] (%)
Normal 1	N/A[a]	N/A	360	3.3	16.9
Normal 2	N/A	N/A	300	2.7	17.2
Normal 3	N/A	N/A	240	2.3	22.1
Normal 4	N/A	N/A	290	2.3	21.6
Normal 5	N/A	N/A	300	2.3	21.8
Normal 6	N/A	N/A	390	2.6	18.1
Tumor 1	U-251 MG	30	280	2.4	16.7
Tumor 2	U-251 MG	38	270	2.3	19.7
Tumor 3	U-251 MG	41	360	2.2	20.1
Tumor 4	U-251 MG	49	340	2.3	21.3
Tumor 5	U-87 MG	18	260	2.3	17.6
Tumor 6	U-87 MG	20	270	2.3	19.5
Tumor 7	U-87 MG	14	210	2.3	14.9
Tumor 8	U-87 MG	18	220	2.3	16.6
Tumor 9	U-87 MG	21	290	2.3	10.6

[a]N/A = not applicable.

[b]The listed injection volume and polarization are for 2D MRSI study.

normal male Sprague-Dawley rats (median weight 300 grams) were included in this study. Due to the difference in growth characteristics of the two cell lines (142), rats implanted with U-251 MG cell lines were scanned approximately 40 days and those implanted with U-87 MG cell lines were scanned 18 days after tumor implantation (Table 6.1). Before each imaging experiment, the rat was placed on a heated pad and anesthetized with isoflurane (2-3%). A catheter was placed into the tail vein for the intravenous administration of hyperpolarized pyruvate solution. The rat was transferred

to a heated pad positioned in the RF coil in the MR scanner. Anesthesia was continued with a constant delivery of isoflurane (1-2%) through a long tube to a cone placed over the rat's nose and mouth while the rat was in the scanner. The rat's vital signs (heart rat and oxygen saturation) were continuously monitored. The body temperature was maintained at 37°C throughout the imaging procedures by maintaining a flow of heated water through the pad underneath the rat.

6.2.3 Polarization Procedure

A detailed description of the polarization procedure and dissolution process was previously published (139,143). In brief, a mixture of 32 μL (approximately 40 mg) [1-^{13}C]-pyruvate (Isotec, Miamisburg, OH) and 15 mM OX63 trityl radical (Oxford Instruments, Abingdon, UK) was hyperpolarized using a HyperSense® DNP polarizer (Oxford Instruments, Abingdon, UK) in a field of 3.35T at approximately 1.4 °K by irradiation with 94.1 GHz microwaves similarly to the previous description (6). After approximately 60 minutes of microwave irradiation, the hyperpolarized pyruvic acid was rapidly dissolved in a saline solution with 5.96 g/L Tris (40 mM), 4.00 g/L NaOH (100 mM), and 0.1 mg/L Na_2EDTA to produce a 100 mM solution of pyruvate with a liquid state pH of 7.6. Approximately 2.3 mL of this solution was then injected into the tail vein of a rat within 10 s of removal from the polarizer. The injection lasted 12 seconds and was followed by a quick saline flush for both dynamic and spectroscopic imaging studies. Immediately after dissolution, an aliquot of the pyruvate solution was used to measure the liquid state polarization using an in-house-built low-field NMR spectrometer. Levels of

polarization ranged from 11-23 % (median polarization 18 %) (Table 6.1). The pH of the final solution was also measured (median pH 7.97±0.77).

6.2.4 ^{1}H and ^{13}C MR Imaging

Experiments were performed using a 3T GE Signa™ scanner (GE Healthcare, Milwaukee, WI) equipped with the multinuclear spectroscopy (MNS) hardware package. The RF coil used in these experiments was a dual-tuned ^{1}H-^{13}C coil with a quadrature ^{13}C channel and linear ^{1}H channel with a 8 cm inner coil diameter and 9 cm length constructed based on an earlier design (144).

High-resolution T_2-weighted anatomical images were obtained in all three planes using a fast spin-echo (FSE) sequence. Axial images were acquired in 8 minutes with an 8 cm FOV, 320 × 192 matrix, 2 mm slice thickness, and 5 NEX. Sagittal and coronal images were acquired in 6.5 minutes with an 8 cm FOV, 256 × 192 matrix, 2 mm (sagittal) or 1.5 mm (coronal) slice thickness, and 4 NEX.

Dynamic ^{13}C spectroscopic data were acquired from a 15 mm slice through the brain. Spectra were obtained every 3 seconds (TR = 3 seconds) for a period of 3.2 minutes using a double spin-echo pulse sequence consisting of a 5-degree flip angle RF excitation, 15 mm axial slice thickness, a pair of non-localized 180 degree hyperbolic secant refocusing pulses, TE = 35 ms, 5 kHz spectral bandwidth (BW), and 2048 spectral points (54,143). Data acquisition started simultaneously with the injection of hyperpolarized [1-^{13}C]-pyruvate and continued until a total of 64 spectra had been acquired in 192 s.

The ^{13}C 2D MRSI data were acquired using a double spin-echo pulse sequence

with a slice-selective variable small flip angle excitation pulse and a pair of non-localized 180 degree hyperbolic secant refocusing pulses (54). A 12 × 8 phase encoding matrix and 60 × 40 mm FOV on a 10 mm selected slice gave an in-plane resolution of 5 × 5 mm and 0.25 cm^3 voxel resolution, and was acquired in 11 seconds with TE/TR = 35/110 ms, 5 kHz BW, and 256 spectral points. Based on the changes in metabolite intensity seen from the ^{13}C dynamic data (Figure 6.1B), the MRSI acquisition began 20 seconds after the start of the injection. This was designed to obtain data while the hyperpolarized ^{13}C lactate was at a maximum. Centric k-space encoding and variable flip angle acquisition schemes were used to enable the efficient use of the hyperpolarized magnetization (145).

For the rats with tumors, pre- and post-Gadolinium (Gd) T_1-weighted axial anatomical images were obtained using a spin-echo sequence before and after the injection of 0.3 mL Gadolinium-DTPA (approximately 0.3 mmol/kg, diluted 1:2 with saline). These were acquired in 16 minutes with an 8 cm FOV, 320 × 192 matrix, 1.2 mm slice thickness, and 7 NEX.

6.2.5 Immunohistochemical Analysis

For immunohistochemical analysis, the rats with tumor were euthanized after the imaging experiment. Their brains were immediately removed and fixed by immersion in 10% buffered formalin. The fixed brains were then trimmed into multiple coronal sections and subsequently dehydrated by graded ethanols and embedded in wax (Paraplast Plus, McCormick Scientific) using routine techniques. All sections were cut at 5µm and mounted on *Superfrost/Plus* slides (Fisher Scientific). All coronal sections were examined by H&E staining. Antibodies to the following epitopes were obtained from

commercial sources and used at following dilutions and incubation times/temperatures: 1) carbonic anhydrase 9 (CA9) (#NB 100-417, Novis Biologicals, Littleton Colorado) at 1:500, 32 min/37°; and 2) Ki-67 (MIB-1)(anti-Ki-67[30-9], Ventana Medical Systems, Inc., Tucson, AZ) at 2μg/ml, 32 min/37° after pre-incubation in 3% H_2O_2/methanol for 16 min. Epitope retrieval for all antibodies was performed for 30 minutes in Tris buffer pH 8 at 90°. All immunohistochemistry was performed on the Ventana Medical Systems Benchmark XT using the iView (Avidin-Biotin) detection system with A-V blocking.

6.2.6 Data Processing

The hyperpolarized ^{13}C dynamic data were processed with MATLAB™ 7.0 (Mathworks Inc., Natick, MA). Individual FIDs were apodized with a 10 Hz Lorentzian filter in the time domain and Fourier-transformed to produce ^{13}C spectrum at each time point. Using the magnitude spectra, the peak height of lactate, alanine, and pyruvate were obtained and plotted as a function of time (Figure 6.1). The hyperpolarized ^{13}C 2D MRSI data were processed with software developed in our laboratory and that was described previously (89). The k-space FIDs were apodized by a 16 Hz Gaussian filter in the time domain and zero-filled to 512 points. The data were then Fourier-transformed to produce a 2-dimensional array of spectra from different spatial locations.

6.2.7 Data Analysis

In order to analyze ^{13}C metabolic parameters for each study, the signal-to-noise ratio (SNR) of lactate, pyruvate and total carbon (tC: a sum of lactate, pyruvate-hydrate, alanine, and pyruvate SNR), as well as the ratio of lactate over pyruvate (Lac/Pyr), lactate

over total carbon (lac/tC) and pyruvate over total carbon (Pyr/tC) were calculated from the ^{13}C 2D MRSI data using the magnitude spectra. In order to estimate the SNR, the integrals for lactate, pyruvate-hydrate, alanine and pyruvate were scaled by the standard deviation of the noise estimated from the first 100 points of the spectrum that contained no metabolite resonances. All SNR values were normalized according to polarization (%) and injection volume (mL) for each exam by:

$$\textit{Normalized SNR} = \textit{SNR} \times (18\ \% / \textit{polarization}) \times (2.3\ \textit{mL} / \textit{injection volume})$$

The carbon spectra were voxel-shifted in order to minimize partial volume effects (146) by applying linear phase to the k-space data as described by the Fourier shift theorem (147). To investigate differences in metabolism between rats with tumor and controls, each ^{13}C parameter was compared between the voxels containing Gd-enhanced brain tissue in the T_1-weighted post-Gd image of the rats with tumor and the normal brain tissue of control rats. Boxplots of each parameter were created and compared between the tumor and normal group. Images of each parameter were generated by spatially interpolating the normalized values of each parameter to the resolution of anatomical images using a linear kernel and overlaying it on the anatomical images. Each ^{13}C imaging parameter was compared between the rats with U-251 MG and U-87 MG model in order to investigate differences in metabolic imaging markers between the two types of tumor.

For immunohistochemical analysis, MIB-1 index (%), CA-9 index (%) and percent necrosis were compared between the rats with U-251 MG and U-87 MG model. For each tumor type, MIB-1 values were compared with ^{13}C imaging parameters in order to test for correlation between the degree of proliferation and ^{13}C metabolic imaging

markers. Mann-Whitney rank-sum test was used for all statistical comparisons, and Spearman rank correlation for the test of correlation.

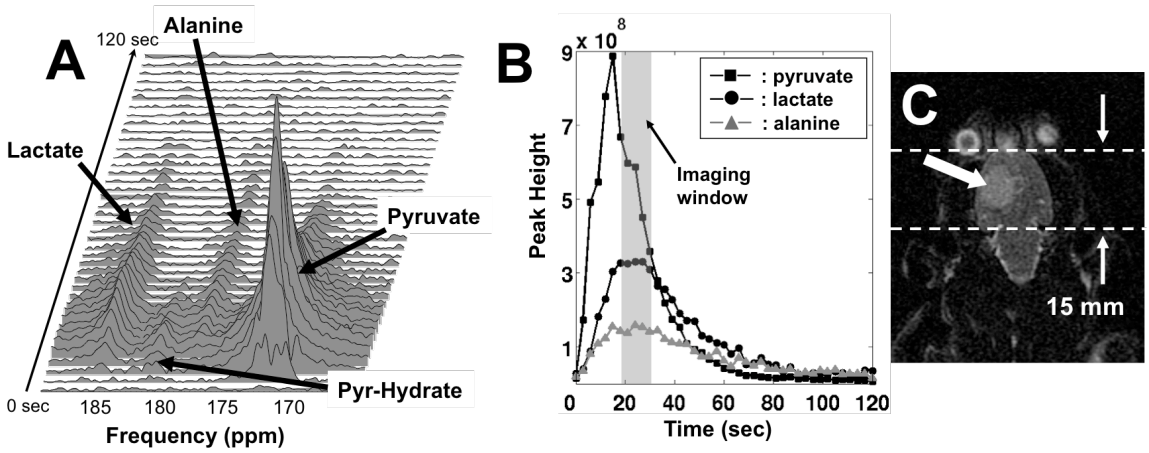

Figure 6.1 A representative example of hyperpolarized ^{13}C dynamic data from a rat with tumor (Tumor 6). The stack plot of ^{13}C magnitude spectra (A) and the peak height plots (B) show the time course of the hyperpolarized [1-^{13}C]-pyruvate and its metabolic products after the injection of 2.3 mL hyperpolarized pyruvate. Forty ^{13}C spectra were plotted in the stack plot (A), and the peak heights of pyruvate, lactate and alanine are plotted for 120 seconds after the injection (B). The pyruvate peak was scaled down by a factor of two for viewing purposes in (B). Both data show the hyperpolarized pyruvate quickly reaching its maximum approximately 15 seconds after the injection and its conversion to lactate and alanine. A T2 FSE image in the coronal plane (C) shows the hyperintense region inside the brain (arrow), which depicts the extent of tumor. The dashed line indicates the 15 mm slice thickness used for acquiring the ^{13}C dynamic data.

6.3 Results

The use of hyperpolarized [1-^{13}C]-pyruvate provided sufficient signal to detect its

transfer of the ^{13}C label to lactate and alanine. Figure 6.1A shows representative ^{13}C dynamic spectra from a 15 mm slice of rat brain with a tumor. Each horizontal line corresponds to a magnitude spectrum acquired at a time resolution of 3 seconds. From these spectra, the peak height of each metabolite was determined, with values plotted as a function of time in Figure 6.1B. Typically, the [1-^{13}C]-pyruvate signal (173 ppm) reached its maximum at approximately 15 seconds after the start of hyperpolarized pyruvate injection, and was followed by the [1-^{13}C]-lactate signal maximum (185 ppm) at approximately 20 seconds following pyruvate injection. After reaching its maximum, the lactate signal maintained a relatively constant level for 10 to 15 seconds. The pyruvate signal decreased rapidly from its maximum peak, and the lactate signal deceased at a slightly slower rate than the pyruvate. [1-^{13}C]-alanine and pyruvate-hydrate were also observed, but the signal levels were low. Figure 6.1C contains a T2 weighted coronal FSE image illustrating the slice coverage of the hyperpolarized ^{13}C dynamic data acquisition. As a result of these observations, the period of 20 to 35 seconds following injection was used as an imaging window for subsequent ^{13}C 2D MRSI studies.

The ^{13}C 2D MRSI data demonstrated excellent detection of ^{13}C-labeled lactate and pyruvate resonances in both the normal rats and the rats with tumor. The [1-^{13}C]-lactate resonance exhibited significantly higher SNR in the tumor brain tissue compared to the normal brain tissue. The [1-^{13}C]-pyruvate resonance was also observed to be higher in the tumor compared to the normal brain tissue. The pyruvate-hydrate and alanine signals appeared to be minimal in brain tissue.

Representative hyperpolarized ^{13}C 2D MRSI data of a normal rat are shown in Figure 6.2. The spectral array (Figure 6.2B) was overlaid on three axial T2 FSE images

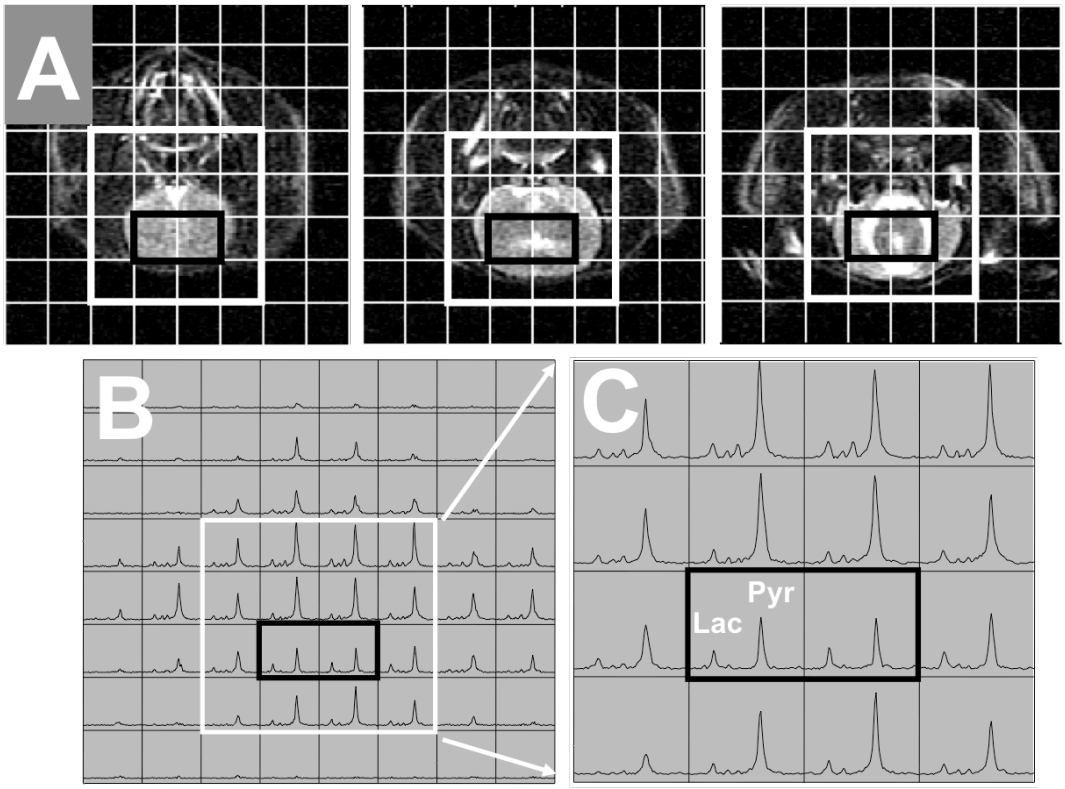

Figure 6.2 Representative hyperpolarized ^{13}C 2D MRSI data from a normal rat (Normal 4). The spectral arrays were overlaid on top of axial T2 FSE images at different locations within the ^{13}C MRSI slice (A). The corresponding magnitude spectra (B) and the zoomed-in spectra around the rat brain (C) showed hyperpolarized [1-^{13}C]-pyruvate and its conversion to other metabolites. The normal brain tissues (voxels inside the black box) displayed ample SNR of lactate and pyruvate. The pyruvate signal inside the brain was low compared to that in the other regions outside the brain, presumably due to the intact blood brain barrier.

within the MRSI slice (Figure 6.2A). Spectra around the brain are magnified in Figure 6.2C, with the black box highlighting voxels inside the brain. The pyruvate peak inside the brain showed an SNR of 99.7 (median, ranged from 71.1 to 119.3), but this was

considerably lower compared to the pyruvate peaks in the non-brain tissue around the brain, suggesting that the amount of pyruvate that passed through the blood brain barrier (BBB) was relatively low. The region outside the brain (voxels above the black box in Figure 6.2C) consistently exhibited a high level of pyruvate, which most likely originated from blood vessels, including the internal carotid artery and the vertebrobasilar arterial system that runs in the ventral surface of the brainstem. The lactate peak inside the brain was relatively small compared to the pyruvate peak (Figure 6.2C).

Figure 6.3 shows representative magnitude spectra from hyperpolarized ^{13}C 2D MRSI data and the corresponding anatomical images of rat brain with tumor. The spectral array had a 5 × 5 mm nominal in-plane resolution and 1 cm slice thickness (Figure 6.3B) and was overlaid on three axial T1 post-Gd images within the ^{13}C MRSI slice (Figure 6.3A). A contrast-enhancing lesion is seen in an axial T1 post-Gd image, and marks the boundary of tumor tissue whose BBB is disrupted. The white box in the T1 post-Gd images (Figure 6.3A) and the corresponding magnitude spectra (Figure 6.3B) represent zoomed-in regions around the rat brain. The voxels inside the brain are highlighted with a black box (Figure 6.3C). The two highlighted voxels in the left column of the black box are from the contrast-enhancing lesion of the rat brain, and exhibit a highly elevated lactate compared to the tissue in the contra-lateral hemisphere, other tissues around the brain and most importantly the brain tissue from normal rats (Figure 6.2C). The level of pyruvate was higher in the tumor region compared to brain tissue from the contra-lateral hemisphere and other tissues around the brain, and compared to the brain of rats without tumor. Axial T1 pre-Gd image and T2 FSE images in axial, coronal and sagittal planes are also shown in Figure 6.3D-G. The hyperintense region in the T2 FSE images

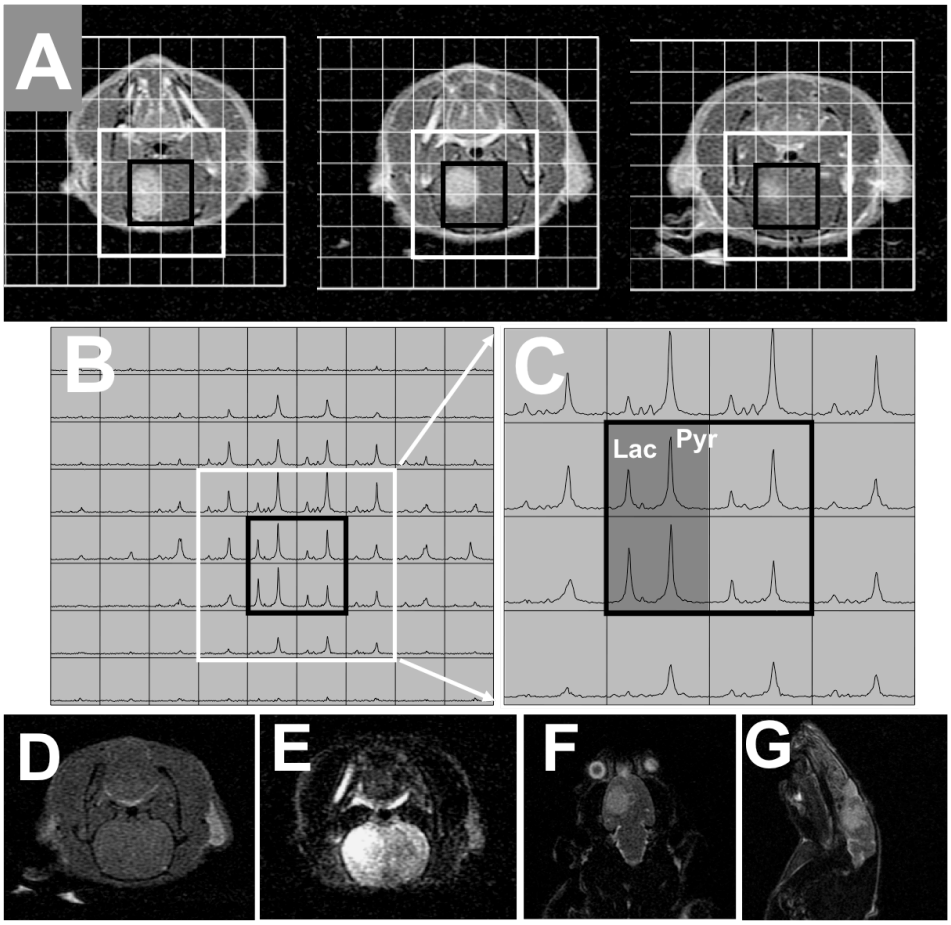

Figure 6.3 Representative anatomical images and the corresponding magnitude spectra from a hyperpolarized ^{13}C 2D MRSI study of a rat with tumor (Tumor 6). Axial T1 post-Gd images within the MRSI slice show contrast-enhancing lesion inside the brain (A). These 1.2 mm-thick axial images represent a fraction of volume that contributed to the ^{13}C signal acquired from a 10 mm slice. The white and black boxes represent the voxels around the brain and inside the brain, respectively. The corresponding magnitude spectra (B) and the zoomed-in spectra around the brain (C) clearly showed elevated ^{13}C lactate and pyruvate level in the tumor (highlighted voxels in the black box in C) compared to the brain tissue in the contra-lateral hemisphere and, most importantly, the brain tissue from the normal rats (Figure 6.2C). An axial T1 pre-Gd image (D) and T2 FSE images in axial, coronal and sagittal planes (E-G) are also shown.

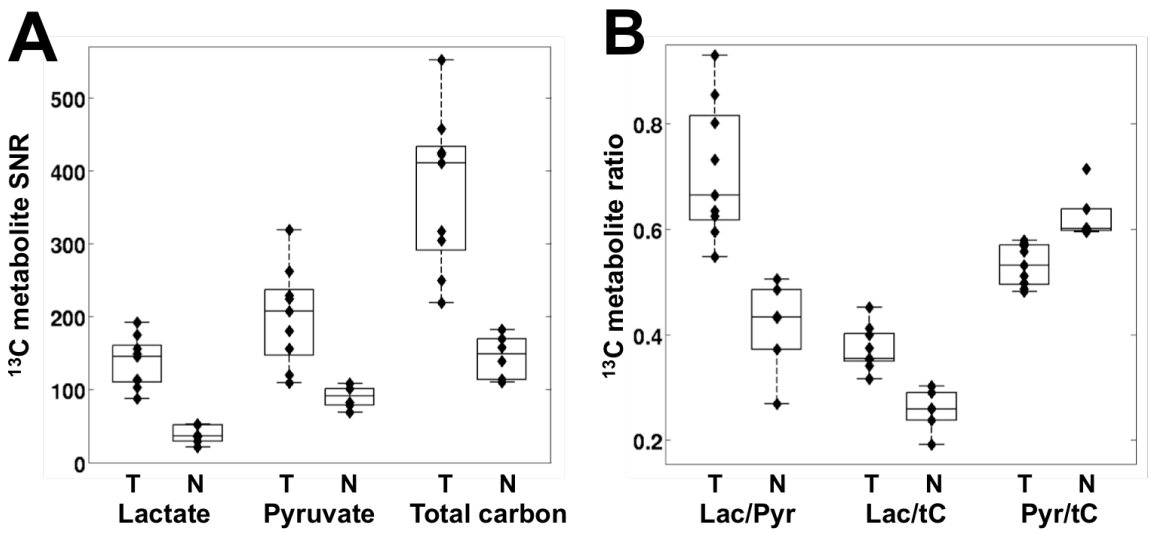

Figure 6.4 Comparison of the SNR of lactate, pyruvate and total carbon (A) and the ratio of lactate over pyruvate (Lac/Pyr), lactate over total carbon (Lac/tC) and pyruvate over total carbon (Pyr/tC) (B) between the tumor (T) and normal (N) rats. All ^{13}C parameters showed significant differences and clear separation between two groups ($p<0.0004$).

illustrates the extent of the tumor and corresponds to the location of the contrast-enhancing lesion in the T1 post-Gd images.

Quantification of the hyperpolarized ^{13}C 2D MRSI data is depicted in Figure 6.4. The SNR of lactate, pyruvate and total carbon as well as their relative ratios (Lac/Pyr, Lac/tC and Pyr/tC) demonstrated major differences in ^{13}C metabolic profiles between the rats with tumors and control rats. All six ^{13}C imaging parameters were significantly different between rats with and without tumor ($p<0.0004$). Representative maps of each ^{13}C parameter are shown for a rat with tumor and normal rat in Figure 6.5. The ^{13}C metabolite images were generated by interpolating the values of each parameter to the resolution of the axial T1 post-Gd image for the rat with tumor and the axial T1 pre-Gd image for the normal rat. The interpolated values from the rat with tumor and normal rat

were overlaid onto the corresponding anatomical images. The rat with a brain tumor showed high lactate, pyruvate, total carbon, Lac/Pyr and Lac/tC in the contrast-enhancing lesion, while the rat without a tumor had significantly lower levels of these parameters in its brain tissue. The contrast-enhanced brain tissue of the rat with a tumor exhibited lower Pyr/tC than the brain tissue of the normal rat.

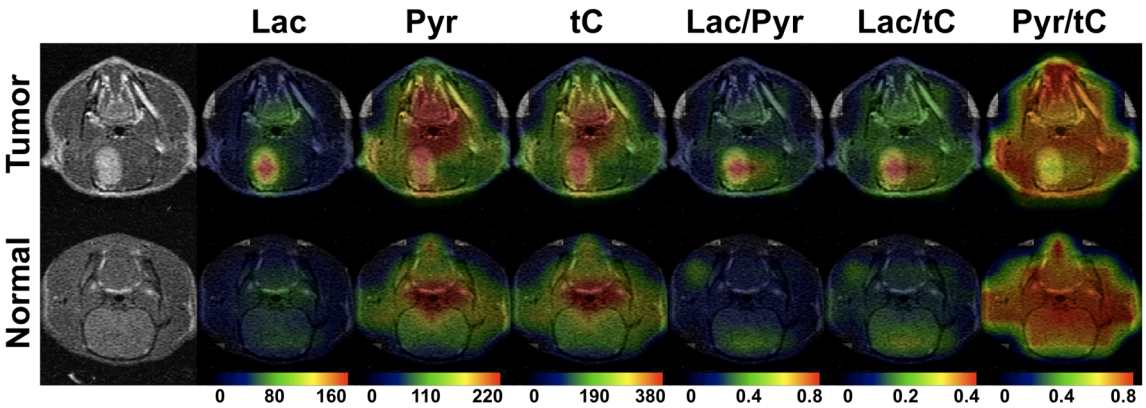

Figure 6.5 Metabolic maps of ^{13}C imaging parameters between a rat with tumor and a control rat. All six parameters exhibited considerably different intensity between the contrast-enhanced brain tissue of the rat with tumor and the brain tissue of the control rat.

Lac: lactate SNR, Pyr: pyruvate SNR, tC: total carbon SNR, Lac/Pyr: lactate over pyruvate ratio, Lac/tC: lactate over total carbon ratio, Pyr/tC: pyruvate over total carbon ratio.

In addition to the differences between the brains of rats with and without tumor (Figure 6.2-6.5), ^{13}C metabolic imaging parameters demonstrated distinctive characteristics between the brains of rats with U-251 MG and U-87 MG tumor (Figure

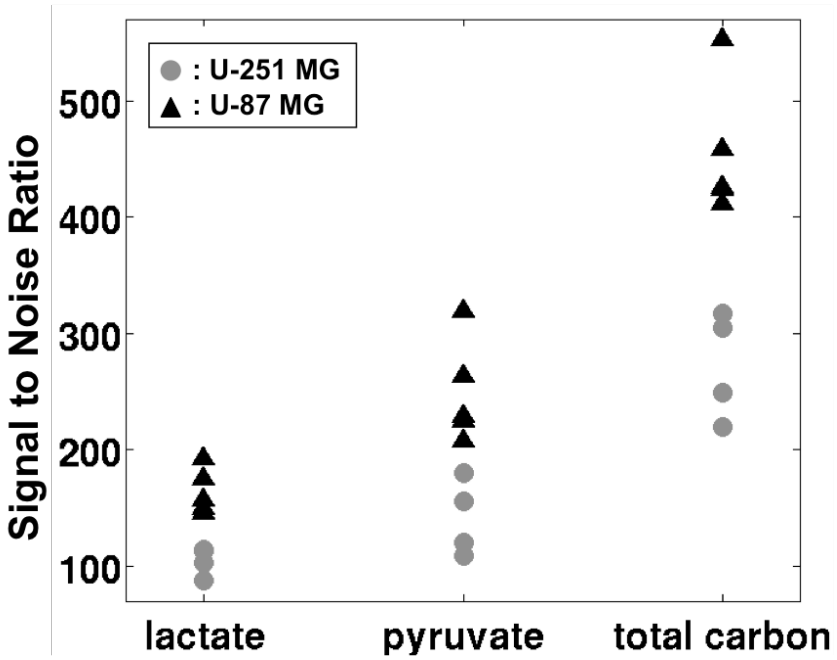

Figure 6.6 Comparison of the SNR of lactate, pyruvate and total carbon between U-251 MG and U-87 MG xenograft. All three parameters were significantly different between the two tumor types ($p<0.02$).

6.6). The U-87 MG tumors had significantly higher SNR of lactate, pyruvate and total carbon than U-251 MG tumors without any overlap of data ($p<0.02$).The two tumor lines had distinct histopathologic features. With H&E staining, all U-251 MG xenografts had greater than 25% necrosis on any section and this was present in a conspicuous pattern of scattered zones of geographic necrosis (Figure 6.7C). In contrast, H&E sections of the U-87 MG xenografts did not demonstrate any significant necrosis and were devoid of the zonal patterns of U-251 MG xenografts (Figure 6.7F). The results from immunohistochemical analysis (Table 6.2) also confirmed that there were distinctive patterns between the two tumor types. The CA-9 immunoreactive areas in sections of U-251 MG xenografts, as indicative of cellular hypoxia (148) were 10 – 25 percent for 3

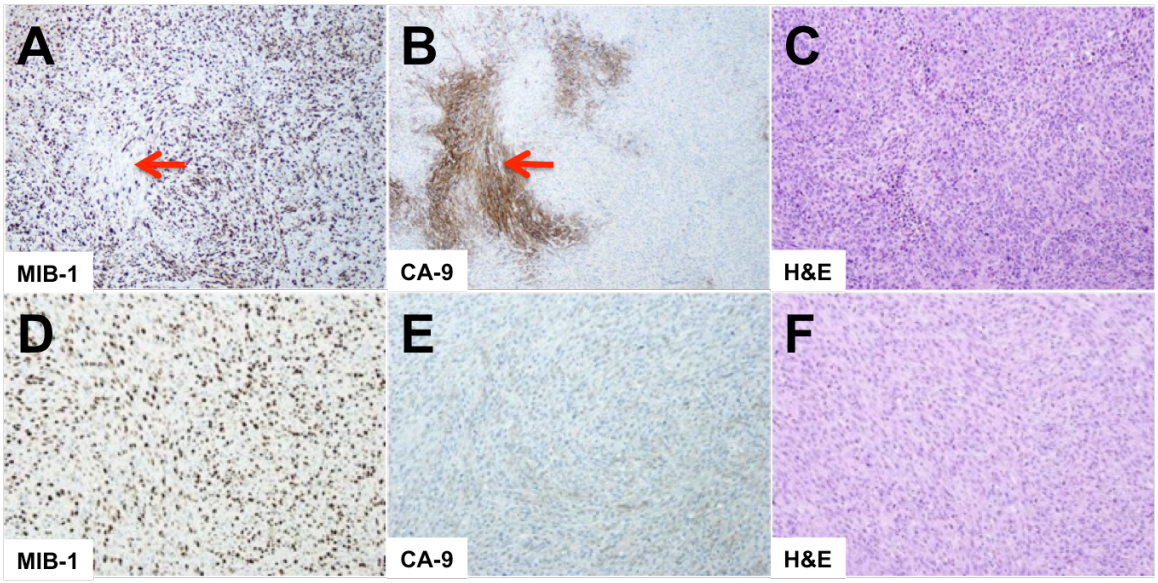

Figure 6.7 Staining of U-251 MG (A-C) and U-87 MG (D-F) xenograft with MIB-1 (A,D), CA-9 (B,E) and H&E (C,F). In the U-251 MG tissue, the zones of cellular hypoxia (arrow in B) corresponded to the zones of lower MIB-1 labeling (arrow in A). In contrast to U-251 MG, the U-87 MG xenografts did not exhibit zonal hypoxia or MIB-1 labeling, and there were no large zones of geographic necrosis. All images are at the same magnification.

rats and greater than 25 percent for the fourth. The cellular hypoxia in U-251 MG tumors was distributed in zones (arrow in Figure 6.7B) and these zones often corresponded to the zones of lower proliferation indicated in MIB-1 staining (arrow in Figure 6.7A). In contrast to U-251 xenografts, all of the U-87 xenografts had very low or no CA-9 labeling (Table 6.2), and did not exhibit zonal MIB-1 labeling (Figure 6.7D-E). The percentage of necrosis was significantly different between U-251 MG and U-87 MG tumor ($p<0.02$), and there was a strong trend toward difference ($p=0.06$) in the CA-9 index (%) between these two tumor types. There appeared to be strong correlations

Table 6.2 Immunohistochemical evaluation of the rats with intracranial human xenograft tumors.

Rat ID	Tumor model	MIB-1 (%)	CA-9 (%)	Necrosis (%)
Tumor 1	U-251 MG	45.65	10 – 25	≥ 25
Tumor 2	U-251 MG	57.00	10 – 25	≥ 25
Tumor 3	U-251 MG	39.47	10 – 25	≥ 25
Tumor 4	U-251 MG	48.11	≥ 25	≥ 25
Tumor 5	U-87 MG	39.78	0 – 10	none
Tumor 6	U-87 MG	43.65	0 – 10	none
Tumor 7	U-87 MG	48.52	none	0 – 10
Tumor 8	U-87 MG	37.32	0 – 10	none
Tumor 9	U-87 MG	40.04	10 – 25	none

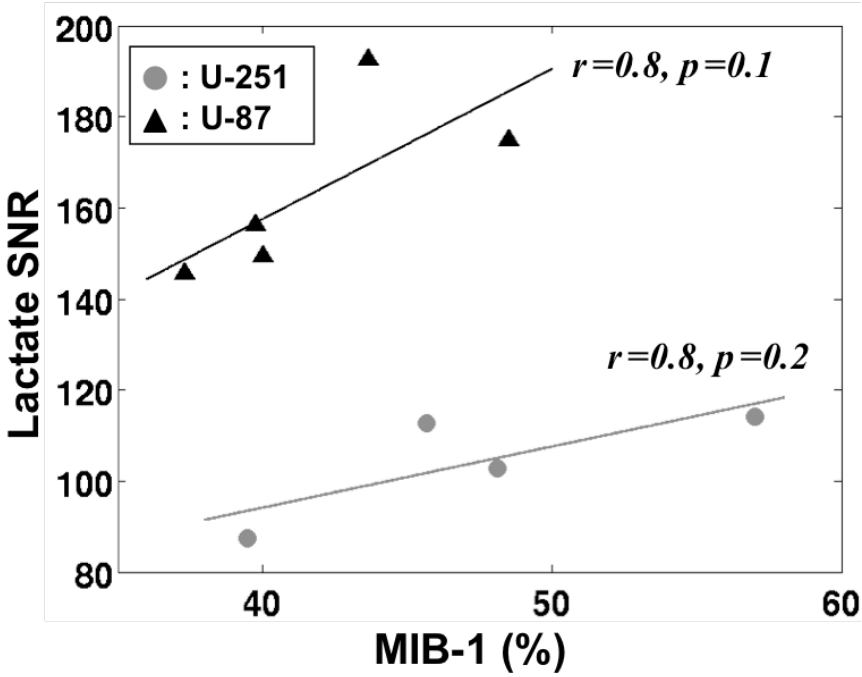

Figure 6.8 Correlation between proliferation marker (MIB-1) and the SNR of lactate. Both U-251 MG and U-87 MG tumor showed a strong correlation with MIB-1 index (r=0.08).

between MIB-1 index (%) and the SNR of lactate for each type of tumor (r=0.8) and the SNR of total carbon for U-87 MG tumor (r=0.7), but the statistical significant of this relationship was limited by the relatively small sample size (Figure 6.8).

6.4 Discussion

This study demonstrated the feasibility of detecting variations in the levels of pyruvate and lactate in human glioblastoma orthotopic xenografts using hyperpolarized [1-^{13}C]-pyruvate as a substrate. The hyperpolarized ^{13}C 2D MRSI data had a nominal spatial resolution of 0.25 cm^3 and demonstrated significant differences in ^{13}C metabolic profiles between tumor and normal brain tissue. The ^{13}C lactate and pyruvate levels in the contrast-enhancing lesion of the brain in rats with a tumor were much higher than those in the brain of rats without a tumor.

All six of the ^{13}C imaging parameters that were evaluated exhibited substantial differences between brains with and without tumors (Figure 6.4). The SNR of lactate, pyruvate and total carbon, and the ratio of Lac/Pyr, Lac/tC and Pyr/tC were well separated without any overlap of data between two groups ($p<0.0004$). The substantial differences between ^{13}C cellular metabolism measurements in tumor and normal brain suggest that this method has great potential for monitoring the abnormal metabolism in brain tumors.

Elevated levels of lactate, lactate to pyruvate ratios and lactate to total carbon ratios are consistent with the findings in previous studies that examined hyperpolarized ^{13}C-labeled lactate in TRAMP mice (62,139) and mouse lymphomas (59). These studies suggested that hyperpolarized ^{13}C-labled lactate may provide an indirect method for

assessing LDH activity. LDH is the enzyme catalyzing the conversion from pyruvate to lactate in glycolysis, which has been seen to have increased activity in brain tumors (149). A recent study demonstrated that the degree of upregulation correlated with the levels of hyperpolarized ^{13}C-labeled lactate in prostate cancer cell lines (150). Future studies will examine hyperpolarized ^{13}C metabolites in an ex vivo model of rat brain tumor and compare them with assay of LDH activity.

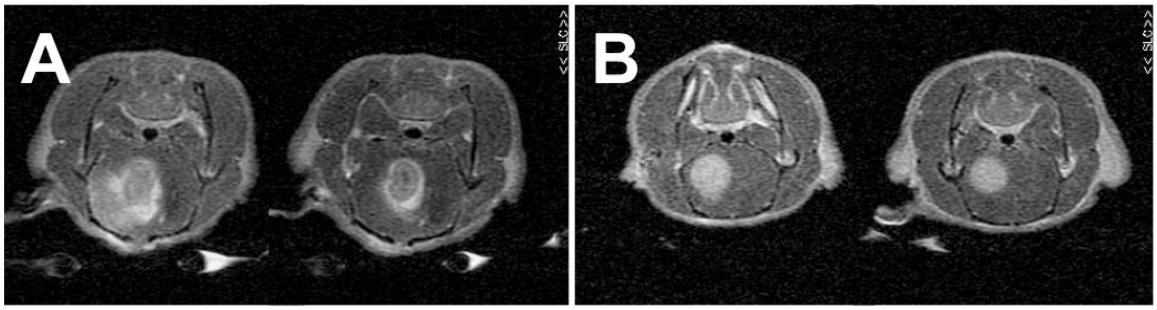

Figure 6.9 The patterns of contrast enhancement in T1 post-Gd images between rats with U-251 MG (A) and U-87 MG (B) model. The U-251 MG tumor displayed heterogeneous levels of contrast enhancement while the levels of contrast enhancement of the U-87 tumor was relatively constant with well-demarcated tumor margin. The difference in contrast-enhancing patterns may be indicative of inherent differences in molecular characteristics between these two tumor models.

U-251 MG and U-87 MG xenograft are well-established cell lines widely used for pre-clinical studies of brain tumor. Previous studies have shown that there are distinct differences in the histopathologic features of these two tumor types (142). U-251 MG tumors consist of a mixture of malignant spindle and epithelioid cells, and contain a large area of necrosis and an irregular border with adjacent brain tissue. U-87 MG tumors are

relatively well-circumscribed with malignant spindle cells in compact fascicles, and exhibit little or no necrosis. U-251 MG cells also contain more hypoxia than U-87 MG cells (151). The immunohistochemical data in our study were consistent with these findings (Table 6.2). The U-251 MG model exhibited large areas of necrosis and hypoxia, whereas the U-87 MG model showed little or no necrosis and hypoxia (Figure 6.7). The patterns of contrast enhancement in T1 post-Gd images of rats with U-251 MG and U-87 MG xenograft also indicated that there were marked differences between these two tumor types (Figure 6.9). The U-87 MG tumor had homogenous levels of contrast enhancement with a well-delineated tumor margin while the U-251 MG tumor exhibited varying levels of contrast enhancement with an irregular tumor margin.

The SNR of lactate, pyruvate and total carbon of U-87 MG tumor were significantly higher than those of U-251 MG tumor ($p<0.02$). The variation in these metabolic profiles may be due to, in part, higher necrotic fraction and thus relatively smaller number of viable tumor cells in U-251 MG compared to U-87 MG tumor. The higher pyruvate uptake in U-87 MG tumor is consistent with a previous study that showed higher mRNA expression in epithelial tumor cell lines of a monocarboxylate transporter (MCT2), which has a high affinity for the transport of pyruvate (152). In addition, low perfusion in necrotic areas of the tumors may result in inadequate delivery of pyruvate to tumor cells. Similarly, the SNR of total carbon, which can be considered as an estimate of the hyperpolarized compounds taken up by the tissue, was in agreement with the difference in necrotic fraction found between U-251 MG and U-87 MG tumors. The differences in ^{13}C metabolic imaging profiles between U-251 MG and U-87 MG model are consistent with the known differences in molecular characteristics between

these tumors and suggest that hyperpolarized ^{13}C MRSI that uses pyruvate as a substrate may be useful in characterizing tumor tissues. The different features of U-87 MG and U-251 MG tumor found from this study are summarized and compared with biological characteristics of the two tumor models in Table 6.3.

Table 6.3 Comparison of biological, immunohistochemical and MR features between U-251 MG and U-87 MG model.

Type of feature	U-251 MG	U-87 MG
Biological	A mixture of malignant spindle and epithelioid cells Irregular borders	Malignant cells in compact fascicles Well-circumscribed borders
Histological and Immunohistochemical	Larger area of necrosis and hypoxia	Little or no necrosis and hypoxia
MRI	Varying levels of contrast enhancement with an irregular tumor margin	Homogeneous levels of contrast enhancement with a well-delineated tumor margin
^{13}C MRSI	Relatively high SNR of lactate, pyruvate and total carbon	Relatively low SNR of lactate, pyruvate and total carbon

Uncontrolled proliferation is one of the major properties of cancer cell. In gliomas, a number of previous studies have correlated proliferation markers with clinical outcome and validated MIB-1/Ki-67 index as one of the major predictors of patient survival (153,154). The strong correlation between the MIB-1 index and the level of ^{13}C-labeled lactate that is converted from hyperpolarized ^{13}C-labeled pyruvate suggests that this methodology may provide an indirect method for characterizing tumor activity and a

potential surrogate marker for prognosis.

Although several imaging techniques such as ^{1}H MRSI, ^{13}C MRS or FDG PET have been applied to evaluate in vivo tumor metabolism (108,109,130-137), MR metabolic imaging using hyperpolarized ^{13}C substrates has several advantages. With the increase in sensitivity of these ^{13}C substrates, the detection of metabolites is possible at high spatial resolution (0.25 cm^3) in a very short acquisition time (11 seconds). These provide critical improvements over conventional ^{13}C MRS, which is limited by low sensitivity and prohibitively long acquisition time. Unlike ^{1}H MRSI, where the overlapping lipid peaks provide a technical challenge for quantifying lactate, the spectrum obtained using hyperpolarized ^{13}C metabolic imaging lack background signal. More importantly, while the interpretation of steady state ^{1}H lactate signal is complicated due to the various potential sources of ^{1}H lactate (128), the lactate signal using ^{13}C MRS reflects only the metabolically active lactate that is generated from hyperpolarized ^{13}C-labled pyruvate via LDH activity during the experiment. The high reproducibility in the difference in lactate uptake between the tumor and normal brain tissue suggests that this technique will be valuable in assessing prognosis and monitoring the brain tumor response to therapy.

Although the dynamic hyperpolarized ^{13}C data contains important biological information, the results of these studies were primarily used to determine the timing of subsequent 2D MRSI exams. They were limited by the 15 mm-thick slice which included contribution from brain, muscle, and the vasculature (Figure 6.1C). The application of a time-resolved MRSI method with an appropriate spatial resolution (139,155) may be expected to provide more specific information about the dynamics of tumor and normal

brain tissue. It should be noted that despite the presence of the blood brain barrier (BBB), the hyperpolarized ^{13}C 2D MRSI data provided ample SNR for evaluating lactate and pyruvate in both normal brain and in tumors (Figure 6.4). The high SNR means it may be possible to obtain increased coverage with higher spatial resolution in future experiments, and that the application of a fast acquisition technique incorporating a flyback echo-planar readout (54,139) could allow the acquisition of a 3D MRSI data which would cover the entire rat brain in a scan time of 10 to 17 seconds.

The brain tissue in normal rats demonstrated much lower pyruvate and lactate uptake compared to the malignant tumor tissue (Figure 6.2C and 6.3C). The low uptake of pyruvate in the normal brain tissue is thought to be due to the selective permeability of the BBB. It is known that lipid-soluble molecules readily penetrate the BBB while charged molecules, which are not lipid-soluble, cross the BBB slowly, or not at all (156). Since pyruvate is a negatively charged molecule in solution, the crossing of pyruvate molecule through the BBB is restricted. It is impossible to determine the degree of pyruvate signal contribution between the brain tissue and the blood vessels in this study because some of the pyruvate and lactate signal in the brain may come from the capillaries in the endothelial cells of the brain. However, the hyperpolarized lactate-to-pyruvate ratio in normal brain tissue was found to be notably different from one in the voxels located around blood vessels (Figure 6.2). In addition, the fact that the rats with U-87 MG and U-251 MG tumor exhibited dissimilar metabolic profiles (Figure 6.6) suggests that the pyruvate was delivered and metabolized in the tumor tissue and the conversion of pyruvate to lactate before its delivery to the tumor tissue was not the major source of the observed hyperpolarized signals. The results from this study suggest that

hyperpolarized ^{13}C MRSI is capable of discriminating between cancerous tissue and normal brain tissue.

In conclusion, this study demonstrated, for the first time, the feasibility of using the DNP to generate hyperpolarized [1-^{13}C]-pyruvate for evaluating the *in vivo* metabolism of an orthotopic human glioblastoma xenograft in rat brain. Distinct ^{13}C metabolic characteristics were observed in hyperpolarized ^{13}C MRSI data between the abnormal brain tissue of the rats with tumors and the normal brain tissue of rats without tumor. Moreover, the SNR of lactate, pyruvate and total carbon were observed to be different between U-251 MG and U-87 MG model, in a manner that was consistent with inherent differences found from immunohistochemical analysis. This study showed that tumor metabolism in brain tumor models can be examined using hyperpolarized ^{13}C MRSI and suggested that this technique may be useful in assessing prognosis and in monitoring brain tumor response to therapy in patients.

Chapter 7: Detection of Early Response to Temozolomide Treatment in Brain Tumors Using Hyperpolarized ^{13}C MR Metabolic Imaging

7.1 Introduction

The general course of treatment for patients with brain tumors consists of surgery, radiation therapy and chemotherapy with the goal of stopping tumor growth by impairing the reproductive process of cells or to kill tumor cells by inducing apoptosis. Temozolomide (TMZ) is one of the most frequently used chemotherapeutic drugs for treating brain tumors, especially high-grade gliomas. It is an alkylating agent and works by damaging DNA and thus triggering the death of tumor cells.

The current standard for monitoring brain tumor response to therapy is a combination of clinical symptoms and Macdonald criteria, which are based on the change in contrast enhancement from magnetic resonance imaging (MRI) or computed tomography (CT) scans (157). Advanced MR techniques such as ^{1}H magnetic resonance spectroscopy (MRS), perfusion MRI and diffusion weighted MRI have also been used for monitoring brain tumor response to therapy (158-163), but may take several weeks to detect response to therapy. Early detection of brain tumor response to treatment would be valuable in defining criteria for continuing or modifying treatment strategies.

Positron emission tomography (PET) is an imaging modality that has been widely used in the clinic for predicting treatment effects. Although the ability to detect an altered

^{18}F-fluoro-dexoyglucose (FDG) uptake in cancerous tissue has made this technique useful in some areas of oncology (134), its use in neuro-oncology presents unique challenges due to the high background signal from normal gray matter (164).

Dynamic nuclear polarization (DNP) and the recent development of a dissolution process that retains polarization in liquid state have allowed for the acquisition of ^{13}C MRS data with more than 10,000-fold increase in sensitivity. Pre-clinical ^{13}C MRS of hyperpolarized [1-^{13}C]-pyruvate has been applied to the investigation of *in vivo* metabolism in subcutaneous lymphoma (59), prostate cancer (62,63), cardiac ischemia (67) and liver cancer (165). A recent study has demonstrated that this technique can be used for differentiating brain tumors from normal tissue in animal model of brain cancer (166). The purpose of this study was to demonstrate the feasibility of using DNP-hyperpolarized [1-^{13}C]-pyruvate to measure response to chemotherapy using TMZ in an orthotopic human glioblastoma xenograft model. Our emphasis was to establish the time frame of changes in ^{13}C imaging parameters and to compare the results with alterations in tumor volume over time.

7.2 Materials and Methods

7.2.1 Cell Culture

U-87 MG human glioblastoma multiforme (GBM) cell lines obtained from the Tissue Bank in the Department of Neurological Surgery at the University of California, San Francisco (UCSF) were maintained as exponentially growing monolayers in complete medium consisting of Eagle's minimal essential medium with 10% fetal calf serum and 1% nonessential amino acids. Cells were cultured at 37°C in a humidified

atmosphere consisting of 95% air and 5% CO_2. Cells were harvested by trypsinization, washed once with Hanks' Balanced Salt Solution and resuspended in Hanks' Balanced Salt Solution for implantation.

7.2.2 Intracerebral Tumor Implantation

The details of intracerebral implantation procedure have been described elsewhere (142,166). In brief, seven-week-old male athymic rats (rnu/rnu, homozygous) purchased from Harlan (Indianapolis, IN) were housed under aseptic conditions with filtered air and sterilized food, water, bedding, and cages. For implantation, rats were anesthetized with an intraperitoneal injection of ketamine (60 mg/kg) and xylazine (7.5 mg/kg). 10 μL of cell suspension (5×10^6 cells) were slowly injected into the right caudate-putamen of rat brain using an implantable guide-screw system. All protocols for animal studies were approved by the UCSF Institutional Animal Care and Use Committee.

7.2.3 Animal Population and Imaging Study Scheme

Twenty male athymic rats (median weight 267 grams) with human GBM xenograft tumors (U-87 MG cell lines) were included in this study. Rats were randomly assigned to TMZ treatment (Temodar®, Schering corp., Kenilworth, NJ) or vehicle control (Ora-Plus®, Paddock Laboratories, Inc., North Minneapolis, MN) groups. All rats received treatment at the 9th to 15th day from the tumor implantation when the size of the tumor monitored by T_2-weighted axial images was at least half the size of a cerebral hemisphere (Table 7.1). The TMZ treated group (n=10) received a single dose of 100 mg/kg TMZ by oral gavage while the control group (n=10) received 1 mL of vehicle

only. All animals underwent ^{13}C and ^{1}H imaging study before the treatment (D0), at D1 (days from treatment) and/or D2 and at several subsequent time points. The D0 scan served as a baseline. Five treated and five control rats were sacrificed at D2 and the tumor tissue from their brains analyzed. Two treated and five control rats were monitored until they exhibited neurologic symptoms indicative of deteriorating body condition and were then euthanized. Three treated rats were sacrificed between D7 and D16. Table 7.1 shows a summary of the animals included in this study, the timing of their imaging studies, and the end point for each animal.

7.2.4 Polarization Procedure

A mixture of 32 μL (approximately 40 mg) [1-^{13}C]-pyruvate (Isotec, Miamisburg, OH) and 15 mM OX63 trityl radical, along with 0.5 mM (approximately 0.47 μL) of Prohance gadolinium for polarization enhancement (167), was hyperpolarized using a HyperSense® DNP polarizer (Oxford Instruments, Abingdon, UK) in a field of 3.35T at approximately 1.4 °K by irradiation with 94.1 GHz microwaves using methods described previously (6). After approximately 60 minutes of microwave irradiation, the hyperpolarized pyruvic acid was rapidly dissolved in a saline solution with 5.96 g/L Tris (40 mM), 4.00 g/L NaOH (100 mM), and 0.1 mg/L Na_2EDTA (ethylenediaminetetraacetic acid). The final dissolved solution had a concentration of 100 mM, pH ~7.5 and a polarization of ~25%. The degree of polarization was measured by taking a small aliquot and injecting it into a custom-built polarimeter ~15 sec after dissolution. Approximately 2.8 mL of this solution was then injected into the tail vein of a rat within 10 s of removal from the polarizer. Taking into account the volume of the

catheter, which is 0.3 mL, approximately 2.5 mL of the dissolved solution was delivered to the animals. The injection lasted 10 seconds.

Table 7.1 Summary of rats included in this study.

Rat ID	Group	Tx date from tumor implantation (days)	Weight at Tx (g)	D1 scan (Y/N)	D2 scan (Y/N)	Study end point (days from Tx)
T1	Treated	14	220	Y	N	D38
T2	Treated	15	290	Y	Y	D34
T3	Treated	10	260	Y	Y	D7
T4	Treated	10	270	Y	N	D14
T5	Treated	10	300	Y	Y	D2
T6	Treated	12	240	Y	Y	D16
T7	Treated	13	310	Y	Y	D2
T8	Treated	15	280	Y	Y	D2
T9	Treated	14	300	Y	Y	D2
T10	Treated	10	250	N	Y	D2
C1	Control	14	200	N	Y	D8
C2	Control	10	270	Y	N	D6
C3	Control	12	270	Y	Y	D2
C4	Control	11	230	Y	Y	D2
C5	Control	13	260	Y	Y	D2
C6	Control	12	280	Y	Y	D2
C7	Control	9	290	Y	Y	D5
C8	Control	10	320	Y	Y	D5
C9	Control	9	250	N	Y	D6
C10	Control	13	250	N	Y	D2

Tx: treatment; Y: yes; N: no.

7.2.5 ^{1}H and ^{13}C MR Imaging

Experiments were performed using a 3T GE Signa™ scanner (GE Healthcare,

Milwaukee, WI) equipped with the multinuclear spectroscopy (MNS) hardware package. The RF coil used in these experiments was a dual-tuned ^{1}H-^{13}C coil with a quadrature ^{13}C channel and linear ^{1}H channel that had a 8 cm inner coil diameter and 9 cm length constructed based on an earlier design (144).

Before each imaging experiment, the rat was placed on a heated pad and anesthetized with isoflurane (2-3%). A catheter was placed into the tail vein for the intravenous administration of hyperpolarized pyruvate solution. The rat was transferred to a heated pad positioned in the RF coil in the MR scanner. Anesthesia was continued with a constant delivery of isoflurane (1-2%) through a long tube to a cone placed over the rat's nose and mouth while the rat was in the scanner. The body temperature was maintained at 37°C throughout the imaging procedures by maintaining a flow of heated water through the pad underneath the rat.

Prior to each ^{13}C imaging, high-resolution T_2-weighted anatomical images were obtained in the axial plane using a fast spin-echo (FSE) sequence. These axial images were acquired in 13 minutes with an 8 cm FOV, 192 × 192 matrix, 2 mm slice thickness, and 8 NEX (TE/TR=60/4000 ms). The ^{13}C 3D magnetic resonance spectroscopic imaging (MRSI) data were acquired using a double spin-echo sequence, which has been described in detail previously (54). In brief, the sequence consists of a slice-selective variable small flip angle excitation pulse and a pair of non-localized 180° hyperbolic secant refocusing pulses. A 10 × 8 × 1 phase encoding matrix with flyback readout on the z-axis (10 × 8 × 16 effective matrix) with 40 mm × 32 mm × 86.4 mm FOV rendered a 4 mm × 4 mm × 5.4 mm spatial resolution (0.086 cm^3 voxel resolution). The data were acquired in 17 seconds with TE/TR = 140/215 ms, 581 Hz spectral bandwidth and 59 spectral points.

The MRSI acquisition began 20 seconds after the start of the injection of hyperpolarized ^{13}C-pyruvate in order to obtain data while the hyperpolarized ^{13}C-lactate was at a maximum (166). Centric k-space encoding and variable flip angle acquisition schemes were used to enable the efficient use of the hyperpolarized magnetization (145).

Anatomical images were obtained using an axial T1-weighted spin-echo sequence after the injection of 0.1 mL Gadolinium (Gd)-DTPA (approximately 0.2 mmol/kg, diluted 1:2 with saline). These were acquired in 13.5 minutes with an 8 cm FOV, 320 × 192 matrix, 1.2 mm slice thickness, and 6 NEX (TE/TR=10/700 ms).

7.2.6 Data Analysis

The method for processing ^{13}C MRSI data has been described previously (139). All ^{13}C MRSI data were analyzed with software developed in our laboratory (89). The raw readout data were reordered into a 4D array. Only the k-space data from flat parts of the flyback trajectory were selected. The time domain signal was apodized by a 16-Hz Gaussian filter and zero-filled to 256 points. A 4D Fourier transform was used to produce a 3D spatial array of spectra. An additional linear phase correction was applied in the flyback dimension to correct for the offset of individual k-space points (115).

The ratio of lactate over pyruvate (Lac/Pyr) was estimated from the ^{13}C magnitude spectra in order to assess an early treatment response. Lac/Pyr was calculated from a voxel containing Gd-enhanced brain tissue in the T1-weighted post-Gd image of the rat brains. The carbon spectra were voxel-shifted in order to minimize partial volume effects by applying linear phase to the k-space data as described by the Fourier shift

theorem (147). In order to estimate the variation of ^{13}C metabolism over time, a percent Lac/Pyr change from baseline was calculate using the following formula:

$$\% \text{ Lac/Pyr change from baseline} = \frac{(Lac/Pyr)_{Di} - (Lac/Pyr)_{D0}}{(Lac/Pyr)_{D0}} \times 100 \qquad [7.1]$$

where $(Lac/Pyr)_{Di}$ and $(Lac/Pyr)_{D0}$ are Lac/Pyr at a certain time point *i* and at baseline, respectively. The percent change in Lac/Pyr from baseline at D1 and D2 were compared between the rats in the treated and control groups using Mann-Whitney rank-sum test.

In order to estimate tumor volume, the 3D volume of the contrast enhancing lesion was calculated from the axial T1 post-Gd slices using software developed in our laboratory (89). At each time point, a percent tumor volume change from baseline was calculated using the same method as the Eq. [7.1].

7.3 Results

For the treated group, the tumor metabolism as measured by the ^{13}C metabolic ratio was altered as early as one day after TMZ treatment (Figure 7.1). At baseline, both the treated and control rats exhibited elevated level of Lac/Pyr with mean Lac/Pyr of 1.1 (SD=0.5). For the group treated with TMZ, Lac/Pyr showed a mean 21 % reduction at D1 (SD=22) and a mean 34 % reduction at D2 (SD=16) compared to baseline values (Figure 7.1). In contrast, Lac/Pyr of the control rats was continuously elevated following administration of vehicle, showing a mean 20 % (SD=25) and 10 % (SD=36) increase compared to baseline values at D1 and D2, respectively (Figure 7.1). Lac/Pyr was statistically different between the treated (n=9) and control (n=7) groups at D1 ($p<0.008$). This pattern continued at D2 ($p<0.008$) between the two groups (n=7 for treated rats and n=9 for control rats). Lac/Pyr for the control group was progressively

elevated over time, while levels of Lac/Pyr stabilized for the treated group after D5 (Figure 7.1).

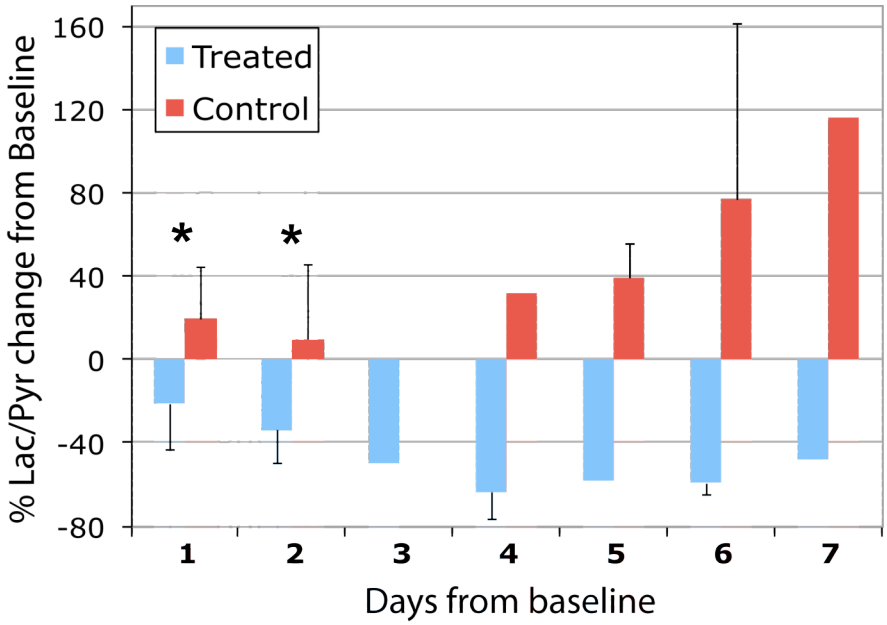

Figure 7.1 Percent change in Lac/Pyr from baseline for the treated and control groups. The ^{13}C metabolism measured by this parameter showed a significant difference between the two groups at D1 and D2 (*$p<0.008$).

Contrary to the findings from ^{13}C MRSI data, both the treated and control rats showed a similar increase in tumor volume for the first few time points (Figure 7.2). The treated group showed a mean 37 % (SD=13) and 68 % (SD=23) increase in their tumor volume at D1 and D2 while the control group showed a mean increase of 28 % (SD=15) and 56 % (SD=19) at D1 and D2. There were no significant differences in the change of tumor volume between the two groups either at D1 ($p>0.1$) or at D2 ($p>0.2$). The volume of tumor in the treated rats showed a steady increase in the first two days and then started to decrease at approximately the 5th day after the initiation of treatment. In contrast, the

tumor volume of the control rats continued to increase (Figure 7.2).

Figure 7.3 and 7.4 are examples from a treated and a control rat, depicting the morphological and metabolic changes that occurred shortly after treatment. T1 post-Gd images, ^{13}C spectra and Lac/Pyr overlay map from D0, D1 and D2 scans are displayed. Lac/Pyr overlay maps were generated by spatially interpolating Lac/Pyr values to the resolution of anatomical images using a linear kernel and overlaying it on the anatomical images. In both examples, the tumor volume continues to increase over time. The lactate peak in the orange voxel, which contained the region of tumors, decreased shortly after the treatment for the treated rat, while the pyruvate peak remained almost constant (Figure 7.3). In contrast, the lactate peak of the control rat showed a relative increase after receiving vehicle (Figure 7.4) and Lac/Pyr progressively increased. The Lac/Pyr maps reiterated these findings for both groups.

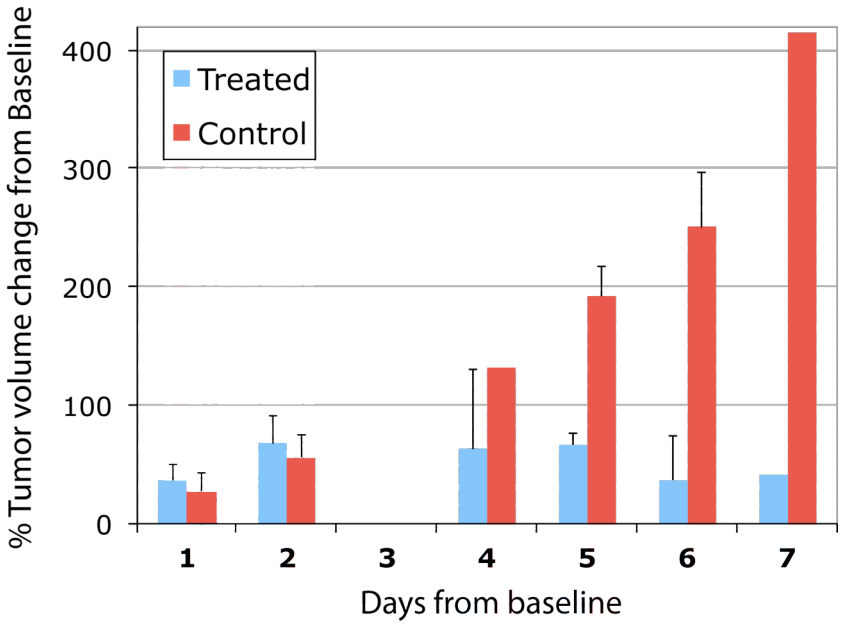

Figure 7.2 Percent tumor volume change from baseline for the treated and control groups. Both groups showed an increase in their tumor volume at D1 and D2.

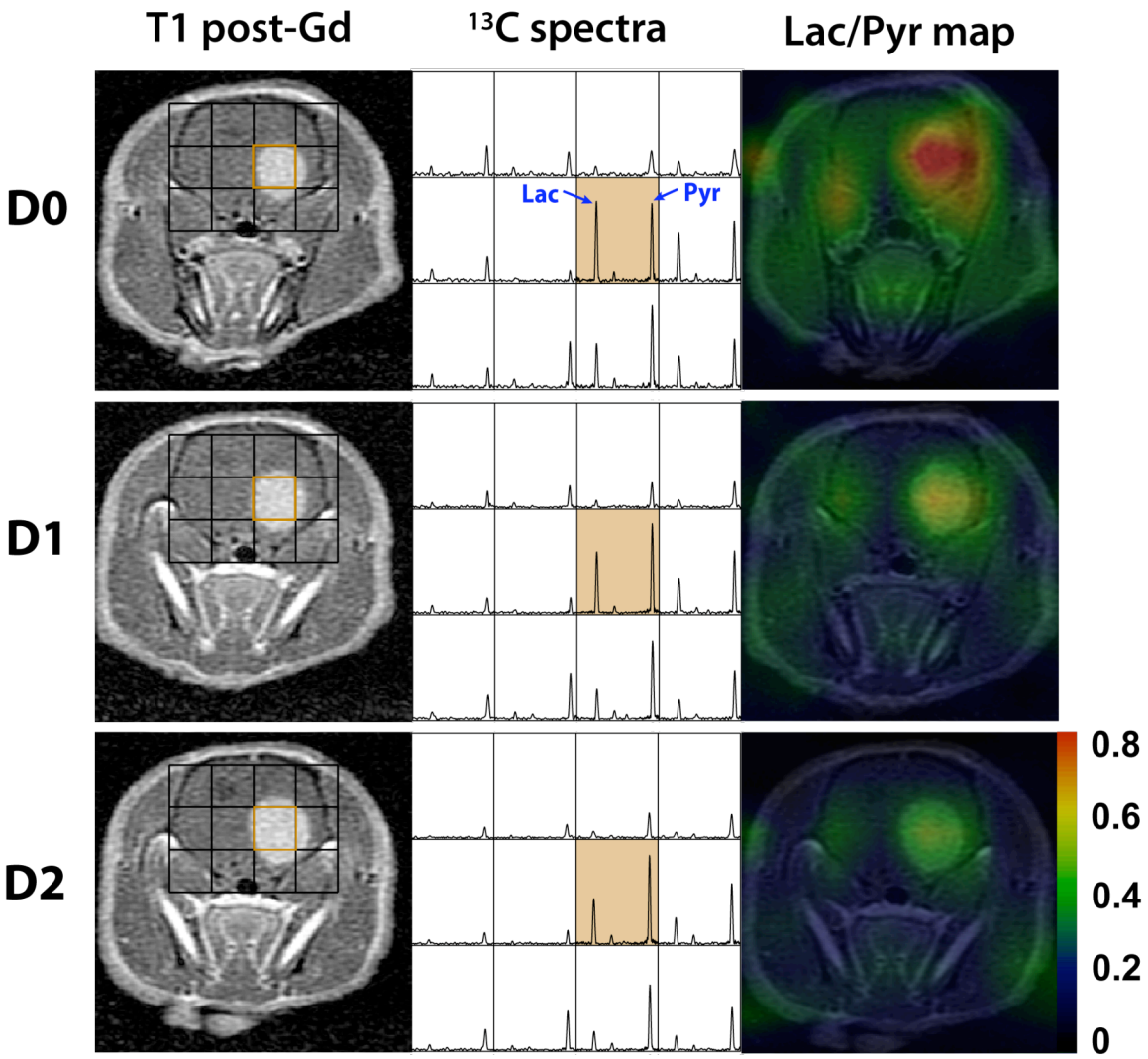

Figure 7.3 An example of a treated rat, showing its T1 post-Gd images, ^{13}C spectra and Lac/Pyr overlay map at D0 (pre-treatment), D1 (one day after the initiation of treatment) and D2 scan. The lactate peak decreased shortly after the treatment, resulting in a drastic drop in Lac/Pyr.

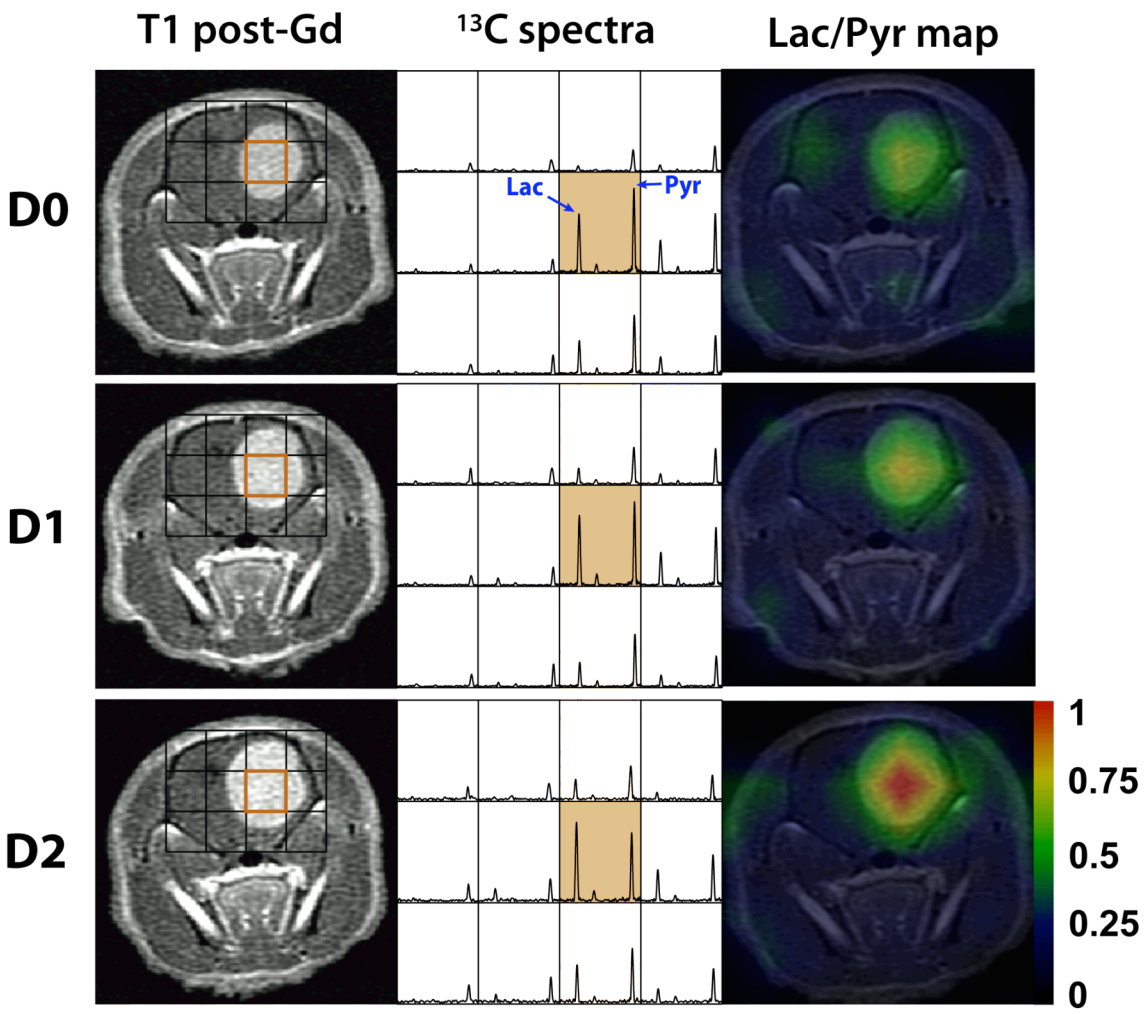

Figure 7.4 An example of a control rat, showing its T1 post-Gd images, ^{13}C spectra and Lac/Pyr overlay map at D0 (pre-treatment), D1 (one day after the treatment initiation) and D2 scan. The lactate peak continued to increase relatively to the pyruvate peak after the treatment, resulting in a steep increase in Lac/Pyr.

The results from the immunohistochemical analysis of tumor tissue showed different levels of caspase-3 staining between the two groups (Figure 7.5). Caspase-3 is an indicator of cell apoptosis. Figure 7.5a is a caspase-3 stained slice from a control rat (C3) that was sacrificed at D2. The absence of stained cells indicates that there were no

apoptotic cells in the tissue at this time. In contrast, the caspase-3 stained slice from a treated rat (T9) sacrificed at D2 showed a small number of apoptotic cells (Figure 7.5b). There were a large number of stained cells for the slice from a treated rat (T3) that was sacrificed at D7, indicating that a greater degree of apoptosis had been induced by DNA alkylation (Figure 7.5c).

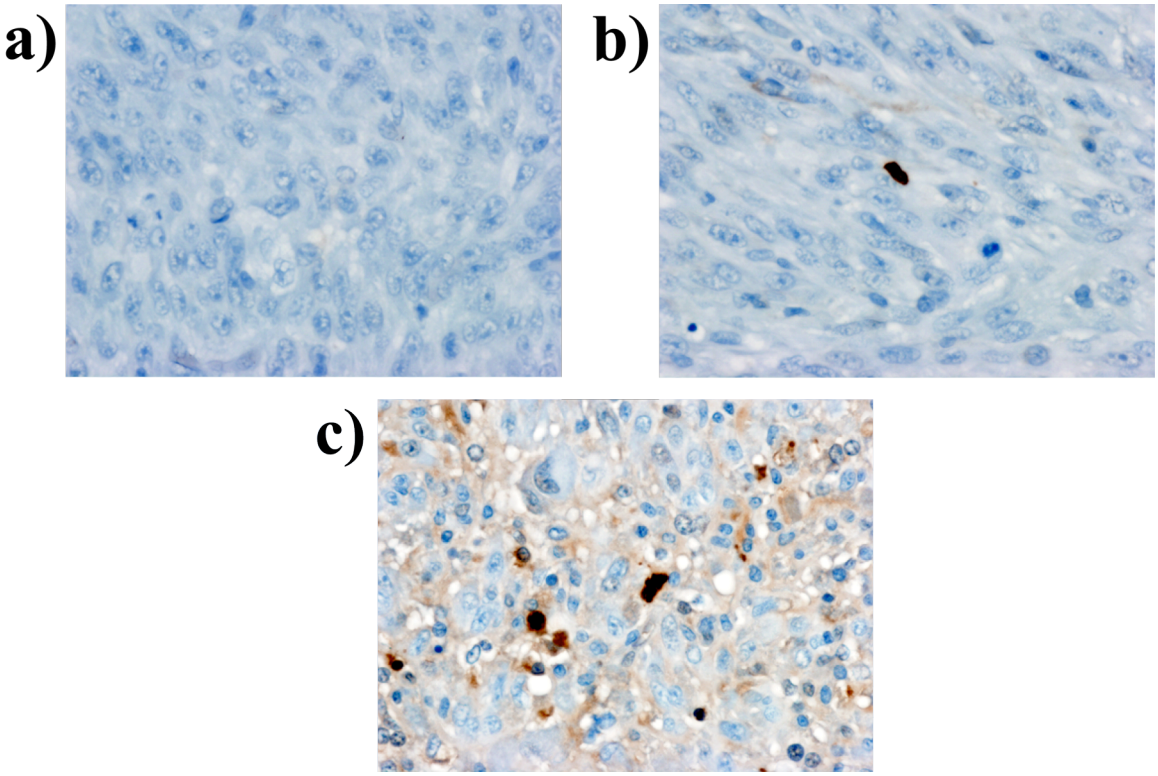

Figure 7.5 Immunohistochemical staining of caspase-3 for a control rat sacrificed at D2 (a), a treated rat sacrificed at D2 (b) and a treated rat sacrificed at D7 (c). All images are at the same magnification (40x).

7.4 Discussion

This study demonstrated the feasibility of detecting early response to TMZ treatment in human glioblastoma orthotopic xenografts using hyperpolarized ^{13}C MRSI with [1-^{13}C]-pyruvate as a substrate. The ^{13}C data from the treated rats showed the ability to detect altered tumor metabolism as early as one day after TMZ therapy initiation (Figure 7.1), while their tumor volume from T1 post-Gd imaging did not show a reduction until 5 to 7 days after treatment (Figure 7.2). The percent change in Lac/Pyr from baseline was statistically different between the two groups at D1 and D2 ($p<0.008$), while the percent tumor volume change from baseline was not ($p>0.1$).

Eight of the ten treated rats exhibited a reduction in Lac/Pyr at day 1 after the initiation of treatment. The other two rats showed an increase of 6 % and 16 % at day 1 but a decrease of -11 % and -27 % at day 2 compared to baseline, respectively. Lac/Pyr of all control rats (n=10) exhibited an increase over time (Figure 7.1). The substantial difference in ^{13}C metabolism between the two groups at this early stage following treatment suggests that this method has a great potential for early monitoring response to TMZ chemotherapy in brain tumors.

Early detection of treatment response is critical for determining whether patients should remain on a specific therapy or not. Effective treatment is often complicated for patients with GBM by its infiltrative nature, which constrains the ability of surgeon to safely perform a complete resection. TMZ is typically given to patients after surgery in an attempt to kill the remaining tumor cells. The heterogeneous nature of GBM makes it difficult to predict the outcome of TMZ therapy (168,169). The ability to non-invasively detect tumor response to TMZ therapy may therefore assist in providing more

personalized treatment strategies and therefore improve the management of patients with GBM.

To the best of our knowledge, this is the first report of a non-invasive imaging modality that detected response to TMZ therapy one day after the initiation of the treatment. A recent study used the same xenograft model of rat brain (U-87 MG) to evaluate TMZ therapy using anatomical MRI, diffusion MRI and ^{1}H MRS (170). Authors from this study reported that there was a 34 % increase in apparent diffusion coefficient (ADC) of the treated group compared to the control group at 11 days after the initiation of the treatment. They also reported a 3-fold increase in NAA-to-total choline ratio (NAA/tCho) from the treated group and a 5-fold decrease in NAA/tCho from the control group that occurred between the 12th and 23rd day from baseline. The tumor volume measured from T_2-weighted MRI showed a reduction at D7, which is consistent with our study, where the tumor volume measured from T_1-weighted post-Gd images started to shrink between D5 to D7 (Figure 7.2). Morphological evidence of tumor reduction in these time points was consistent with the finding from immunohistochemical analysis of a rat sacrificed at D7, which exhibited widespread apoptotic cells (Figure 7.5).

The results from this study suggest that metabolic imaging with hyperpolarized [1-^{13}C]-pyruvate may provide a unique tool that clinical neuro-oncologists can use in the future to monitor tumor response to therapy for patients with brain tumors. Future studies will examine the application of this technology to human subjects and will investigate whether similar results can be found using other treatments.

Chapter 8: Summary

Magnetic resonance spectroscopic imaging (MRSI) is one of the most active areas of magnetic resonance research because of its ability to non-invasively assess biochemical status and metabolic activity. ^{1}H MRSI has become an important tool for defining tumor burden and evaluating therapy outcome in patients with brain tumors. Hyperpolarized ^{13}C MRSI is a new modality that has opened the door for monitoring *in vivo* biochemical reactions with high sensitivity. The aim of this dissertation project was to develop new methods to improve brain tumor characterization and management using both ^{1}H and hyperpolarized ^{13}C MRSI.

Evaluation of combined information from ^{1}H MRSI and magnetic resonance imaging (MRI) for radiation target definition showed that the combination of morphological and metabolic abnormalities may be sufficient to define target volumes in patients with gliomas. This would allow for a reduction and custom shaping of the current volumes used for brain gliomas and reduce the dose delivered to uninvolved normal brain tissue.

A new lactate-edited 3D ^{1}H MRSI sequence was implemented at 3 T and applied to patients with brain tumor. The implementation of this technique means that lactate can be evaluated in a routine clinical setting in order to study its potential as a marker for prognosis and response to therapy.

The application of hyperpolarized ^{13}C MRSI to a human glioblastoma xenograft in rat brain revealed distinct ^{13}C metabolic characteristics between the abnormal brain

tissue of the rats with tumors and the normal brain tissue of rats without tumor. This study suggested that tumor metabolism in brain tumor models can be examined using hyperpolarized ^{13}C MRSI.

The feasibility of using dynamic nuclear polarization hyperpolarized [1-^{13}C]-pyruvate to detect early response to temozolomide (TMZ) treatment was demonstrated using an orthotopic human glioblastoma xenograft model in rat brain. The ^{13}C data from the treated rats showed the ability to detect altered tumor metabolism as early as one day after the TMZ treatment initiation. The results from this study suggest that metabolic imaging with hyperpolarized [1-^{13}C]-pyruvate may provide a new tool for clinical neuro-oncologists to use in monitoring tumor response to therapy for patients with brain tumors.

The application of these new methods has the potential for improving the characterization and management of brain tumors using ^{1}H and hyperpolarized ^{13}C MRSI. Future studies will focus on using ^{1}H MRSI for predicting treatment outcome in patients with glioblastoma multiforme and applying hyperpolarized ^{13}C MRSI to monitor response to therapy.

References

1. Block F, Hansen WW, Packard M. The Nuclear Induction Experiment. Phys Rev 1946;70:474-485.
2. Lauterbur PC. Image formation by induced local interactions. Examples employing nuclear magnetic resonance. Nature 1973;242:190-191.
3. Law M, Hamburger M, Johnson G, et al. Differentiating surgical from non-surgical lesions using perfusion MR imaging and proton MR spectroscopic imaging. Technol Cancer Res Treat 2004;3(6):557-565.
4. Nelson SJ, Graves E, Pirzkall A, et al. In vivo molecular imaging for planning radiation therapy of gliomas: an application of 1H MRSI. J Magn Reson Imaging 2002;16(4):464-476.
5. Nelson SJ, Vigneron DB, Dillon WP. Serial evaluation of patients with brain tumors using volume MRI and 3D 1H MRSI. NMR Biomed 1999;12(3):123-138.
6. Ardenkjaer-Larsen JH, Fridlund B, Gram A, et al. Increase in signal-to-noise ratio of > 10,000 times in liquid-state NMR. Proc Natl Acad Sci U S A 2003;100(18):10158-10163.
7. Jemal A, Siegel R, Ward E, Hao Y, Xu J, Thun MJ. Cancer statistics, 2009. CA Cancer J Clin 2009;59(4):225-249.
8. Central Brain Tumor Registry of the United States analyses of the NPCR and SEER data; 2004-2006.
9. Azevedo FA, Carvalho LR, Grinberg LT, et al. Equal numbers of neuronal and nonneuronal cells make the human brain an isometrically scaled-up primate brain. J Comp Neurol 2009;513(5):532-541.
10. Markert JA, Devita TV, Hellman S, Rosenberg SA. Glioblastoma Multiforme: Jones & Bartlett Publishers; 2004.
11. Daumas-Duport C, Scheithauer B, O'Fallon J, Kelly P. Grading of astrocytomas. A simple and reproducible method. Cancer 1988;62(10):2152-2165.
12. Pignatti F, van den Bent M, Curran D, et al. Prognostic factors for survival in adult patients with cerebral low-grade glioma. J Clin Oncol 2002;20(8):2076-2084.
13. Prados MD, Scott C, Curran WJ, Jr., Nelson DF, Leibel S, Kramer S. Procarbazine, lomustine, and vincristine (PCV) chemotherapy for anaplastic astrocytoma: A retrospective review of radiation therapy oncology group protocols comparing survival with carmustine or PCV adjuvant chemotherapy. J Clin Oncol 1999;17(11):3389-3395.
14. Hess KR, Broglio KR, Bondy ML. Adult glioma incidence trends in the United States, 1977-2000. Cancer 2004;101(10):2293-2299.
15. Stupp R, Mason WP, van den Bent MJ, et al. Radiotherapy plus concomitant and adjuvant temozolomide for glioblastoma. N Engl J Med 2005;352(10):987-996.
16. Muroff LR, Runge VM. The use of MR contrast in neoplastic disease of the brain. Top Magn Reson Imaging 1995;7(3):137-157.

17. Smirniotopoulos JG, Murphy FM, Rushing EJ, Rees JH, Schroeder JW. Patterns of contrast enhancement in the brain and meninges. Radiographics 2007;27(2):525-551.
18. Scerrati M, Roselli R, Iacoangeli M, Pompucci A, Rossi GF. Prognostic factors in low grade (WHO grade II) gliomas of the cerebral hemispheres: the role of surgery. J Neurol Neurosurg Psychiatry 1996;61(3):291-296.
19. Vives KP, Piepmeier JM. Complications and expected outcome of glioma surgery. J Neurooncol 1999;42(3):289-302.
20. Berger MS, Deliganis AV, Dobbins J, Keles GE. The effect of extent of resection on recurrence in patients with low grade cerebral hemisphere gliomas. Cancer 1994;74(6):1784-1791.
21. Devaux BC, O'Fallon JR, Kelly PJ. Resection, biopsy, and survival in malignant glial neoplasms. A retrospective study of clinical parameters, therapy, and outcome. J Neurosurg 1993;78(5):767-775.
22. Bucci MK, Bevan A, Roach M, 3rd. Advances in radiation therapy: conventional to 3D, to IMRT, to 4D, and beyond. CA Cancer J Clin 2005;55(2):117-134.
23. Morris DE, Bourland JD, Rosenman JG, Shaw EG. Three-dimensional conformal radiation treatment planning and delivery for low- and intermediate-grade gliomas. Semin Radiat Oncol 2001;11(2):124-137.
24. Harrison LB, Chadha M, Hill RJ, Hu K, Shasha D. Impact of tumor hypoxia and anemia on radiation therapy outcomes. Oncologist 2002;7(6):492-508.
25. Chamberlain MC. Recurrent brainstem gliomas treated with oral VP-16. J Neurooncol 1993;15(2):133-139.
26. Sloman JC, Bell PA. Cell cycle-specific effects of glucocorticoids on phytohaemagglutinin-stimulated lymphocytes. Clin Exp Immunol 1980;39(2):503-509.
27. Ryken TC, McDermott M, Robinson PD, et al. The role of steroids in the management of brain metastases: a systematic review and evidence-based clinical practice guideline. J Neurooncol;96(1):103-114.
28. Yung WK. Temozolomide in malignant gliomas. Semin Oncol 2000;27(3 Suppl 6):27-34.
29. Parney IF, Chang SM. Current chemotherapy for glioblastoma. Cancer J 2003;9(3):149-156.
30. La Rocca RV, Mehdorn HM. Localized BCNU chemotherapy and the multimodal management of malignant glioma. Curr Med Res Opin 2009;25(1):149-160.
31. Cohen MH, Johnson JR, Pazdur R. Food and Drug Administration Drug approval summary: temozolomide plus radiation therapy for the treatment of newly diagnosed glioblastoma multiforme. Clin Cancer Res 2005;11(19 Pt 1):6767-6771.
32. Bodor N, Brewster ME. Problems of delivery of drugs to the brain. Pharmacol Ther 1982;19(3):337-386.
33. Levin VA. A pharmacologic basis for brain tumor chemotherapy. Semin Oncol 1975;2(1):57-61.
34. Guenault T. Statistical Physics: Springer; 2007.
35. Levitt MH. Spin Dynamics: Basics of Nuclear Magnetic Resonance: John Wiley & Sons; 2001.

36. Haacke ME, Brown RW, Thompson MR, Venkatesan R. Magnetic resonance imaging: physical principles and sequence design: Wiley-Liss; 1999.
37. Wright PJ, Mougin OE, Totman JJ, et al. Water proton T1 measurements in brain tissue at 7, 3, and 1.5 T using IR-EPI, IR-TSE, and MPRAGE: results and optimization. MAGMA 2008;21(1-2):121-130.
38. Stanisz GJ, Odrobina EE, Pun J, et al. T1, T2 relaxation and magnetization transfer in tissue at 3T. Magn Reson Med 2005;54(3):507-512.
39. Bloch F. The Principle of Nuclear Induction. Science 1953;118(3068):425-430.
40. Keevil SF. Spatial localization in nuclear magnetic resonance spectroscopy. Phys Med Biol 2006;51(16):R579-636.
41. Bottomley PA. Spatial localization in NMR spectroscopy in vivo. Ann N Y Acad Sci 1987;508:333-348.
42. Haase A, Frahm J, Hanicke W, Matthaei D. 1H NMR chemical shift selective (CHESS) imaging. Phys Med Biol 1985;30(4):341-344.
43. Duyn JH, Gillen J, Sobering G, van Zijl PC, Moonen CT. Multisection proton MR spectroscopic imaging of the brain. Radiology 1993;188(1):277-282.
44. Albert MS, Cates GD, Driehuys B, et al. Biological magnetic resonance imaging using laser-polarized 129Xe. Nature 1994;370(6486):199-201.
45. Kauczor H, Surkau R, Roberts T. MRI using hyperpolarized noble gases. Eur Radiol 1998;8(5):820-827.
46. Bowers CR, Weitekamp DP. Transformation of symmetrization order to nuclear-spin magnetization by chemical reaction and nuclear magnetic resonance. Phys Rev Lett 1986;57(21):2645-2648.
47. Golman K, Axelsson O, Johannesson H, Mansson S, Olofsson C, Petersson JS. Parahydrogen-induced polarization in imaging: subsecond (13)C angiography. Magn Reson Med 2001;46(1):1-5.
48. Abragam A and Goldman M. Principles of dynamic nuclear polarisation Rep Prog Phys 1978;41:395-467.
49. Overhauser AW. Polarization of Nuclei in Metals. Phys Rev 1953;92(2):411-415.
50. Gabellieri C, Reynolds S, Lavie A, Payne GS, Leach MO, Eykyn TR. Therapeutic target metabolism observed using hyperpolarized 15N choline. J Am Chem Soc 2008;130(14):4598-4599.
51. Merritt ME, Harrison C, Kovacs Z, Kshirsagar P, Malloy CR, Sherry AD. Hyperpolarized (89)Y offers the potential of direct imaging of metal ions in biological systems by magnetic resonance. J Am Chem Soc 2007;129(43):12942-12943.
52. Hall DA, Maus DC, Gerfen GJ, et al. Polarization-enhanced NMR spectroscopy of biomolecules in frozen solution. Science 1997;276(5314):930-932.
53. Hendrick RE, Haacke EM. Basic physics of MR contrast agents and maximization of image contrast. J Magn Reson Imaging 1993;3(1):137-148.
54. Cunningham CH, Chen AP, Albers MJ, et al. Double spin-echo sequence for rapid spectroscopic imaging of hyperpolarized 13C. J Magn Reson 2007;187(2):357-362.
55. Svensson J, Mansson S, Johansson E, Petersson JS, Olsson LE. Hyperpolarized 13C MR angiography using trueFISP. Magn Reson Med 2003;50(2):256-262.

56. Johansson E, Olsson LE, Mansson S, et al. Perfusion assessment with bolus differentiation: a technique applicable to hyperpolarized tracers. Magn Reson Med 2004;52(5):1043-1051.
57. Ishii M, Emami K, Kadlecek S, et al. Hyperpolarized 13C MRI of the pulmonary vasculature and parenchyma. Magn Reson Med 2007;57(3):459-463.
58. Gallagher FA, Kettunen MI, Day SE, et al. Magnetic resonance imaging of pH in vivo using hyperpolarized 13C-labelled bicarbonate. Nature 2008;453(7197):940-943.
59. Day SE, Kettunen MI, Gallagher FA, et al. Detecting tumor response to treatment using hyperpolarized 13C magnetic resonance imaging and spectroscopy. Nat Med 2007;13(11):1382-1387.
60. Golman K, in 't Zandt R, Thaning M. Real-time metabolic imaging. Proc Natl Acad Sci U S A 2006;103(30):11270-11275.
61. Nelson SJ, Vigneron D, Kurhanewicz J, Chen A, Bok R, Hurd R. DNP-Hyperpolarized C Magnetic Resonance Metabolic Imaging for Cancer Applications. Appl Magn Reson 2008;34(3-4):533-544.
62. Albers MJ, Bok R, Chen AP, et al. Hyperpolarized 13C lactate, pyruvate, and alanine: noninvasive biomarkers for prostate cancer detection and grading. Cancer Res 2008;68(20):8607-8615.
63. Chen AP, Kurhanewicz J, Bok R, et al. Feasibility of using hyperpolarized [1-13C]lactate as a substrate for in vivo metabolic 13C MRSI studies. Magn Reson Imaging 2008;26(6):721-726.
64. Gallagher FA, Kettunen MI, Day SE, Lerche M, Brindle KM. 13C MR spectroscopy measurements of glutaminase activity in human hepatocellular carcinoma cells using hyperpolarized 13C-labeled glutamine. Magn Reson Med 2008;60(2):253-257.
65. Warburg O. On the origin of cancer cells. Science 1956;123(3191):309-314.
66. Schroeder MA, Cochlin LE, Heather LC, Clarke K, Radda GK, Tyler DJ. In vivo assessment of pyruvate dehydrogenase flux in the heart using hyperpolarized carbon-13 magnetic resonance. Proc Natl Acad Sci U S A 2008;105(33):12051-12056.
67. Golman K, Petersson JS, Magnusson P, et al. Cardiac metabolism measured noninvasively by hyperpolarized 13C MRI. Magn Reson Med 2008;59(5):1005-1013.
68. Merritt ME, Harrison C, Storey C, Sherry AD, Malloy CR. Inhibition of carbohydrate oxidation during the first minute of reperfusion after brief ischemia: NMR detection of hyperpolarized 13CO2 and H13CO3. Magn Reson Med 2008;60(5):1029-1036.
69. Bleehen NM, Stenning SP. A Medical Research Council trial of two radiotherapy doses in the treatment of grades 3 and 4 astrocytoma. The Medical Research Council Brain Tumour Working Party. Br J Cancer 1991;64(4):769-774.
70. Leibel SA, Scott CB, Loeffler JS. Contemporary approaches to the treatment of malignant gliomas with radiation therapy. Semin Oncol 1994;21(2):198-219.
71. Walker MD, Strike TA, Sheline GE. An analysis of dose-effect relationship in the radiotherapy of malignant gliomas. Int J Radiat Oncol Biol Phys 1979;5(10):1725-1731.

72. Ten Haken RK, Thornton AF, Jr., Sandler HM, et al. A quantitative assessment of the addition of MRI to CT-based, 3-D treatment planning of brain tumors. Radiother Oncol 1992;25(2):121-133.
73. Van Kampen M, Levegrun S, Wannenmacher M. Target volume definition in radiation therapy. Br J Radiol 1997;70 Spec No:S25-31.
74. Sheline GE. Radiotherapy for high grade gliomas. Int J Radiat Oncol Biol Phys 1990;18(4):793-803.
75. Garden AS, Maor MH, Yung WK, et al. Outcome and patterns of failure following limited-volume irradiation for malignant astrocytomas. Radiother Oncol 1991;20(2):99-110.
76. Liang BC, Thornton AF, Jr., Sandler HM, Greenberg HS. Malignant astrocytomas: focal tumor recurrence after focal external beam radiation therapy. J Neurosurg 1991;75(4):559-563.
77. Wallner KE, Galicich JH, Krol G, Arbit E, Malkin MG. Patterns of failure following treatment for glioblastoma multiforme and anaplastic astrocytoma. Int J Radiat Oncol Biol Phys 1989;16(6):1405-1409.
78. Nakagawa K, Aoki Y, Fujimaki T, et al. High-dose conformal radiotherapy influenced the pattern of failure but did not improve survival in glioblastoma multiforme. Int J Radiat Oncol Biol Phys 1998;40(5):1141-1149.
79. Fitzek MM, Thornton AF, Rabinov JD, et al. Accelerated fractionated proton/photon irradiation to 90 cobalt gray equivalent for glioblastoma multiforme: results of a phase II prospective trial. J Neurosurg 1999;91(2):251-260.
80. Kelly PJ, Daumas-Duport C, Kispert DB, Kall BA, Scheithauer BW, Illig JJ. Imaging-based stereotaxic serial biopsies in untreated intracranial glial neoplasms. J Neurosurg 1987;66(6):865-874.
81. Pirzkall A, McKnight TR, Graves EE, et al. MR-spectroscopy guided target delineation for high-grade gliomas. Int J Radiat Oncol Biol Phys 2001;50(4):915-928.
82. Pirzkall A, Li X, Oh J, et al. 3D MRSI for resected high-grade gliomas before RT: tumor extent according to metabolic activity in relation to MRI. Int J Radiat Oncol Biol Phys 2004;59(1):126-137.
83. Dowling C, Bollen AW, Noworolski SM, et al. Preoperative proton MR spectroscopic imaging of brain tumors: correlation with histopathologic analysis of resection specimens. AJNR Am J Neuroradiol 2001;22(4):604-612.
84. McKnight TR, von dem Bussche MH, Vigneron DB, et al. Histopathological validation of a three-dimensional magnetic resonance spectroscopy index as a predictor of tumor presence. J Neurosurg 2002;97(4):794-802.
85. McKnight TR, Noworolski SM, Vigneron DB, Nelson SJ. An automated technique for the quantitative assessment of 3D-MRSI data from patients with glioma. J Magn Reson Imaging 2001;13(2):167-177.
86. Rydberg JN, Hammond CA, Grimm RC, et al. Initial clinical experience in MR imaging of the brain with a fast fluid-attenuated inversion-recovery pulse sequence. Radiology 1994;193(1):173-180.

87. De Coene B, Hajnal JV, Gatehouse P, et al. MR of the brain using fluid-attenuated inversion recovery (FLAIR) pulse sequences. AJNR Am J Neuroradiol 1992;13(6):1555-1564.
88. Tran TK, Vigneron DB, Sailasuta N, et al. Very selective suppression pulses for clinical MRSI studies of brain and prostate cancer. Magn Reson Med 2000;43(1):23-33.
89. Nelson SJ. Analysis of volume MRI and MR spectroscopic imaging data for the evaluation of patients with brain tumors. Magn Reson Med 2001;46(2):228-239.
90. Nelson SJ. Multivoxel magnetic resonance spectroscopy of brain tumors. Mol Cancer Ther 2003;2(5):497-507.
91. Pelizzari CA, Chen GT, Spelbring DR, Weichselbaum RR, Chen CT. Accurate three-dimensional registration of CT, PET, and/or MR images of the brain. J Comput Assist Tomogr 1989;13(1):20-26.
92. Wang C, Pahl JJ, Hogue RE. A method for co-registering three-dimensional multi-modality brain images. Comput Methods Programs Biomed 1994;44(2):131-140.
93. Woods RP, Mazziotta JC, Cherry SR. MRI-PET registration with automated algorithm. J Comput Assist Tomogr 1993;17(4):536-546.
94. Nelson SJ, Nalbandian AB, Proctor E, Vigneron DB. Registration of images from sequential MR studies of the brain. J Magn Reson Imaging 1994;4(6):877-883.
95. Hochberg FH, Pruitt A. Assumptions in the radiotherapy of glioblastoma. Neurology 1980;30(9):907-911.
96. Oppitz U, Maessen D, Zunterer H, Richter S, Flentje M. 3D-recurrence-patterns of glioblastomas after CT-planned postoperative irradiation. Radiother Oncol 1999;53(1):53-57.
97. Lee SW, Fraass BA, Marsh LH, et al. Patterns of failure following high-dose 3-D conformal radiotherapy for high-grade astrocytomas: a quantitative dosimetric study. Int J Radiat Oncol Biol Phys 1999;43(1):79-88.
98. Pirzkall A, Nelson SJ, McKnight TR, et al. Metabolic imaging of low-grade gliomas with three-dimensional magnetic resonance spectroscopy. Int J Radiat Oncol Biol Phys 2002;53(5):1254-1264.
99. Larson DA, Wara WM. Radiotherapy of primary malignant brain tumors. Semin Surg Oncol 1998;14(1):34-42.
100. Herholz K, Heindel W, Luyten PR, et al. In vivo imaging of glucose consumption and lactate concentration in human gliomas. Ann Neurol 1992;31(3):319-327.
101. Kim SH, Chang KH, Song IC, et al. Brain abscess and brain tumor: discrimination with in vivo H-1 MR spectroscopy. Radiology 1997;204(1):239-245.
102. Sijens PE, Levendag PC, Vecht CJ, van Dijk P, Oudkerk M. 1H MR spectroscopy detection of lipids and lactate in metastatic brain tumors. NMR Biomed 1996;9(2):65-71.
103. Li X, Vigneron DB, Cha S, et al. Relationship of MR-derived lactate, mobile lipids, and relative blood volume for gliomas in vivo. AJNR Am J Neuroradiol 2005;26(4):760-769.

104. Saraswathy S, Crawford FW, Lamborn KR, et al. Evaluation of MR markers that predict survival in patients with newly diagnosed GBM prior to adjuvant therapy. J Neurooncol 2009;91(1):69-81.
105. Crawford FW, Khayal IS, McGue C, et al. Relationship of pre-surgery metabolic and physiological MR imaging parameters to survival for patients with untreated GBM. J Neurooncol 2009;91(3):337-351.
106. Prichard JW. What the clinician can learn from MRS lactate measurements. NMR Biomed 1991;4(2):99-102.
107. Aboagye EO, Bhujwalla ZM, He Q, Glickson JD. Evaluation of lactate as a 1H nuclear magnetic resonance spectroscopy index for noninvasive prediction and early detection of tumor response to radiation therapy in EMT6 tumors. Radiat Res 1998;150(1):38-42.
108. Star-Lack J, Spielman D, Adalsteinsson E, Kurhanewicz J, Terris DJ, Vigneron DB. In vivo lactate editing with simultaneous detection of choline, creatine, NAA, and lipid singlets at 1.5 T using PRESS excitation with applications to the study of brain and head and neck tumors. J Magn Reson 1998;133(2):243-254.
109. He Q, Bhujwalla ZM, Glickson JD. Proton detection of choline and lactate in EMT6 tumors by spin-echo-enhanced selective multiple-quantum-coherence transfer. J Magn Reson B 1996;112(1):18-25.
110. Edden RA, Schar M, Hillis AE, Barker PB. Optimized detection of lactate at high fields using inner volume saturation. Magn Reson Med 2006;56(4):912-917.
111. Lange T, Dydak U, Roberts TP, Rowley HA, Bjeljac M, Boesiger P. Pitfalls in lactate measurements at 3T. AJNR Am J Neuroradiol 2006;27(4):895-901.
112. Kim JH, Chang KH, Na DG, et al. 3T 1H-MR spectroscopy in grading of cerebral gliomas: comparison of short and intermediate echo time sequences. AJNR Am J Neuroradiol 2006;27(7):1412-1418.
113. Kelley DA, Wald LL, Star-Lack JM. Lactate detection at 3T: compensating J coupling effects with BASING. J Magn Reson Imaging 1999;9(5):732-737.
114. Kaiser LG, Young K, Matson GB. Elimination of spatial interference in PRESS-localized editing spectroscopy. Magn Reson Med 2007;58(4):813-818.
115. Cunningham CH, Vigneron DB, Chen AP, et al. Design of flyback echo-planar readout gradients for magnetic resonance spectroscopic imaging. Magn Reson Med 2005;54(5):1286-1289.
116. Pauly J, Le Roux P, Nishimura D, Macovski A. Parameter relations for the Shinnar-Le Roux selective excitation pulse design algorithm [NMR imaging]. IEEE Trans Med Imaging 1991;10(1):53-65.
117. Li Y, Osorio JA, Ozturk-Isik E, et al. Considerations in applying 3D PRESS H-1 brain MRSI with an eight-channel phased-array coil at 3 T. Magn Reson Imaging 2006;24(10):1295-1302.
118. Ozturk-Isik E, Crane JC, Cha S, Chang SM, Berger MS, Nelson SJ. Unaliasing lipid contamination for MR spectroscopic imaging of gliomas at 3T using sensitivity encoding (SENSE). Magn Reson Med 2006;55(5):1164-1169.
119. Zierhut ML, Ozturk-Isik E, Chen AP, Park I, Vigneron DB, Nelson SJ. (1)H spectroscopic imaging of human brain at 3 Tesla: comparison of fast three-dimensional magnetic resonance spectroscopic imaging techniques. J Magn Reson Imaging 2009;30(3):473-480.

120. Margosian P SF. Faster MR imaging: imaging with half the data. Health Care Instrum 1986;1:195-197.
121. MacFall JR, Pelc NJ, Vavrek RM. Correction of spatially dependent phase shifts for partial Fourier imaging. Magn Reson Imaging 1988;6(2):143-155.
122. Ozturk-Isik E, Chen AP, Crane JC, et al. 3D sensitivity encoded ellipsoidal MR spectroscopic imaging of gliomas at 3T. Magn Reson Imaging 2009;27(9):1249-1257.
123. Pruessmann KP, Weiger M, Scheidegger MB, Boesiger P. SENSE: sensitivity encoding for fast MRI. Magn Reson Med 1999;42(5):952-962.
124. Otazo R, Mueller B, Ugurbil K, Wald L, Posse S. Signal-to-noise ratio and spectral linewidth improvements between 1.5 and 7 Tesla in proton echo-planar spectroscopic imaging. Magn Reson Med 2006;56(6):1200-1210.
125. Weybright P, Sundgren PC, Maly P, et al. Differentiation between brain tumor recurrence and radiation injury using MR spectroscopy. AJR Am J Roentgenol 2005;185(6):1471-1476.
126. Di Costanzo A, Scarabino T, Trojsi F, et al. Proton MR spectroscopy of cerebral gliomas at 3 T: spatial heterogeneity, and tumour grade and extent. Eur Radiol 2008;18(8):1727-1735.
127. Smith MA, Koutcher JA, Zakian KL. J-difference lactate editing at 3.0 Tesla in the presence of strong lipids. J Magn Reson Imaging 2008;28(6):1492-1498.
128. Kugel H, Heindel W, Ernestus RI, Bunke J, du Mesnil R, Friedmann G. Human brain tumors: spectral patterns detected with localized H-1 MR spectroscopy. Radiology 1992;183(3):701-709.
129. Kaibara T, Tyson RL, Sutherland GR. Human cerebral neoplasms studied using MR spectroscopy: a review. Biochem Cell Biol 1998;76(2-3):477-486.
130. Terpstra M, Gruetter R, High WB, et al. Lactate turnover in rat glioma measured by in vivo nuclear magnetic resonance spectroscopy. Cancer Res 1998;58(22):5083-5088.
131. Ziegler A, von Kienlin M, Decorps M, Remy C. High glycolytic activity in rat glioma demonstrated in vivo by correlation peak 1H magnetic resonance imaging. Cancer Res 2001;61(14):5595-5600.
132. Ross BD, Higgins RJ, Boggan JE, Willis JA, Knittel B, Unger SW. Carbohydrate metabolism of the rat C6 glioma. An in vivo 13C and in vitro 1H magnetic resonance spectroscopy study. NMR Biomed 1988;1(1):20-26.
133. Wijnen JP, Van der Graaf M, Scheenen TW, et al. In vivo 13C magnetic resonance spectroscopy of a human brain tumor after application of 13C-1-enriched glucose. Magn Reson Imaging;28(5):690-697.
134. Gambhir SS. Molecular imaging of cancer with positron emission tomography. Nat Rev Cancer 2002;2(9):683-693.
135. Juweid ME, Cheson BD. Positron-emission tomography and assessment of cancer therapy. N Engl J Med 2006;354(5):496-507.
136. Heron DE, Andrade RS, Beriwal S, Smith RP. PET-CT in radiation oncology: the impact on diagnosis, treatment planning, and assessment of treatment response. Am J Clin Oncol 2008;31(4):352-362.

137. Facey K, Bradbury I, Laking G, Payne E. Overview of the clinical effectiveness of positron emission tomography imaging in selected cancers. Health Technol Assess 2007;11(44):iii-iv, xi-267.
138. Golman K, Ardenkjaer-Larsen JH, Petersson JS, Mansson S, Leunbach I. Molecular imaging with endogenous substances. Proc Natl Acad Sci U S A 2003;100(18):10435-10439.
139. Chen AP, Albers MJ, Cunningham CH, et al. Hyperpolarized C-13 spectroscopic imaging of the TRAMP mouse at 3T-initial experience. Magn Reson Med 2007;58(6):1099-1106.
140. Lu H, Forbes RA, Verma A. Hypoxia-inducible factor 1 activation by aerobic glycolysis implicates the Warburg effect in carcinogenesis. J Biol Chem 2002;277(26):23111-23115.
141. Golman K, Zandt RI, Lerche M, Pehrson R, Ardenkjaer-Larsen JH. Metabolic imaging by hyperpolarized 13C magnetic resonance imaging for in vivo tumor diagnosis. Cancer Res 2006;66(22):10855-10860.
142. Ozawa T, Faddegon BA, Hu LJ, Bollen AW, Lamborn KR, Deen DF. Response of intracerebral human glioblastoma xenografts to multifraction radiation exposures. Int J Radiat Oncol Biol Phys 2006;66(1):263-270.
143. Kohler SJ, Yen Y, Wolber J, et al. In vivo 13 carbon metabolic imaging at 3T with hyperpolarized 13C-1-pyruvate. Magn Reson Med 2007;58(1):65-69.
144. Derby K, Tropp J, Hawryszko C. Design and evaluation of a novel dual-tuned resonator for spectroscopic imaging. J Magn Reson 1990;86:645-651.
145. Zhao L, Mulkern R, Tseng CH, et al. Gradient-Echo Imaging Considerations for Hyperpolarized 129Xe MR. J Magn Reson B 1996;113(2):179-183.
146. Vigneron DB, Nelson SJ, Murphy-Boesch J, et al. Chemical shift imaging of human brain: axial, sagittal, and coronal P-31 metabolite images. Radiology 1990;177(3):643-649.
147. Bracewell RN. The Fourier transform and its applications. New York: McGraw-Hill; 1978.
148. Yoo H, Baia GS, Smith JS, et al. Expression of the hypoxia marker carbonic anhydrase 9 is associated with anaplastic phenotypes in meningiomas. Clin Cancer Res 2007;13(1):68-75.
149. Subhash MN, Rao BS, Shankar SK. Changes in lactate dehydrogenase isoenzyme pattern in patients with tumors of the central nervous system. Neurochem Int 1993;22(2):121-124.
150. Gisselsson A, Lerche, M. (2008) Metabolic activity of diseased and healthy prostate cells investigated as lactate formation from hyperpolarized 13C-pyruvatem [abstract]. Proc. Intl. Soc. Mag. Reson. Med. p 251.
151. Wang J, Klem J, Wyrick JB, et al. Detection of hypoxia in human brain tumor xenografts using a modified comet assay. Neoplasia 2003;5(4):288-296.
152. Lin RY, Vera JC, Chaganti RS, Golde DW. Human monocarboxylate transporter 2 (MCT2) is a high affinity pyruvate transporter. J Biol Chem 1998;273(44):28959-28965.
153. Grzybicki DM, Moore SA. Implications of prognostic markers in brain tumors. Clin Lab Med 1999;19(4):833-847.

154. Reavey-Cantwell JF, Haroun RI, Zahurak M, et al. The prognostic value of tumor markers in patients with glioblastoma multiforme: analysis of 32 patients and review of the literature. J Neurooncol 2001;55(3):195-204.
155. Larson PE, Kerr AB, Chen AP, et al. Multiband excitation pulses for hyperpolarized 13C dynamic chemical-shift imaging. J Magn Reson 2008;194(1):121-127.
156. Davson H, Zlokovic B, Rakic L, Sega MB. An Introduction to the Blood-brain Barrier: CRC Press; 1993.
157. Macdonald DR, Cascino TL, Schold SC, Jr., Cairncross JG. Response criteria for phase II studies of supratentorial malignant glioma. J Clin Oncol 1990;8(7):1277-1280.
158. Walecki J, Tarasow E, Kubas B, et al. Hydrogen-1 MR spectroscopy of the peritumoral zone in patients with cerebral glioma: assessment of the value of the method. Acad Radiol 2003;10(2):145-153.
159. Balmaceda C, Critchell D, Mao X, et al. Multisection 1H magnetic resonance spectroscopic imaging assessment of glioma response to chemotherapy. J Neurooncol 2006;76(2):185-191.
160. Leimgruber A, Ostermann S, Yeon EJ, et al. Perfusion and diffusion MRI of glioblastoma progression in a four-year prospective temozolomide clinical trial. Int J Radiat Oncol Biol Phys 2006;64(3):869-875.
161. Akella NS, Twieg DB, Mikkelsen T, et al. Assessment of brain tumor angiogenesis inhibitors using perfusion magnetic resonance imaging: quality and analysis results of a phase I trial. J Magn Reson Imaging 2004;20(6):913-922.
162. Tomura N, Narita K, Izumi J, et al. Diffusion changes in a tumor and peritumoral tissue after stereotactic irradiation for brain tumors: possible prediction of treatment response. J Comput Assist Tomogr 2006;30(3):496-500.
163. Hamstra DA, Rehemtulla A, Ross BD. Diffusion magnetic resonance imaging: a biomarker for treatment response in oncology. J Clin Oncol 2007;25(26):4104-4109.
164. Wong TZ, van der Westhuizen GJ, Coleman RE. Positron emission tomography imaging of brain tumors. Neuroimaging Clin N Am 2002;12(4):615-626.
165. Hu S, Lustig M, Balakrishnan A, et al. 3D compressed sensing for highly accelerated hyperpolarized (13)C MRSI with in vivo applications to transgenic mouse models of cancer. Magn Reson Med;63(2):312-321.
166. Park I, Larson PE, Zierhut ML, et al. Hyperpolarized 13C magnetic resonance metabolic imaging: application to brain tumors. Neuro Oncol 2010;12(2):133-144.
167. Ardenkjaer-Larsen JH, Macholl S, Johannesson H. Dynamic Nuclear Polarization with trityls at 1.2 K. Appl Magn Reson 2008;34:509-522.
168. Huang F, Kavan P, Guiot MC, Markovic Y, Roberge D. When temozolomide alone fails: adding procarbazine in salvage therapy of glioma. Can J Neurol Sci 2008;35(2):192-197.
169. Brandes AA, Tosoni A, Basso U, et al. Second-line chemotherapy with irinotecan plus carmustine in glioblastoma recurrent or progressive after first-line temozolomide chemotherapy: a phase II study of the Gruppo Italiano Cooperativo di Neuro-Oncologia (GICNO). J Clin Oncol 2004;22(23):4779-4786.

170. Paul Walker, Xavier Tizon, Sébastien Parfait, Johel Miteran, Philippe Maingon, Nicolas Hoffman, Olivier Duchamp. Evaluation of Early Response to Temozolomide and Radiotherapy with Magnetic Resonance Imaging and Proton Magnetic Resonance Spectroscopy in Human Glioma Models in Nude Rats. AACR Annual Meeting. #3733. 2008; San Diego, CA, USA.

Publishing Agreement

It is the policy of the University to encourage the distribution of all theses, dissertations, and manuscripts. Copies of all UCSF theses, dissertations, and manuscripts will be routed to the library via the Graduate Division. The library will make all theses, dissertations, and manuscripts accessible to the public and will preserve these to the best of their abilities, in perpetuity.

Please sign the following statement:

I hereby grant permission to the Graduate Division of the University of California, San Francisco to release copies of my thesis, dissertation, or manuscript to the Campus Library to provide access and preservation, in whole or in part, in perpetuity.

Author Signature

9/30/2010

Date